Bulletin of the Geological Society of Denmark

VOLUME 61 | DECEMBER 2013 | COPENHAGEN

DGF

Bulletin of the Geological Society of Denmark

is published by the Geological Society of Denmark (DGF, Dansk Geologisk Forening), founded in 1893

The *Bulletin* publishes contributions of international interest in all fields of geological sciences, with a natural emphasis on results of new work on material from Denmark, the Faroes and Greenland. Contributions based on foreign material may also be submitted to the Bulletin in cases where the author is a member of the Society. The rate of publishing is one volume per year. All articles are published as pdf-files immediately after acceptance and technical production. A paper edition of each volume is issued at the end of the year and is distributed to libraries only.

Scientific editing and reviewing are done on an unpaid collegial basis; technical production expenses are covered by the membership fees.

The bulletin is freely accessible on the web page of the Geological Society of Denmark: http://2dgf.dk/publikationer/bulletin/index.html.

Instructions to authors:

See inside the back cover and also: http://2dgf.dk/publikationer/bulletin/vejledning.html

Cover: The headland of Kap Dalton on the Blosseville Kyst in East Greenland consists of flood basalts emplaced during and after breakup of the North Atlantic in the early Eocene. The picture shows the transition from the syn-breakup flows of the 55.5 Ma Skrænterne Formation to the 49.1 Ma post-breakup flows of the Igtertivâ Formation. The time interval between the two formations is represented by a c 7 m thick reddish, purplish and black sediment horizon deposited on the eroded top of the uppermost lava flow of the Skrænterne Formation. See this volume pp. 1–18: Larsen, L.M., Pedersen, A.K., Sørensen, E.V., Watt, W.S. & Duncan, R.A.: Stratigraphy and age of the Eocene Igtertivâ Formation basalts, alkaline pebbles and sediments of the Kap Dalton Group in the graben at Kap Dalton, East Greenland. Photo: A.K. Pedersen.

Stratigraphy and age of the Eocene Igtertivâ Formation basalts, alkaline pebbles and sediments of the Kap Dalton Group in the graben at Kap Dalton, East Greenland

LOTTE M. LARSEN, ASGER K. PEDERSEN, ERIK VEST SØRENSEN, W. STUART WATT & ROBERT A. DUNCAN

Larsen, L.M., Pedersen, A.K., Sørensen, E.V., Watt, W.S. & Duncan, R.A., 2013. Stratigraphy and age of the Eocene Igtertivâ Formation basalts, alkaline pebbles and sediments of the Kap Dalton Group in the graben at Kap Dalton, East Greenland. ©2013 by Bulletin of the Geological Society of Denmark, Vol. 61, pp. 1–18. ISSN 2245-7070. (www.2dgf.dk/publikationer/bulletin).

A NE–SW-trending graben at Kap Dalton on the Blosseville Kyst contains an at least 600 m thick succession of Eocene basalt lavas and sediments. The succession has been investigated by new field work, geochemical analysis and radiometric dating by the ^{40}Ar-^{39}Ar incremental heating method. The results show that the volcanic succession comprises about 220 m of the uppermost plateau basalt formation, the Skrænterne Formation. This is separated from the overlying lava flows of the Igtertivâ Formation by 7 m of sediments that represent a period of around six million years. The two formations can be distinguished by different trace element ratios. The Igtertivâ Formation comprises an at least 300 m thick main succession of flows dated to 49.09 ± 0.48 Ma, overlain by sediments of the Bopladsdalen Formation. A basal conglomerate in the sediments contains pebbles of alkaline igneous rocks of which three were dated at 49.17 ± 0.35 Ma, 47.60 ± 0.25 Ma, and 46.98 ± 0.24 Ma. The sediments are thus younger than 47 Ma. Above 30 m of sediments occur two Igtertivâ Formation lava flows dated to 43.77 ± 1.08 Ma. The overlying sediments of the Bopladsdalen and Krabbedalen Formations are therefore not older than about 44 Ma and palynological evidence shows that they are also not much younger than this. Use of the Geological Time Scale 2012 has resulted in good agreement between radiometric and palynological ages.

The Igtertivâ Formation lava flows were fed from a regional coast-parallel dyke swarm indicating a new rifting episode at 49–44 Ma. This coincides with a major mid-Eocene plate reorganisation event in the North Atlantic and the start of northward-propagation of the Reykjanes Ridge through the continent. The Igtertivâ rift may have been directly instrumental for the initiation of this process.

Keywords: Igtertivâ Formation, plateau basalts, alkaline pebbles, Bopladsdalen Formation, radiometric ages, Kap Dalton, East Greenland, ridge propagation.

Received 2 May 2013
Accepted in revised form
28 June 2013
Published online
1 August 2013

Lotte Melchior Larsen [lml@geus.dk], Erik Vest Sørensen [evs@geus.dk], W. Stuart Watt [wsw@geus.dk], Geological Survey of Denmark and Greenland (GEUS), Øster Voldgade 10, DK-1350 Copenhagen K, Denmark. Asger Ken Pedersen [akp@snm.ku.dk], Natural History Museum of Denmark, Øster Voldgade 5–7, DK-1350 Copenhagen K, Denmark (also GEUS). Robert A. Duncan [rduncan@coas.oregonstate.edu], College of Earth, Ocean and Atmospheric Sciences, Oregon State University, Corvallis, Oregon 97331, USA.

The East Greenland flood basalts belong to the North Atlantic Igneous Province and were erupted in connection with continental breakup and the start of formation of the North Atlantic Ocean in the early Tertiary (e.g. Upton 1988; Eldholm & Grue 1994; Saunders *et al*. 1997; Skogseid *et al*. 2000; Brooks 2011). The basalts in East Greenland occurring between 68°N and 70.5°N cover around 65 000 km^2 with an up to 6–8 km thick lava succession (Pedersen *et al*. 1997), forming the most voluminous part of the onshore Tertiary basalts in the North Atlantic Igneous Province. A Paleocene part, the Lower Basalts, is present in a limited area east of Kangerlussuaq (Nielsen *et al*. 1981) whereas the overlying 'plateau basalts' extend over the whole area (Pedersen *et al*. 1997). The stratigraphy of the plateau basalts was established by Larsen *et al*. (1989) who defined five regionally extensive basalt formations, *viz*. the Magga Dan, Milne Land, Geikie Plateau, Rømer Fjord and Skrænterne Formations. In contrast, the sixth and youngest formation, the Igtertivâ Formation, was found only in a small downfaulted area at Kap Dalton on the Blosseville Kyst. Data on this formation were therefore scarce and the boundary to the underlying Skrænterne Formation

was not identified, resulting in a stratigraphic gap in the known succession.

The precise age of the Milne Land to Skrænterne Formations was established with ^{40}Ar-^{39}Ar dating by Storey *et al.* (2007a) who found that all were erupted within a very narrow interval around 55.5 Ma within the earliest Eocene. No reliable age was obtained for the Igtertivâ Formation.

The promontory of Kap Dalton is situated at 69°27'N in the northern part of the Blosseville Kyst in central East Greenland (Fig. 1). The Igtertivâ Formation is preserved in a small graben behind the headland and is overlain by the oldest known post-basaltic sediments, including conglomerates with pebbles of exotic alkaline igneous rocks (Wager 1935). The succession spans a crucial time period during which large changes in volcanism, sedimentation and palaeogeography took place.

This paper presents a much extended volcanic stratigraphy of the Kap Dalton area together with the first radiometric age determinations of the lavas of the Igtertivâ Formation and the alkaline pebbles.

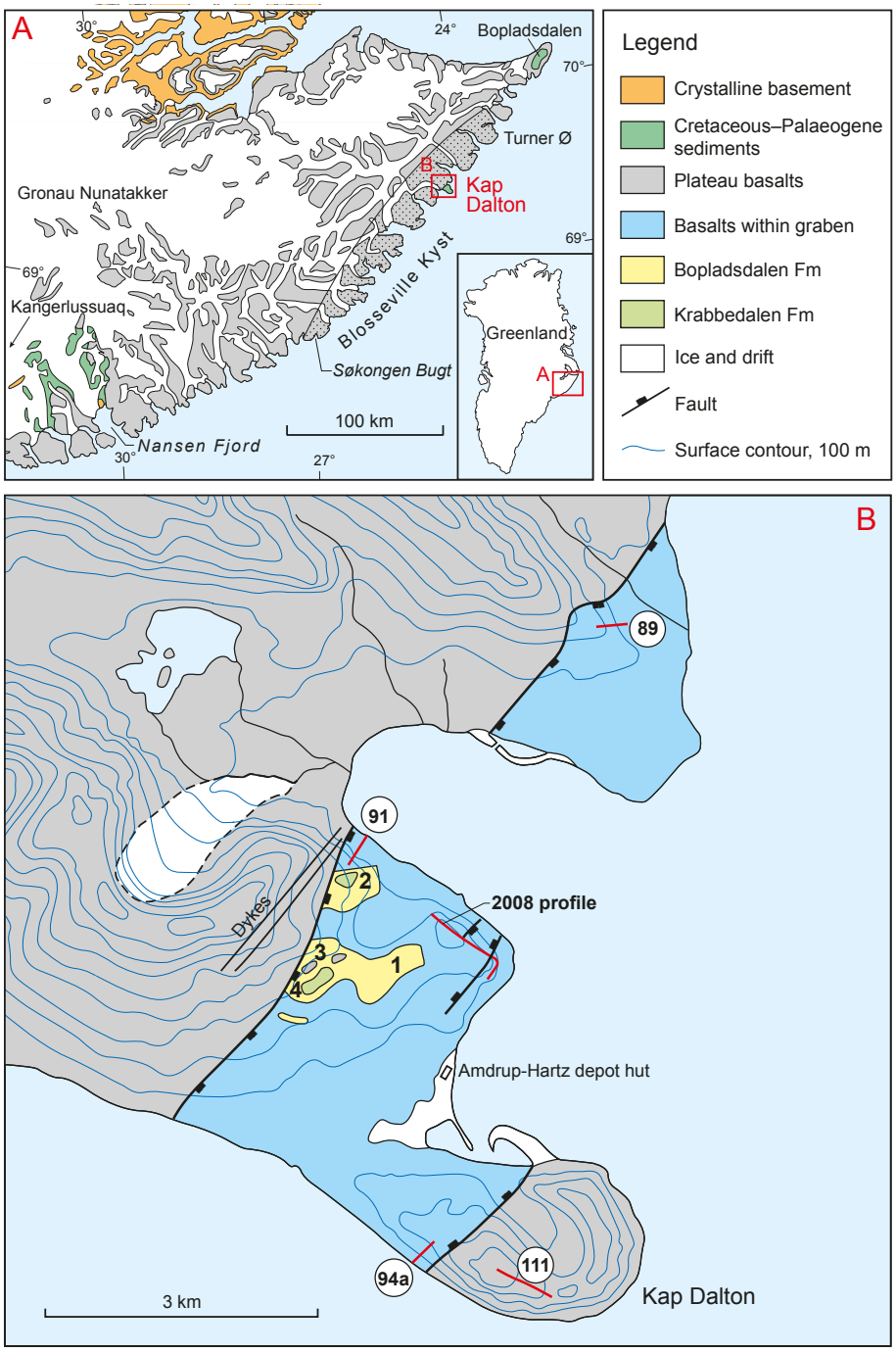

Fig. 1. Geological map of the Kap Dalton area, modified from Larsen *et al.* (2005). Sampled profiles through the volcanic succession are shown by red lines; ringed numbers are profiles from 1975. The numbers 1–4 in the sediments are localities of Larsen *et al.* (2005). The dotted basalt areas in A are cut by a slightly arcuate coast-parallel dyke swarm.

Geological setting and previous work

Due to the remoteness of the Kap Dalton area it has been visited only infrequently. The sediments overlying the basalt lavas were found by O. Nordenskiöld and N.E.K. Hartz during the Danish Amdrup–Hartz expedition in 1900, and the collected fossil material was examined by Ravn (1904). The area was visited again in 1932 during the Scoresby Sound Committee's Second East Greenland Expedition, when L.R. Wager found that the sediment succession had a basal conglomerate with pebbles of a variety of exotic alkaline igneous rocks (Wager 1935). The area was mapped by the Geological Survey of Greenland in 1975 when both sediments and lavas were investigated (Watt *et al*. 1976; Soper & Costa 1976; Soper *et al*. 1976). The next visit was by the Geological Survey of Denmark and Greenland (GEUS) in 2001 when the sediments were investigated in detail for the first time (Larsen *et al*. 2002, 2005; Heilmann-Clausen *et al*. 2008). In 2008 two GEUS geologists briefly visited the Kap Dalton area, taking series of stereo-photographs of the lava succession in the coastal cliffs and sampling the lava succession and the alkaline conglomerate pebbles. The present paper is mainly based on this work.

The graben in the Kap Dalton area is around 3.5 km wide and bounded on both sides by major, NE-running faults (Wager 1935; Watt *et al*. 1976). The north-western boundary fault can be followed for 8 km on the Kap Dalton peninsula and the smaller peninsula immediately to the north (Fig. 1). The down-faulted block is itself cut by a number of small faults. In the northern peninsula the succession is upturned along the edge by drag along the main fault, whereas on the Kap Dalton peninsula the main part of the succession dips around 10°NW (Watt *et al*. 1976; Larsen *et al*. 1989). The resulting small southerly dip component around 2° means that any stratigraphic level drops about 100 m from north to south across the peninsula (Sørensen 2011).

The plateau basalts bounding the graben to the NW are nearly flat-lying and belong to the Geikie Plateau, Rømer Fjord and Skrænterne Formations, indicating a downthrow of the graben succession in excess of 1500 m (Larsen *et al*. 1989). The plateau basalts bounding the graben to the SE on the Kap Dalton headland belong to the uppermost part of the Skrænterne Formation and are downthrown about 1400 m relative to the lavas on the mainland; thus the downthrow of the succession in the graben relative to the SE fault may only be a few hundred metres.

The lava succession in the graben was defined as the Igtertivâ Formation by Larsen *et al*. (1989). (Igtertivâ is the old Greenlandic name for Kap Dalton). The stratigraphy of this formation was based on two short sample profiles from 1975 which could not be correlated. In particular, the lower boundary was undefined. The lavas of the Igtertivâ Formation are not cut by any dykes, in contrast to the surrounding lavas where cross-cutting NE-running dykes are frequent (Watt 1975). The majority of the dykes were intruded before the main graben-forming faulting took place (Watt *et al*. 1976), and because of compositional similarities these dykes were considered to have fed the Igtertivâ Formation (Larsen *et al*. 1989).

Sediment layers are commonly present between the lava flows of the Igtertivâ Formation. Red and green siltstones, coal and tuffs have been described, and some layers contain sparse marine microfossils that have been used to constrain the age of the volcanic succession (Soper & Costa 1976; Soper *et al*. 1976; Jolley 1998; Heilmann-Clausen *et al*. 2008).

The sediments overlying the lavas of the Igtertivâ Formation belong to the Bopladsdalen and Krabbedalen Formations of the Kap Dalton Group. The sediments, and their contained fossils, have been described by several authors, notably Ravn (1904, 1933), Wager (1935), Soper & Costa (1976), Soper *et al*. (1976), and Larsen *et al*. (2002, 2005). Larsen *et al*. (2005) provided the most detailed description of the sediments and the lateral variations in four profiles logged in detail (localities 1–4 in Fig. 1).

The alkaline pebbles in the conglomerate at the base of the Bopladsdalen Formation were only re-found in 2001 and no descriptions of them have appeared since Wager's (1935) work.

Age relations

The age of the post-volcanic sediments of the Kap Dalton Group has been revised repeatedly. Most recently Larsen *et al*. (2005), based on detailed palynological data, suggested that the sediments were deposited during a time span of less than 3 million years in the early middle Eocene (early Lutetian), correlating to the upper NP14 to middle NP15 nannoplankton zones. This corresponds to the time interval 47–44 Ma in the Geological Time Scale 2012 (GTS 2012) (Vandenberghe *et al*. 2012).

Heilmann-Clausen *et al*. (2008) presented palynological data for the interbasaltic sediments in the Igtertivâ Formation, 50–100 m below the top of the formation. The dinoflagellate assemblage includes a reliable indicator for an age not older than late Ypresian, latest NP12, corresponding to 50–51 Ma according to GTS 2012. They also presented palaeomagnetic results for two lava flows: the topmost flow just below the Kap Dalton Group sediments is normally magnetised and was referred to either magnetochron C22n (49.34–48.56

Ma) or C21n (47.35–45.73 Ma) (ages according to GTS 2012). A lava flow close to the Amdrup-Hartz depot hut is reversely magnetised and was therefore placed in either C22r or C21r; however, based on the present study the flows near the hut belong to the Skrænterne Formation (see later), and the magnetochron is considered to be C24r as for the rest of the plateau basalt succession (Storey *et al*. 2007a).

Tegner *et al*. (1998) quoted an unpublished ^{40}Ar-^{39}Ar result for the Igtertivâ Formation as suggesting eruption around 48–49 Ma. This is in accordance with the palynological age and is significantly younger than the underlying plateau basalts which are dated by the ^{40}Ar–^{39}Ar method to 56.4–55.3 Ma (Heister *et al*. 2001; Storey *et al*. 2007a).

Field work 2008

In 2008 two of the authors (AKP and EVS) spent two and a half days at Kap Dalton. Because of the crumbling sediments and the relatively smooth topography, exposures are often poor as noted by all earlier workers. However, Wager's (1935) conglomerate locality with pebbles of alkaline igneous rocks was easily found following his map (Fig. 1, locality 1). This is a scree-covered surface where rounded polished pebbles and platy bits of grey volcaniclastic sandstone lie loose as shown in Fig. 3A. In addition, alkaline pebbles were also found at a higher level at locality 3 (Fig. 1) in scree belonging to the Krabbedalen Formation.

The lava succession was sampled in a profile along the top of the steep NE-facing cliff within the graben (Fig. 2; profile line in Fig. 1). The steep cliff face provides good exposures and the stratigraphic control is enhanced by the colour stereo-photographs. This is necessary because the cliff succession dips 7°NW and is cut by one large and two small faults.

At the top of the succession a 30 m thick sediment horizon is present, repeated in two neighbouring fault blocks (Figs 2, 3B, 3C, 4). The sediment is a greenish-grey fissile volcaniclastic sandstone to siltstone with subordinate thin claystone horizons with plant remains. It contains scattered centimetre-sized rounded polished pebbles (Fig. 3D). At the base of the sediment horizon is a poorly exposed conglomerate with a larger concentration of pebbles up to 22 cm in diameter, comprising alkaline igneous rocks. The conglomerate and the volcaniclastic sediments correlate with the Bopladsdalen Formation and Wager's conglomerate at locality 1, as described by Larsen *et al*. (2005). In contrast to locality 1 where two 2 m and 6 m thick quartzitic sandstone horizons are present,

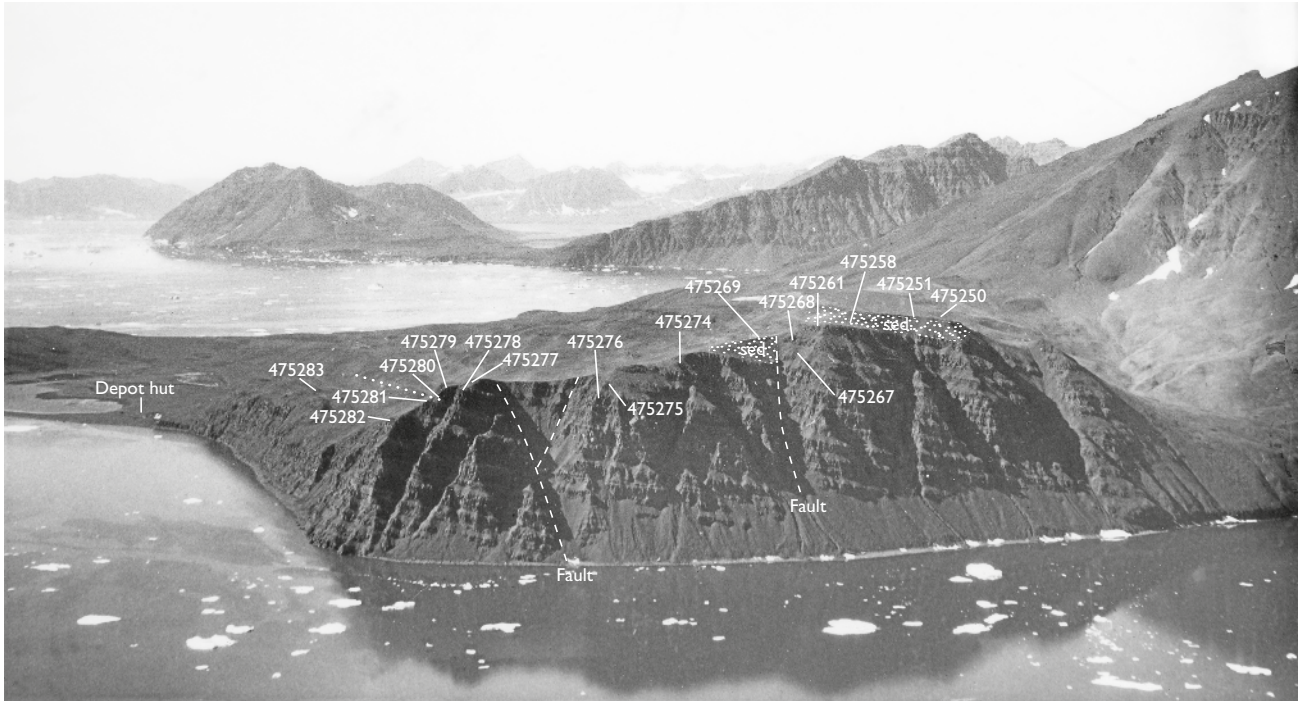

Fig. 2. Overview photograph of the NE-facing cliff where the sample profile in 2008 was taken. Sample numbers are indicated. The 30 m thick sediment horizon near the top of the succession, cut by a fault, is highlighted with small white dots and annotated 'sed'. The dotted line to the left of the cliff, near the location of sample 475280, indicates the position of the boundary between the Skrænterne and Igtertivâ Formations. The headland of Kap Dalton is outside the picture to the left. Height of cliff up to 310 m. Photo by M. Watt 1974.

no quartzitic sandstone horizons were found in the profile at the cliff edge.

The sediment horizon at the cliff edge is overlain by at least two basalt lava flows (Fig. 3B). The lower flow is present in both fault blocks; it is about 8 m thick, vesiculated and coarsely columnar jointed. In the western fault block this flow is overlain by another fairly altered lava flow of which only about 2 m is preserved. Higher parts of the succession are not preserved at the cliff edge where they have been removed by erosion (Fig. 2). No such lava flows are present at locality 1.

The sediments rest on the eroded top of a lava flow. The lava succession below the sediments comprises about ten 20–30 m thick flows of which the upper five were sampled. There is around 5 m of yellow-brown claystone and tuff below the uppermost flow; farther down no sediments are visible between flows but may be present beneath the scree (Fig. 4). All flows have the morphology of subaerial flows.

The eastern part of the cliff is cut by a fault across which the lava flows cannot be correlated. The lava succession east of the fault consists of about eleven 10–40 m thick flows of which the upper five were sampled. Thick purplish red-brown sediment horizons occur between many of the flows (Fig. 5). Again, all lava flows have the morphology of subaerial flows. This lava succession forms the SE-facing cliff at the end of which the Amdrup-Hartz depot hut is located (Fig. 2).

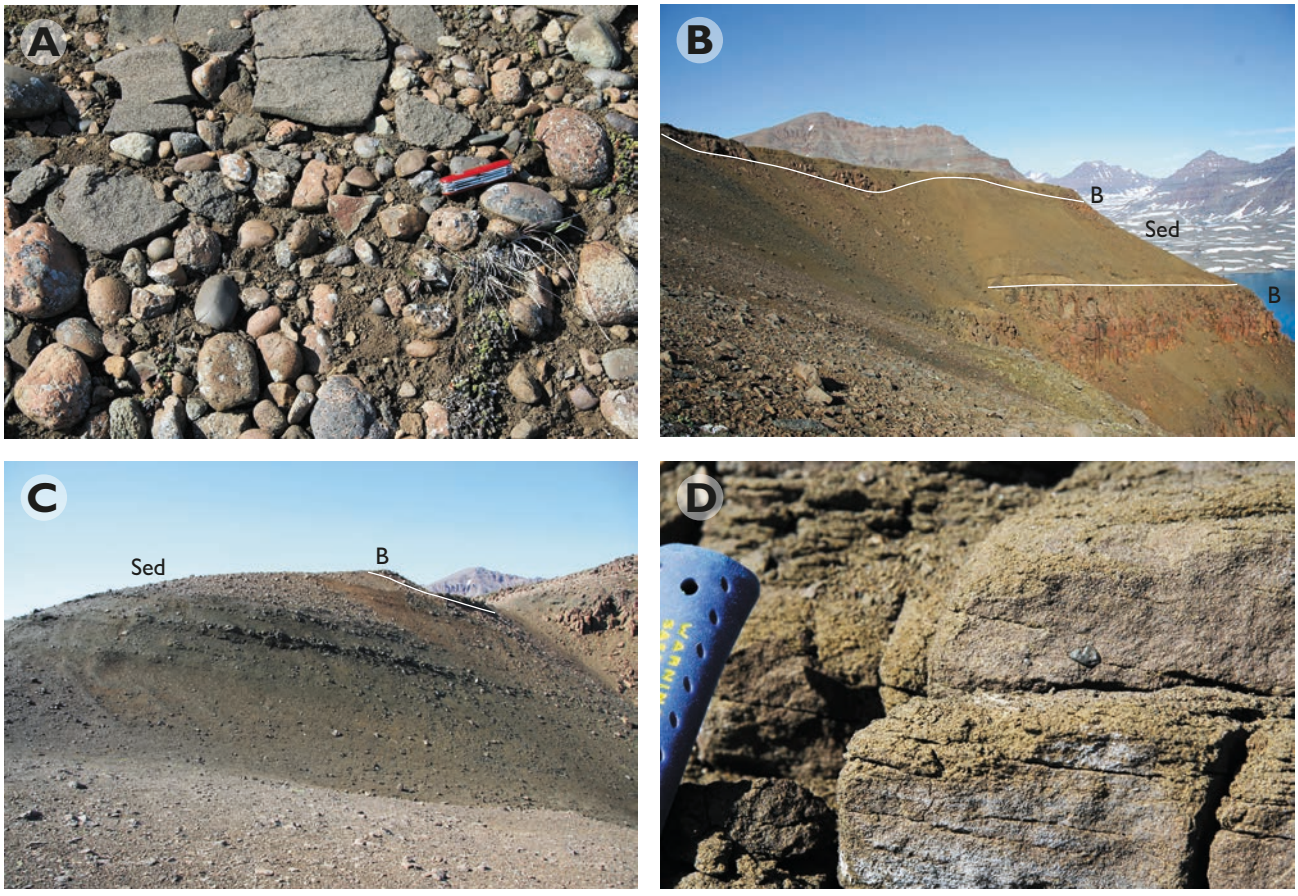

Fig. 3. The Bopladsdalen Formation at Kap Dalton. **A**: Small slabs of volcaniclastic sandstone and rounded polished pebbles of alkaline rocks in scree at locality 1 in Fig. 1. Length of knife handle 8 cm. **B**: Around 30 m of volcaniclastic sediments (Sed) of the Bopladsdalen Formation in the cliff shown in Fig. 2, overlying basalt lavas (B) of the Igtertivâ Formation and capped by two lava flows (B; only one is visible); western of the two fault blocks with sediments, looking west towards the plateau basalts on the mainland. **C**: Bopladsdalen Formation sediments (Sed) capped by a lava flow (B); same succession as shown in 3B but in the eastern of the two fault blocks; height of exposure close to 30 m. **D**: Close-up of fissile volcaniclastic sandstone with a single 1–2 cm pebble.

Analytical methods

Major and trace element analyses

Bulk rocks were analysed for major elements by X-ray fluorescence spectrometry (XRF). Samples with FeO determination were analysed at GGU/GEUS, following procedures given in Kystol & Larsen (1999). Samples with all iron as Fe_2O_3 were analysed at University of Edinburgh, following procedures given in Fitton *et al.* (1998). Results from the two laboratories are closely comparable, as shown by Larsen *et al.* (1998).

Trace elements were analysed by inductively coupled plasma mass spectrometry (ICP-MS) at GEUS, using a PerkinElmer Elan 6100 DRC Quadrupole mass spectrometer. Sample dissolution followed a modified version of the procedure used by Turner *et al.* (1999) and Ottley *et al.* (2003). Calibration was done using two certified REE solutions and three international reference standards. Results for reference samples processed and run simultaneously with the unknowns are normally within 5% of the reference value for most elements with concentrations > 0.1 ppm.

Radiometric age determinations

Samples were dated by the ^{40}Ar-^{39}Ar incremental heating method in the Noble Gas Mass Spectrometry Laboratory at Oregon State University. The instrument is a MAP 215-50 gas mass spectrometer with all-metal extraction system equipped with a 10W CO_2 laser and Heine low-blank, double-vacuum resistance furnace connected to an ultra-clean, low volume (~1000 cc) gas cleanup line. Samples were degassed in 8–17 temperature steps, from 500°C to fusion at around 1400°C. Zr-Al getters removed active gases. Ion beam currents are measured with the electron multiplier at m/z = 35, 36, 37, 38, 39, and 40, and intervening baselines. Measurement times, peak/baseline voltages, data acquisition and storage are computer controlled. Mass discrimination is monitored using an air pipette system. All resulting ages are calculated using the ArArCALC software package (Koppers 2002).

Unaltered phenocrysts were separated by standard mineral separation techniques. Fine grained, unaltered whole-rocks were cored with a 5 mm diameter diamond-tipped drill bit, then sectioned into disks

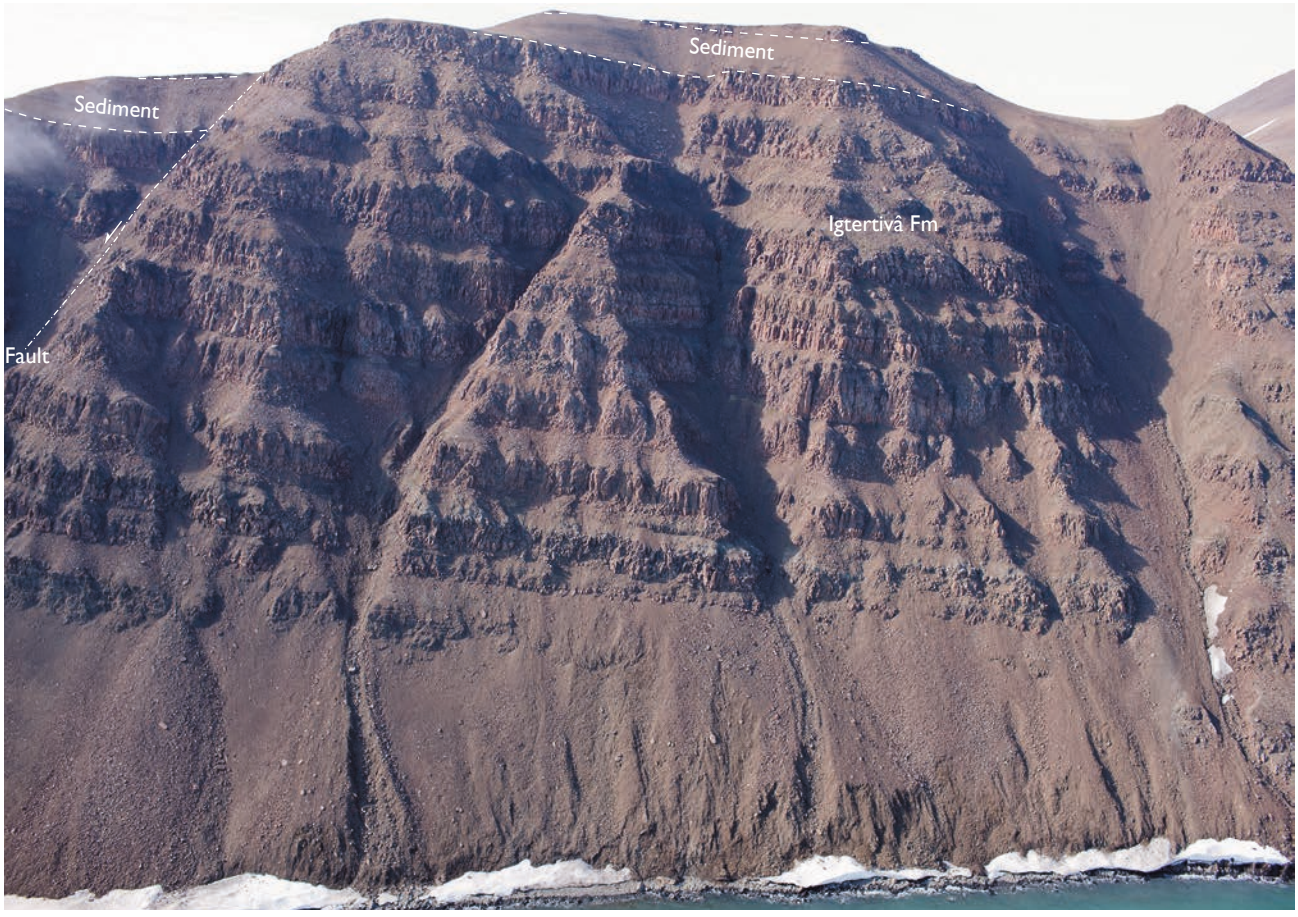

Fig. 4. The volcanic succession of the Igtertivâ Formation in the central part of the cliff face in Fig. 2. The lavas are overlain by 30 m of volcaniclastic sediments belonging to the Bopladsdalen Formation which are again capped by two lava flows. The succession is repeated across a minor fault in the left part of the picture. Height of cliff 310 m.

of 100–300 mg. Samples were irradiated at the Oregon State University TRIGA experimental reactor for six hours at 1 MW power. The neutron flux was monitored with the FCT-3 biotite monitor. All ages are here calculated relative to an age of 28.201 Ma for the Fish Canyon Tuff, following Kuiper *et al*. (2008) and Schmitz (2012), and using the decay constant for ^{40}K of Steiger & Jäger (1977).

Chemical stratigraphy

The profile sampled in 2008 is shown schematically in Fig. 6 together with three shorter profiles (89, 91, 94a) sampled in 1975 (Watt *et al*. 1976). The profile locations are shown in Fig. 1. The four profiles can be confidently placed in relation to each other by combined field and geochemical correlations. Selected chemical analyses, including the dated samples, are shown in Table 1, and all analyses are available in Supplementary data file 1 at the web site http://2dgf.dk/publikationer/bulletin/191bull61.html.

The lavas are all tholeiitic basalts with 4.8–7.2 wt% MgO and 2.0–3.2 wt% TiO_2 (Fig. 7A). Specific correlations can be made at four levels, based on the detailed trace element characteristics of the flows. Three single flows and a group of two flows can be correlated between profiles; these flows are joined by lines in Fig. 6 and encircled in the plots in Fig. 7.

Because of the correlation between the upper flows in profiles 2008 and 91 (Fig. 6, level 4), the conglomerates in these profiles cannot be the same. In profile 91 the lateral correlative to the 30 m sediment horizon and the conglomerate with alkaline pebbles must be situated in the 50 m unexposed interval between samples 116346 and 116347. The conglomerate on top of profile 91 contains only non-alkaline basalt pebbles (N.J. Soper, personal communication 1975), confirming that it is another unit.

Presence of the Skrænterne Formation in the graben at Kap Dalton

A significant discontinuity in trace element ratios is used as datum line in Fig. 6 (correlation level 1). Below this level all flows have higher HREE (Gd/Lu) ratios

Fig. 5. The eastern part of the cliff face in Fig. 2. The fault block to the left, which continues into the background, contains the uppermost lava flows of the Skrænterne Formation. They are overlain by 7 m of red sediment and the two lowermost lava flows of the Igtertivâ Formation. The flows to the right of the fault zone all belong to the Igtertivâ Formation. Height of central cliff section 220 m.

at given LREE (La/Sm) ratios than the flows above this level (Fig. 7B). This difference is accompanied by differences in other incompatible element ratios such as Nb/Y and Zr/Y (Fig. 7C). The flows below the level are shown in green colours in Figs 6 and 7.

The principal difference between the established Igtertivâ and Skrænterne Formations (Larsen *et al.* 1989) was lower TiO_2/P_2O_5 and Zr/Nb ratios in the Igtertivâ Formation than in the Skrænterne Formation (and the underlying plateau basalt formations).

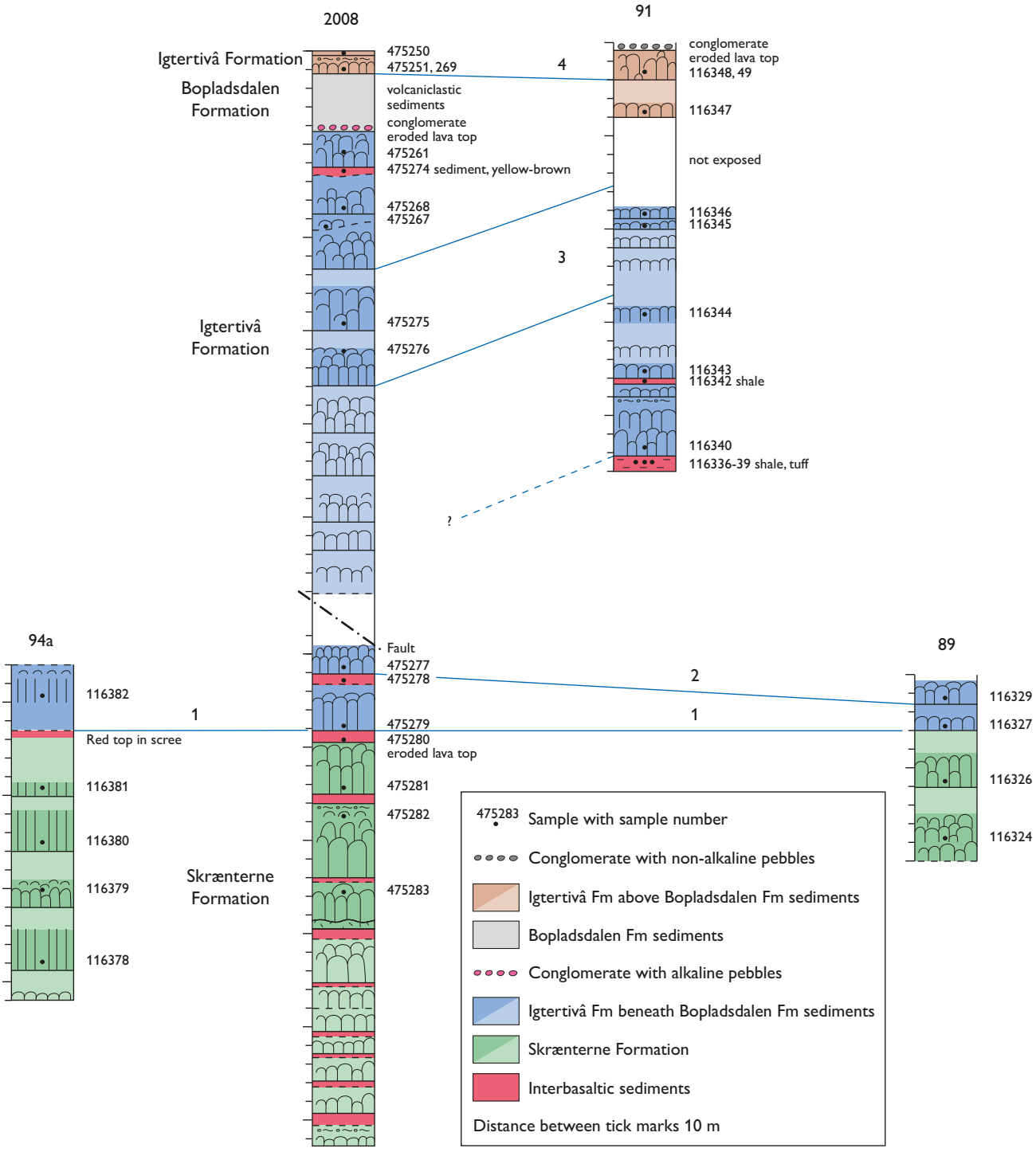

Fig. 6. Diagrammatic representation of the four sampled lava profiles through the Igtertivâ Formation in the Kap Dalton area, with sample numbers indicated. Profile numbers at tops refer to profiles located in Fig. 1. Correlation lines between flows are based on geochemical characteristics, and numbers 1–4 refer to plot groups in Fig. 7. Unsampled parts of the successions have pale colours. The 'decorations' within the lava flows are simplified depictions of the physical appearance of the flows.

As the flows below correlation level 1 in Fig. 6 have significantly higher Zr/Nb than those above, they could actually belong to the Skrænterne Formation. To test this possibility, profile 111 through the upper Skrænterne Formation in the headland of Kap Dalton (Fig. 1; Larsen *et al*. 1989) was analysed for trace elements. The results (Table 1 and Supplementary data file 1) showed that the flows below correlation level 1 in Fig. 6 have trace element contents and ratios that are indistinguishable from the Skrænterne Formation flows in profile 111 (Fig. 7). We conclude that the flows below correlation level 1 belong to the Skrænterne Formation, thereby defining the base of the Igtertivâ Formation.

In the field, the boundary between the Skrænterne and Igtertivâ Formations is unexposed in two profiles although a red sediment was noted in scree in profile 94a (Fig. 6). However the boundary is excellently exposed in the 2008 profile (Fig. 5) where 6.5–7 m of sediment overlies an eroded lava flow whose rubble top has been completely removed (Fig. 8). The sediment comprises, in succession, 0.6 m red laterite overlying the lava, c. 1 m sediment mottled in red-brown and yellow ochre colours, c. 3 m red-brown sediment, 1.6 m dark purplish sediment, and 0.5 m dark, nearly black claystone. A thin top zone is bleached, probably by the overlying lava flow. The sediment horizon represents a considerable time interval, as shown below.

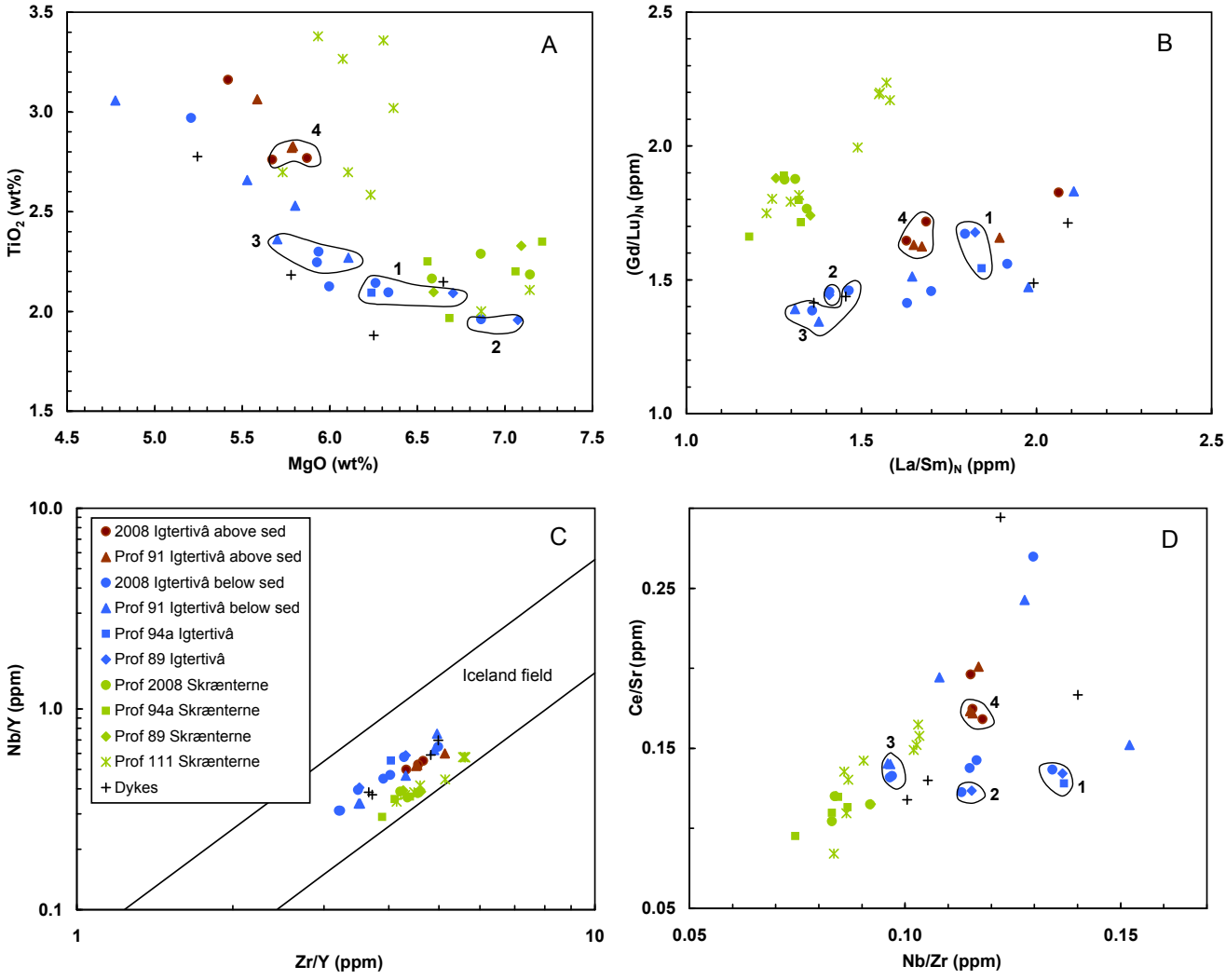

Fig. 7. Geochemical plots of analysed samples from profiles 89, 91, 94a, 111, and 2008. **A**: major elements; **B**, **C**, **D**: various trace element ratios. The subscript N (in B) indicates chondrite normalised concentrations. The differences between the Skrænterne and Igtertivâ Formations are apparent in B and C, whereas the major elements are less diagnostic. Correlated flows at four levels are encircled, and the individuality of these flows is particularly clear in B and D. Numbers 1–4 refer to correlation levels in Fig. 6. The Iceland field in C is after Fitton *et al*. (1998).

Table 1. Analyses of lavas and alkaline pebbles from the Kap Dalton area

GGU-nr	**215605**	**475282**	**475279**	**475275**	**116344**	**475261**	**475269**	**475239**	**475245**	**475258**
Profile	111	2008	2008	2008	91	2008	2008	Trachybas.	Trachyte	Phonolite
Formation	Skrænterne	Skrænterne	Igtertivâ	Igtertivâ	Igtertivâ	Igtertivâ	Igtertivâ	Pebble	Pebble	Pebble
Major elements, wt%										
SiO_2	48.05	48.10	48.28	47.58	49.14	48.95	47.81	47.21	58.08	51.16
TiO_2	3.22	2.11	2.08	2.23	2.49	2.90	2.68	3.12	0.48	0.55
Al_2O_3	13.08	14.14	13.73	14.00	14.19	13.09	13.36	17.43	18.70	20.31
Fe_2O_3	4.02	13.78	13.57	14.45	5.45	15.57	14.96	10.33	5.02	4.78
FeO	10.31				7.33					
MnO	0.22	0.29	0.23	0.26	0.22	0.24	0.24	0.60	0.19	0.19
MgO	5.99	6.43	6.09	5.77	5.71	5.08	5.51	4.02	0.87	0.75
CaO	10.83	11.48	11.42	11.55	10.83	9.39	10.79	9.15	3.11	2.75
Na_2O	2.43	2.20	2.41	2.31	2.62	2.78	2.61	3.45	5.51	7.16
K_2O	0.35	0.17	0.43	0.10	0.51	0.55	0.23	1.82	4.49	4.91
P_2O_5	0.32	0.19	0.21	0.20	0.30	0.38	0.28	0.53	0.08	0.12
LOI	1.39	0.46	0.69	0.81	1.50	0.16	0.48	1.62	3.20	4.66
Sum	100.21	99.35	99.14	99.27	100.29	99.08	98.95	99.28	99.72	97.33
Trace elements, ppm										
Sc	37.2	37.7	40.8	45.3	41.3	37.4	38.8	14.7	2.40	2.46
V	405	348	362	416	361	386	406	215	20.12	70.78
Cr	127	248	90.2	44.5	123	34.1	83.5	18.8	0.72	0.48
Co	54.0	50.5	50.3	56.2	50.3	42.6	47.9	29.7	16.3	10.2
Ni	81.6	103	65.5	49.5	67.1	36.5	51.3	25.9	17.5	1.95
Cu	263	161	177	260	235	214	234	94.7	4.54	3.84
Zn	125	101	106	115	114	128	120	111	103	129
Ga	22.7	20.4	19.5	20.2	20.6	20.6	21.0	26.6	25.7	39.0
Rb	2.85	4.66	7.20	0.37	10.52	5.71	0.92	46.3	160	129
Sr	272	245	249	205	210	207	237	855	1154	519
Y	35.5	30.3	31.8	43.9	45.2	50.0	41.1	31.3	33.8	25.6
Zr	198	132	136	142	195	249	188	309	676	1058
Nb	20.4	10.9	18.3	13.7	21.0	32.4	21.7	66.6	147	329
Cs	0.037	0.020	0.066	0.010	0.058	0.067	0.027	1.388	3.542	3.131
Ba	96.7	72.1	105	34.8	106	157	97.2	761	3919	12080
La	17.52	10.00	14.47	11.71	17.51	24.33	17.44	48.60	80.71	54.38
Ce	42.94	25.52	34.06	26.93	40.75	55.69	41.41	99.53	130.95	101.39
Pr	6.23	3.78	4.67	4.08	5.68	7.43	5.72	12.17	13.51	10.62
Nd	29.18	17.88	20.54	19.03	25.87	32.73	25.32	48.53	43.60	35.64
Sm	7.06	4.88	5.03	5.38	6.65	7.93	6.46	9.38	6.72	6.11
Eu	2.27	1.64	1.64	1.81	2.08	2.36	2.05	3.05	2.78	2.34
Gd	7.76	5.57	5.60	6.70	7.69	8.98	7.39	9.03	7.11	5.46
Tb	1.19	0.93	0.93	1.12	1.28	1.47	1.22	1.24	0.99	0.84
Dy	6.88	5.41	5.55	7.13	7.87	8.98	7.22	6.25	4.93	4.72
Ho	1.309	1.089	1.156	1.538	1.586	1.879	1.468	1.110	0.914	0.896
Er	3.42	2.90	3.10	4.26	4.35	5.13	4.09	2.80	2.50	2.58
Tm	0.477	0.439	0.465	0.650	0.643	0.784	0.590	0.376	0.392	0.413
Yb	2.97	2.62	2.89	3.99	4.07	4.84	3.63	2.16	2.58	2.64
Lu	0.438	0.367	0.414	0.598	0.629	0.712	0.532	0.300	0.379	0.385
Hf	5.22	3.37	3.41	3.64	4.91	6.20	4.76	7.15	12.09	14.61
Ta	1.282	0.957	1.273	0.943	1.325	2.447	1.458	4.059	6.00	7.20
Pb	1.602	0.907	1.199	0.644	1.377	1.998	1.275	3.329	14.3	14.1
Th	1.416	0.859	1.192	1.057	1.704	2.709	1.633	4.422	20.4	24.7
U	0.420	0.247	0.346	0.286	0.407	0.737	0.465	1.131	3.55	15.4

Where no FeO is given, all iron is determined as Fe_2O_3

Improved recognition of the Igtertivâ Formation

The original definition of the Igtertivâ Formation was based mainly on profile 91 with profile 94a as reference profile. Four of the five lava flows in profile 94a have now been relocated to the Skrænterne Formation. The original misplacement was possible because distinction between the formations was mainly based on different TiO_2/P_2O_5 ratios for which there is an overlap zone at low TiO_2. All flows in profile 94a are low-Ti flows that fall in the overlap zone (Larsen *et al.* 1989: fig. 79). One of these flows was analysed for trace elements in 1989, and the Zr/Nb ratio of this flow does indeed plot with the Skrænterne rather than with the Igtertivâ Formation (Larsen *et al.* 1989: figs 83 and 93).

The clear discontinuity in trace element ratios between the Skrænterne and Igtertivâ Formations found in this work provides a much improved tool for discrimination between the two formations. Relative to the Skrænterne Formation the Igtertivâ Formation has lower HREE ratios at similar LREE ratios (Fig. 7B) and higher Nb/Y ratios at similar Zr/Y (Fig. 7C). The parameter ΔNb defined by Fitton *et al.* (1998) is a useful discriminant. It is the vertical distance of a point to the lower of the two black lines defining the Iceland field in Fig. 7C and is calculated as $\Delta Nb=\log(Nb/Y)-1.92\log(Zr/Y)+1.74$. In the present data set the Skrænterne Formation has $\Delta Nb<0.13$ and the Igtertivâ Formation has $\Delta Nb>0.15$ (Supplementary data file 1). The Igtertivâ Formation also has lower TiO_2/P_2O_5, but the analytical uncertainty on the major elements is too large to distinguish the differences at low concentrations.

The changed trace element ratios is an expression of slightly changed melting relations or mantle sources, or both, during the time interval between the two formations. The relatively low HREE ratios of the Igtertivâ Formation suggest melting at shallower levels, possibly due to thinner lithosphere in the Igtertivâ rift zone (e.g. Fram & Lesher 1993). In this respect the Igtertivâ Formation differs from other post-breakup basaltic rocks along the East Greenland coast where 50–47 Ma gabbroic intrusions do not show signs of shallow melting (Bernstein *et al.* 1998).

The lava flows overlying the 30 m sediments high in profiles 2008 and 91 (Fig. 6) are relatively evolved and are chemically indistinguishable from the Igtertivâ Formation below the sediments (Fig. 7). They are therefore considered to be a continuation of the Igtertivâ Formation and not produced in a separate melting event. There is, however, a considerable age difference between these flows and those below the sediment horizon (see below).

Dykes

Four NE-trending dykes cutting the plateau basalts immediately west of the boundary fault near profile 91 (Larsen *et al.* 1989) were also analysed for trace elements. Their geochemical character is completely consistent with that of the Igtertivâ Formation (Fig. 7), supporting the suggestion by Larsen *et al.* (1989) that the dykes are feeders for this formation.

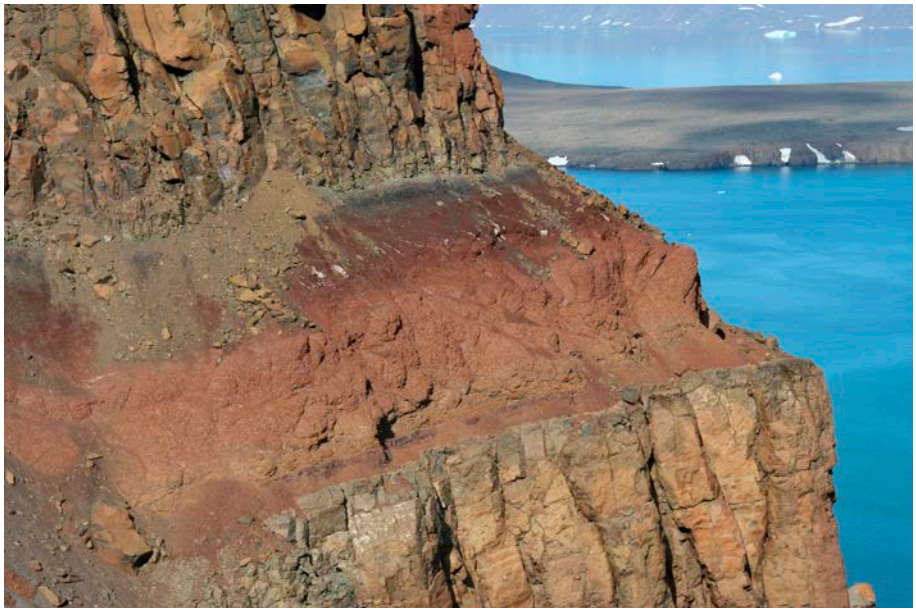

Fig. 8. A sediment horizon about 7 m thick between lava flows of the Skrænterne and Igtertivâ Formations. The uppermost flow in the Skrænterne Formation is eroded and has lost its top zone.

Radiometric ages

The lavas at Kap Dalton are generally K-poor and aphyric, with partial alteration of the groundmass to clay. Suitable candidates for radiometric dating are therefore rare. Reliable ^{40}Ar-^{39}Ar age spectra ('plateaus') were obtained for two lava flows from the Igtertivâ Formation, one flow *below* the 30 m sediment–conglomerate horizon (Bopladsdalen Formation), and one flow *above* the sediment horizon. The results (Table 2 and Fig. 9) indicate ages of 49.09 ± 0.48 Ma for the flow below the sediment, and 43.77 ± 1.08 Ma for the flow above the sediment. This leaves an interval of about 5 million years for deposition of the 30 m sediments of the Bopladsdalen Formation.

The alkaline pebbles in the conglomerate at the base of the Bopladsdalen Formation have higher contents of K_2O and several are feldspar-phyric. Three pebbles of trachybasalt (hawaiite), trachyte and phonolite gave precise, well-defined ages of 49.17 ± 0.35 Ma, 47.60 ± 0.25 Ma, and 46.98 ± 0.24 Ma, respectively (Table 2 and Fig. 10).

Details of the ^{40}Ar-^{39}Ar analyses are available in Supplementary data files 2 and 3.

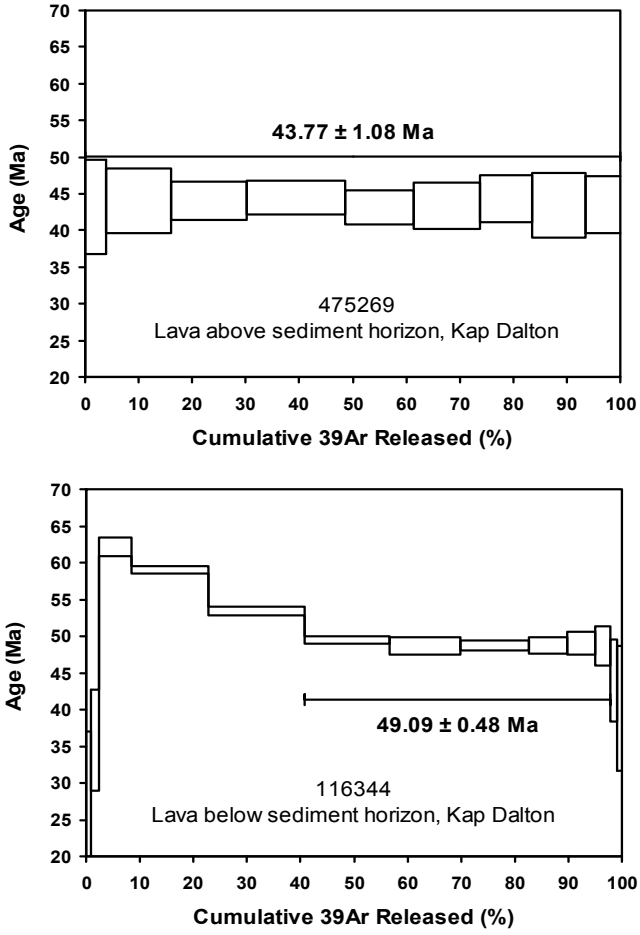

Fig. 9. ^{40}Ar-^{39}Ar age spectra and plateau ages for two lava flows from the Igtertivâ Formation at Kap Dalton. The stratigraphic position of the samples is shown in Fig. 6. The higher analytical uncertainty for the flow above the sediment is due to the very low K-content of the analysed plagioclase.

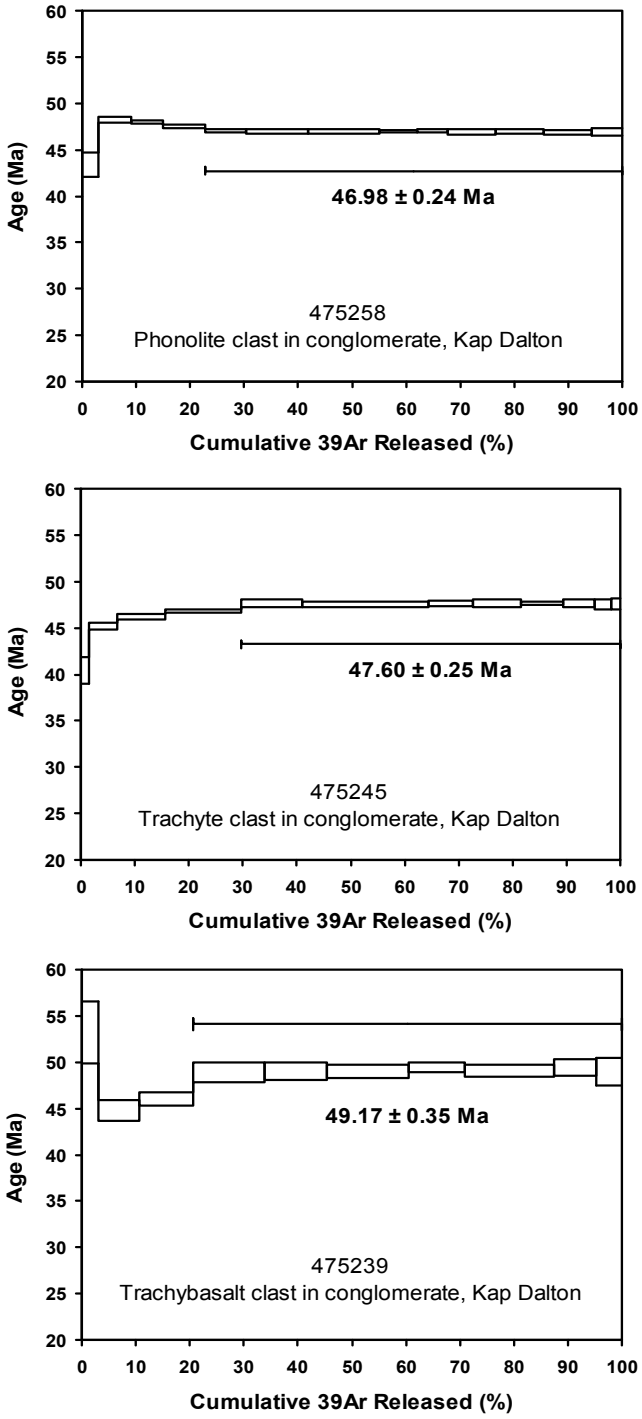

Fig. 10. ^{40}Ar-^{39}Ar age spectra and plateau ages for three pebbles of alkaline igneous rocks in the basal conglomerate of the Bopladsdalen Formation at Kap Dalton. The uncertainties are smaller than for the lavas because of the much higher K contents of the analysed feldspars.

Table 2. ^{40}Ar-^{39}Ar ages for lavas from the Igtertivâ Formation and alkaline pebbles from conglomerate at Kap Dalton

	Sample no.	Material	Plateau age ±2 □ (Ma)	% ^{39}Ar	Isochron age ±2 □ (Ma)	MSWD	$^{40}Ar/^{36}Ar$ Intercept
Lava flows							
Flow below sediment	116344	Groundmass	49.09 ± 0.48	57.0	49.06 ± 1.40	0.95	296 ± 48
Flow above sediment	475269	Plagioclase	43.77 ± 1.08	100	43.86 ± 1.36	0.12	294 ± 13
Pebbles in conglomerate							
Trachybasalt (hawaiite)	475239	Plagioclase	49.17 ± 0.35	79.5	49.50 ± 0.78	0.30	283 ± 28
Trachyte	475245	Feldspar	47.60 ± 0.25	70.2	47.58 ± 0.48	0.10	297 ± 33
Phonolite	475258	Sanidine	46.98 ± 0.24	77.2	46.92 ± 0.73	0.23	300 ± 54

All sample numbers are GGU numbers.
Isochron ages and intercept values are from the inverse isochrons. Details are provided in Electronic Appendices 2 and 3.

Evolution of the volcanic and sedimentary succession in the graben at Kap Dalton

A 220 m thick succession of nine lava flows of the uppermost Skrænterne Formation is present within the graben zone. The best age for this succession is the 55.42 ± 0.06 Ma age for a tuff in the upper part of the Skrænterne Formation in Gronau Nunatakker obtained by Storey *et al*. (2007b). A flow from the Skrænterne Formation near the Amdrup-Hartz hut is reversely magnetised (Heilmann-Clausen *et al*. 2008), belonging in magnetochron C24r. The Skrænterne Formation belongs to the second 'megacycle' of volcanic activity defined by Larsen & Watt (1985) and Larsen *et al*. (1989). The major eruptive centres for this were considered to be situated east of the present coast line in areas that were later to form part of the Jan Mayen continental fragment.

After the deposition of the lavas of the Skrænterne Formation, an episode of erosion removed the top of the lava succession, and a 7 m thick sediment horizon was deposited. The time interval for this is around six million years between 55.4 and 49.1 Ma.

The well defined dyke swarm with a parallel fault system (Watt 1975) that fed the lavas of the Igtertivâ Formation was interpreted by Larsen & Watt (1985) and Larsen *et al*. (1989) to be produced in a distinct rifting event that affected the continent well inboard of the then continental margin towards the opening Atlantic Ocean. This rifting event led to renewed mantle melting, and the main volcanic succession of the Igtertivâ Formation was deposited. The succession is more than 300 m thick and consists of at least 12 lava flows. The radiometric age of 49.09 ± 0.48 Ma is in good agreement with palynological data for interbasaltic sediments indicating an age "not older than latest NP12" (Heilmann-Clausen *et al*. 2008), which corresponds to younger than 50–51 Ma according to GTS 2012. Heilmann-Clausen *et al*. (2008) found that the uppermost flow below the Bopladsdalen Formation at locality 1 is normally magnetised, and according to GTS 2012 the magnetochron is unequivocally C22n (49.34–48.56 Ma).

During the period 49.2–47 Ma (at least), a number of small alkaline central volcanos and magma chambers developed not far from the Kap Dalton area, probably on higher ground away from the rift zone, either north-west or south-east of the present coast.

A period of erosion, possibly caused by relative uplift of the Kap Dalton area, removed the top of the main succession of the Igtertivâ Formation. Because lava flows reappear at higher levels it is inferred that eruption of lava flows from the Igtertivâ Formation continued elsewhere, but the uplift might have prevented later lava flows from reaching the Kap Dalton area. The alkaline volcanos were also eroded.

The sediments of the Kap Dalton Group then started accumulating. According to Larsen *et al*. (2002, 2005) the depositional environment of the sediments was coast-near, starting with a land surface where the eroded lava flows formed an irregular topography with hills and valleys in which rivers deposited conglomerates with rounded pebbles at the base of the formation. The land gradually became covered by shallow-marine sediments. There is therefore a considerable lateral variation which complicates correlation. A suggested correlation scheme for the various units of the Igtertivâ Formation and the Kap Dalton Group is shown in Fig. 11.

The Kap Dalton Group sediments cannot be older than the youngest dated pebble in the basal conglomerate, i.e. 46.98 ± 0.24 Ma (Table 2). The palynological evidence is in good agreement: Larsen *et al*. (2005) state that the dinoflagellate assemblage 1 (Fig. 11) is "not older than the upper part of the NP14 zone", and this corresponds to *c*. 47 Ma according to GTS 2012.

After deposition of around 30 m of the Bopladsdalen sediments a few lava flows from the Igtertivâ Formation reached the Kap Dalton area, perhaps as a result of relative subsidence or tilting. The flows are

present in profiles 2008 and 91 and their age is 43.77 ± 1.08 Ma. Their equivalent level at locality 1 is unknown but, based on the lateral correlation of the thick quartz sandstone horizons at localities 1 and 2 (by Larsen *et al*. 2005), it must be situated somewhere below that horizon at locality 1 (Fig. 11). All sediments above this level cannot be older than 44 ± 1 Ma, including all of the Krabbedalen Formation. The palynological evidence is again in agreement with the radiometric ages: Larsen *et al*. (2005) state that the dinoflagellate assemblages 1 and 2 (Fig. 11) are not younger than respectively subzones E4d and E5a of Bujak & Mudge (1994); these two neighbouring subzones lie on each side of the P10–P11 zone boundary which in the GTS 2012 has an age between 43.5 and 44 Ma (Vandenberghe *et al*. 2012). In combination, the radiometric and palynological data constrain an age very close to 44 Ma for the sediments above the upper lava flows.

Larsen *et al*. (2005) considered that the deposition of the whole Kap Dalton Group lasted around 3 million years. While there is no conflict between the palynological and radiometric data, it may be questioned whether the Bopladsdalen Formation sediments below the upper lava flows were deposited gradually during the period post-47 Ma to 44 Ma or in a shorter period. Two lines of evidence point to a briefer interval. Firstly, the sediments above the upper lava flows are constrained within a short time span. Secondly, the occurrence of alkaline pebbles in the Krabbedalen Formation indicate that the alkaline rocks were available for erosion around 44 Ma. Such rocks are normally of small volume and extent, and if they were already eroded around 47 Ma it is likely that they would have been completely removed at 44 Ma. It is thus possible that the whole Kap Dalton Group could have been deposited within the interval 45–44 Ma.

Contemporaneous events in the North Atlantic

The magmatism of the Igtertivâ Formation was caused by a distinct rifting event, as indicated by the swarm of NE-trending dykes feeding the lavas of this formation. The dyke swarm (Fig. 1) is slightly arcuate and can be followed along the coast for about 100 km from Søkongen Bugt in the south to Turner Ø in the north (Watt 1975). It probably runs partly east of the coast line where there are thick volcanic rocks to both sides of the large Blosseville Kyst Escarpment (H.C. Larsen 1990). The rift zone was called the "East Greenland extinct axis" and was considered to represent the first, failed, attempt to split the Jan Mayen continental fragment away from Greenland (Larsen & Watt 1985; Larsen *et al*. 1989; H.C. Larsen 1988). The event was

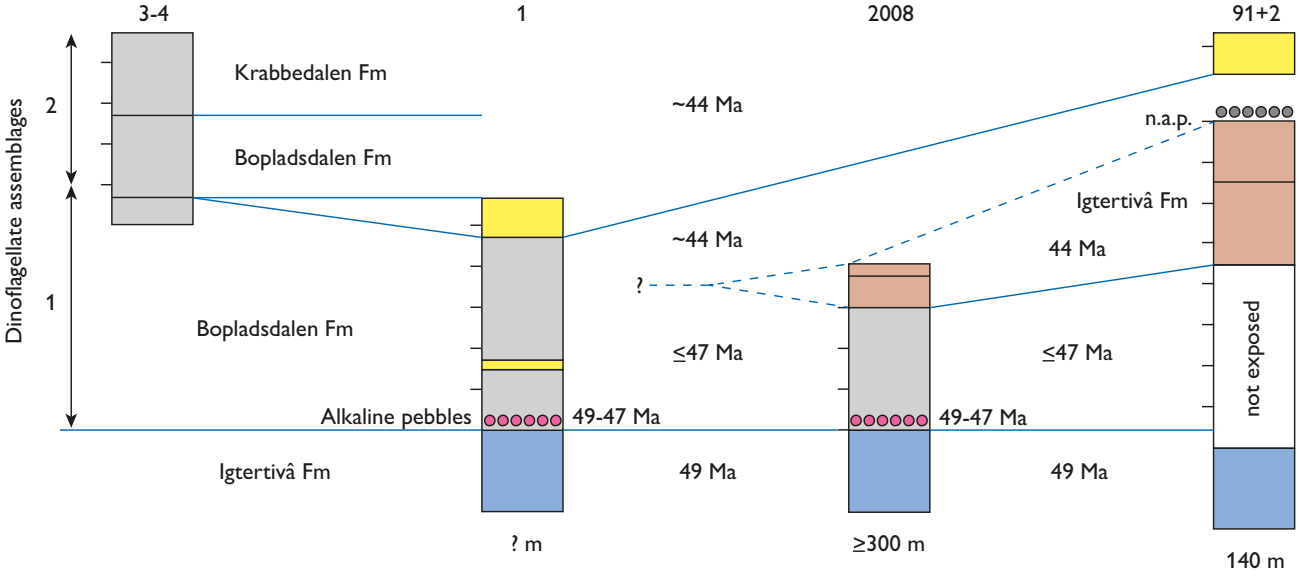

Fig. 11. Suggested correlation of the volcanic–sedimentary succession in the Kap Dalton area, with ages (Ma) indicated. Sediment profiles, with yellow horizons showing quartzitic sandstones, are partly from Larsen *et al*. (2005). Numbers 1–4 above profiles are locality numbers of Larsen *et al*. (2005), and 2008 and 91 are volcanic profiles (Figs 1 and 6). The lavas of the Igtertivâ Formation both underlie the Bopladsdalen Formation (blue) and are interbedded with it (brown). The distance between tick marks on the vertical scale is 10 m; the blue part of the Igtertivâ Formation is shown schematically only. n.a.p.: non-alkaline igneous pebbles. The conglomerate with alkaline pebbles at the base of the Bopladsdalen Formation may be present in locality 2/profile 91 but the level is not exposed.

placed in magnetochron C24n, following closely after the deposition of the main plateau basalt succession, but its re-assignment here to magnetochron C22n does not change the perception of a splitting attempt. However, the dating of the rifting to 49–44 Ma places it with other events at that time.

Gaina *et al*. (2009) and Gernigon *et al*. (2012) proposed that an important plate tectonic reorganisation event took place in the North Atlantic in the mid-Eocene around magnetochron C21r (48.6–47.4 Ma) comprising changes in spreading rate and direction. They noted coincidence in time with events along the East Greenland margin, including the deposition of the Kap Dalton Group sediments and also a peak in intrusive activity along the East Greenland margin farther south where more than 10 intrusive complexes were emplaced between 66°N and 69°N (Bernstein *et al*. 1998; Tegner *et al*. 1998, 2008). An important change was that the Reykjanes Ridge started propagating northwards from the Kangerlussuaq area. The coastal dyke swarm of the Igtertivâ Formation points south-westwards towards the Reykjanes Ridge, and if the rift extended farther south it would be close to the tip of the ridge (Fig. 12). The rift may thus have been directly instrumental to the start of propagation of the Reykjanes Ridge by easing its way through the continent. In this context it is interesting that a lava flow drilled on the shelf outside Nansen Fjord on the southern Blosseville Kyst gave an age of 48.7 ± 0.7 Ma (Thy *et al*. 2007).

The majority of the faults that cut the succession at Kap Dalton, and the formation of the exposed small graben, are later than the period considered here. They may perhaps have formed when the Reykjanes Ridge propagated past the area some time between magnetochrons C13 and C6, at 33 to 24 Ma.

Conclusions

The graben at Kap Dalton contains around 220 m of lava flows belonging to the Skrænterne Formation, the youngest of the plateau basalt formations. This was dated at 55.42 ± 0.06 Ma by Storey *et al*. (2007b). Lavas of the Skrænterne and Igtertivâ Formations can be clearly distinguished by their trace elements, notably the HREE and Nb-Zr-Y ratios.

The transition to the overlying lava flows of the Igtertivâ Formation is well exposed and consists of 7 m

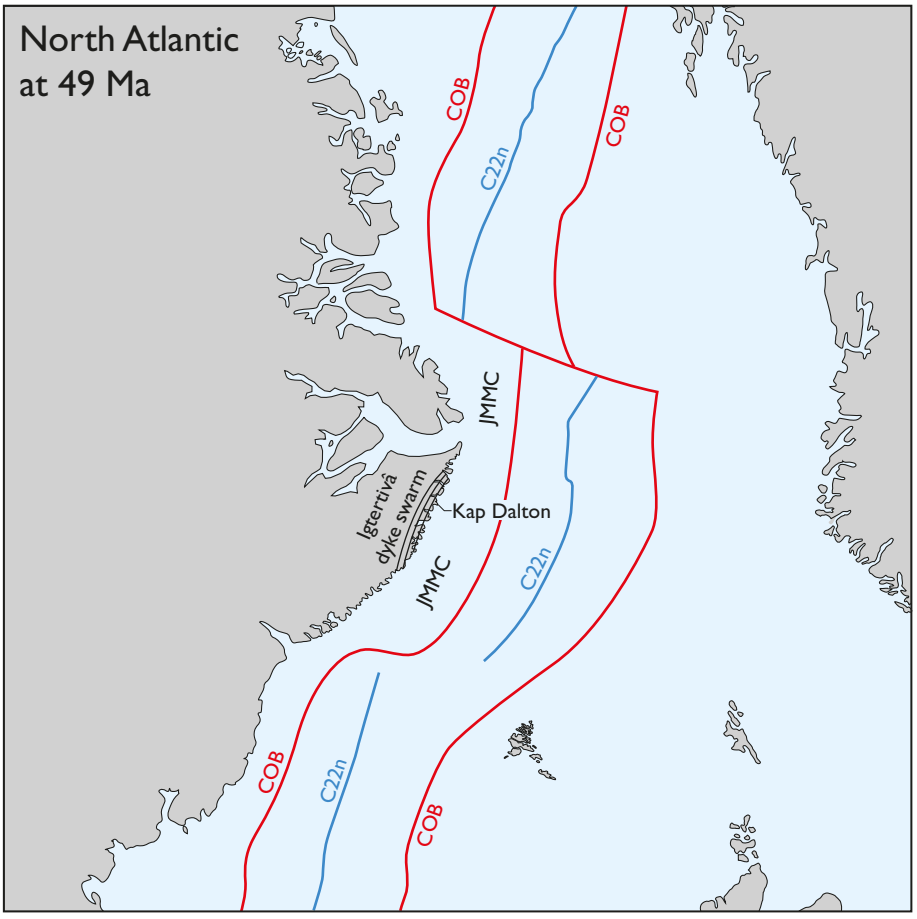

Fig. 12. Part of the North Atlantic reconstructed at 49 Ma with the program GPlates (Boyden *et al*. 2011). This time corresponds to the formation of magnetic anomaly C22n (49.34–48.57 Ma) at the mid-oceanic spreading ridge. Note that the tip of the southern spreading ridge ('Reykjanes Ridge') points directly towards the Igtertivâ dyke swarm and rift zone. COB: Continent–Ocean Boundary. JMMC: the coming Jan Mayen microcontinent.

red and black clay sediments deposited on an eroded lava surface. The horizon represents a time interval of up to six million years.

The lava flows of the Igtertivâ Formation are preserved only within the graben where the succession is more than 300 m thick and intercalated at the top with sediments of the Bopladsdalen Formation of the Kap Dalton Group. The main part of the succession below the sediments is dated at 49.09 ± 0.48 Ma while a lava flow intercalated with sediments of the Bopladsdalen Formation has an age of 43.77 ± 1.08 Ma.

Pebbles of exotic alkaline igneous rocks in the basal conglomerate of the Bopladsdalen Formation (Wager 1935) are dated at 49.17 ± 0.35 Ma, 47.60 ± 0.25 Ma, and 46.98 ± 0.24 Ma. This constrains the age of the sediments to less than 47 Ma. The age of the sediments above the intercalated lavas, comprising the upper part of the Bopladsdalen Formation and all of the overlying Krabbedalen Formation, is close to 44 Ma. There is good agreement between the radiometric and the palynological age data when the Geological Time Scale 2012 is used.

Dykes in a more than 100 km long coast-parallel dyke swarm are compositionally identical to the lavas of the Igtertivâ Formation and are considered to be part of the feeder system for the lavas. The relatively low HREE ratios of the Igtertivâ Formation suggest melting at shallower levels than the Skrænterne Formation, possibly because the melting took place beneath thin lithosphere in the Igtertivâ rift zone.

The Igtertivâ Formation magmatism was caused by a regional rifting event at 49–44 Ma. This coincides with a major mid-Eocene plate reorganisation event in the North Atlantic and the start of northward-propagation of the Reykjanes Ridge through the continent. The Igtertivâ Formation rift may have been directly instrumental to the start of this propagation.

Acknowledgements

We thank GEUS's expedition leader Jørgen Bojesen-Koefoed for providing support during field work on Kap Dalton. John Huard recalculated all the ^{40}Ar-^{39}Ar ages to the new (2012) age for the FCT monitor. Pierpaolo Guarnieri made the GPlates reconstruction of the North Atlantic to 49 Ma, and Michael Larsen and Richard Wilson provided very constructive reviews. Publication of the paper was authorised by the Geological Survey of Denmark and Greenland.

References

Bernstein, S., Kelemen, P.B., Tegner, C., Kurz, M.D., Blusztajn, J. & Brooks, C.K. 1998: Post-breakup basaltic magmatism along the East Greenland Tertiary rifted margin. Earth and Planetary Science Letters 160, 845–862.

Boyden, J.A., Müller, R.D., Gurnis, M., Torsvik, T.H., Clark, J.A., Turner, M., Ivey-Law, H., Watson, R.J. & Cannon, J.S. 2011: Next-generation plate-tectonic reconstructions using Gplates. In: Keller, G. & Baru, C. (eds), Geoinformatics: Cyberinfrastructure for the Solid Earth Sciences, 95–116. Cambridge: Cambridge University Press.

Brooks, C.K. 2011: The East Greenland rifted volcanic margin. Geological Survey of Denmark and Grenland Bulletin 24, 96 pp.

Bujak, J.P. & Mudge, D. 1994: A high-resolution North Sea Eocene dinocyst zonation. Journal of the Geological Society, London, 151, 449–462.

Eldholm, O. & Grue, K. 1994: North Atlantic volcanic margins: dimensions and production rates. Journal of Geophysical Research 99, B2, 2955–2968.

Fitton, J.G., Saunders, A.D., Larsen, L.M., Hardarson, B.S. & Norry, M.J. 1998: Volcanic rocks from the Southeast Greenland margin at 63°N: composition, petrogenesis and mantle sources. In: Saunders, A.D., Larsen, H.C. & Wise, S.H. (eds), Proceedings of the Ocean Drilling Program, Scientific Results 152, 331–350. College Station, TX (Ocean Drilling Program).

Fram, M.S. & Lesher, C.E. 1993: Geochemical constraints on mantle melting during creation of the North Atlantic basin. Nature 363, 712–715.

Gaina, C., Gernigon, L. & Ball, P. 2009: Palaeocene-Recent plate boundaries in the NE Atlantic and the formation of the Jan Mayen microcontinent. Journal of the Geological Society, London, 166, 601–616.

Gernigon, L., Gaina, C., Olesen, O., Ball, P.J., Péron-Pinvidic, G. & Yamasaki, T. 2012: The Norway Basin revisited: From continental breakup to spreading ridge. Marine and Petroleum Geology 35, 1–19.

Heilmann-Clausen, C., Abrahamsen, N., Larsen, M., Piasecki, S. & Stemmerik, L. 2008: Age of the youngest Paleogene flood basalts in East Greenland. Newsletters on Stratigraphy 43, 55–63.

Heister, L.E., O'Day, P.A., Brooks, C.K., Neuhoff, P. & Bird, D.K. 2001: Pyroclastic deposits within the East Greenland Tertiary flood basalts. Journal of the Geological Society, London 158, 269–284.

Jolley, D.W. 1998: Early Eocene palynofloras from Holes 915A, 916A, 917A, and 918D, East Greenland. In: Saunders, A.D., Larsen, H.C. & Wise, S.H. (eds), Proceedings ODP, Scientific Results 152, College Station, TX (Ocean Drilling Program), 221–231.

Koppers, A.K. 2002: ArArCALC – software for $^{40}Ar/^{39}Ar$ age calculations. Computers & Geosciences 28, 605–619.

Kuiper, K.F., Deino, A., Hilgen, F.J., Krijgsman, W., Renne, P.R. & Wijbrans, J.R. 2008: Synchronizing rock clocks of Earth history. Science 320, 500–504.

Kystol, J. & Larsen, L.M. 1999: Analytical procedures in the Rock Geochemical Laboratory of the Geological Survey of Denmark and Greenland. Geology of Greenland Survey Bulletin 184, 59–62.

Larsen, H.C. 1988: A multiple and propagating rift model for the NE Atlantic. In: Morton, A.C. & Parson, L.M. (eds), Early Tertiary volcanism and the opening of the NE Atlantic. Geological Society, London, Special Publication 39, 157–158.

Larsen, H.C. 1990: The East Greenland Shelf. In: Grantz, A., Johnson, L. & Sweeney, J.F. (eds), The Arctic Ocean Region. Boulder, Colorado, Geological Society of America, The Geology of North America Vol. L, 185–210.

Larsen, L.M. & Watt, W.S. 1985: Episodic volcanism during break-up of the North Atlantic: evidence from the East Greenland plateau basalts. Earth and Planetary Science Letters 73, 105–116.

Larsen, L.M., Watt, W.S. & Watt, M. 1989: Geology and petrology of the Lower Tertiary plateau basalts of the Scoresby Sund region, East Greenland. Bulletin Grønlands Geologiske Undersøgelse 157, 164 pp.

Larsen, L.M., Fitton, J.G. & Fram, M.S. 1998: Volcanic rocks of the Southeast Greenland margin in comparison with other parts of the N Atlantic Tertiary volcanic province. In: Saunders, A.D., Larsen, H.C. & Wise, S.H. (eds), Proceedings of the Ocean Drilling Program, Scientific Results 152, 315–330. College Station, TX (Ocean Drilling Program).

Larsen, M., Piasecki, S. & Stemmerik, L. 2002: The post-basaltic Palaeogene and Neogene sediments at Kap Dalton and Savoia Halvø, East Greenland. Geology of Greenland Survey Bulletin 191, 103–110.

Larsen, M., Heilmann-Clausen, C., Piasecki, S. & Stemmerik, L. 2005: At the edge of a new ocean: post-volcanic evolution of the Palaeogene Kap Dalton Group, East Greenland. In: Doré, A.G. & Vining, B.A. (eds), Petroleum Geology: North-West Europe and global perspectives – Proceedings of the 6th Petroleum Geology Conference 923–932. London: The Geological Society.

Nielsen, T.F.D., Soper, N.J., Brooks, C.K., Faller, A.M., Higgins, A.C. & Matthews, D.W. 1981: The pre-basaltic sediments and the Lower Basalts at Kangerdlugssuaq, East Greenland: their stratigraphy, lithology, palaeomagnetism and petrology. Meddelelser om Grønland, Geoscience 6, 28 pp.

Ottley, C.J., Pearson, D.G. & Irvine, G.J. 2003: A routine method for the dissolution of geological samples for the analysis of REE and trace elements via ICP-MS. In: Holland, J.G. & Tanner, S.D. (eds), Plasma Source Mass Spectrometry: Applications and Emerging Technologies, 221–230. Cambridge: Royal Society of Chemistry.

Pedersen, A.K., Watt, M., Watt, W.S. & Larsen, L.M. 1997: Structure and stratigraphy of the Early Tertiary basalts of the Blosseville Kyst, East Greenland. Journal of the Geological Society, London 154, 565–570.

Ravn, J.P.J. 1904: The Tertiary Fauna at Kap Dalton in East-Greenland. Meddelelser om Grønland 29 (3), 95–140.

Ravn, J.P.J. 1933: New investigations of the Tertiary at Cape Dalton, East Greenland. Meddelelser om Grønland 105 (1), 15 pp.

Saunders, A.D., Fitton, J.G., Kerr, A.C., Norry, M.J., & Kent, R.W. 1997: The North Atlantic Igneous Province. In: Mahoney, J.J. & Coffin, M.L. (eds), Large Igneous Provinces. Geophysical Monograph 100, 45–93. Washington, D.C.: American Geophysical Union.

Schmitz, M.D. 2012: Radiogenic isotope geochronology. In: Gradstein, F.M., Ogg, J.G., Schmitz, M. & Ogg, G. (eds), The geologic time scale 2012, 115–126. Amsterdam: Elsevier. DOI: 10.1016/B978-0-444-59425-9.00006-8.

Skogseid, J., Planke, S., Faleide, J.I., Pedersen, T., Eldholm, O., & Neverdal, F. 2000: NE Atlantic continental rifting and volcanic margin formation. In: Nøttvedt, A. *et al*. (eds), Dynamics of the Norwegian Margin. Geological Society, London, Special Publication 167, 295–326.

Soper, N.J. & Costa, L.I. 1976: Palynological evidence for the age of Tertiary basalts and post-basaltic sediments at Kap Dalton, central East Greenland. Rapport Grønlands Geologiske Undersøgelse 80, 123–127.

Soper, N.J., Downie, C, Higgins, A.C. & Costa, L.I. 1976: Biostratigraphic ages of Tertiary basalts on the East Greenland continental margin and their relationship to plate separation in the Northeast Atlantic. Earth and Planetary Science Letters 32, 149–157.

Sørensen, E.V. 2011: Stratigraphy and structure of the lavas and conglomerate in the graben at Kap Dalton, Blosseville Kyst, East Greenland: a field and photogrammetric study. Pp 183–204 in: Sørensen, E.V. 2011: Implementation of digital Multi-Model Photogrammetry for building of 3D-models and interpretation of the geological and tectonic evolution of the Nuussuaq Basin. Unpublished Ph.D. thesis, University of Copenhagen, 204 pp.

Steiger, R.H. & Jäger, E. 1977: Subcommission on geochronology: convention on the use of decay constants in geo- and cosmochronology. Earth and Planetary Science Letters 36, 359–362.

Storey, M., Duncan, R.A. & Tegner, C. 2007a: Timing and duration of volcanism in the North Atlantic Igneous Province: Implications for geodynamics and links to the Iceland hotspot. Chemical Geology 241, 264–281.

Storey, M., Duncan, R.A. & Swisher, C.H. 2007b: Paleocene–Eocene thermal maximum and the opening of the Northeast Atlantic. Science 316, 587–589.

Tegner, C., Duncan, R.A., Bernstein, S., Brooks, C.K., Bird, D. & Storey, M. 1998: ^{40}Ar-^{39}Ar geochronology of Tertiary mafic intrusions along the East Greenland rifted margin: Relation to flood basalts and the Iceland hotspot track. Earth and Planetary Science Letters 156, 75–88.

Tegner, C., Brooks, C.K., Duncan, R.A., Heister, L.E. & Bernstein, S. 2008: ^{40}Ar-^{39}Ar ages of intrusions in East Greenland: rift-to-drift transition over the Iceland hotspot. Lithos 101, 480–500.

Thy, P., Lesher, C.E. & Larsen, H.C. (eds), 2007: Proceedings of the Ocean Drilling Program, Initial Reports 163X. College Station, Texas (Ocean Drilling Program). doi:10.2973/odp.proc.ir.163x.2007.

Turner, S.P., Platt, J.P., George, R.M.M., Kelly, S.P., Pearson, D.G. & Nowell, G.M. 1999: Magmatism associated with orogenic collapse of the Betic–Alboran domain, SE Spain. Journal of Petrology 40, 1011–1036.

Upton, B.G.J. 1988: History of Tertiary igneous activity in the N Atlantic borderlands. In: Morton, A.C. & Parson, L.M. (eds) Early Tertiary volcanism and the opening of the NE Atlantic. Geological Society, London, Special Publication 39, 429–453.

Vandenberghe, N., Hilgen, F.J. & Speijer, R.P. 2012: The Paleogene period. In: Gradstein, F.M., Ogg, J.G., Schmitz, M. & Ogg, G. (eds), The geologic time scale 2012, 855–921. Amsterdam: Elsevier. DOI: 10.1016/B978-0-444-59425-9.00028-7.

Wager, L.R. 1935: Geological investigations in East Greenland. Part II. Geology of Kap Dalton. Meddelelser om Grønland 105 (3), 32 pp + plates and map.

Watt, M. 1975: Photo-reconnaissance of the Blosseville Kyst between Steward Ø and Søkongen Bugt, central East Greenland. Rapport Grønlands Geologiske Undersøgelse 75, 91–95.

Watt, W.S., Soper, N.J. & Watt, M. 1976: Reconnaissance mapping of the northern Blosseville Kyst between Kap Brewster and Kap Dalton, central East Greenland. Rapport Grønlands Geologiske Undersøgelse 80, 120–122.

Depositional environments of Lower Cretaceous (Ryazanian–Barremian) sediments from Wollaston Forland and Kuhn Ø, North-East Greenland

SEBASTIAN PAULY, JÖRG MUTTERLOSE & PETER ALSEN

Pauly, S., Mutterlose, J. & Alsen, P., 2013. Depositional environments of Lower Cretaceous (Ryazanian–Barremian) sediments from Wollaston Forland and Kuhn Ø, North-East Greenland. ©2013 by Bulletin of the Geological Society of Denmark, Vol. 61, pp. 19–36. ISSN 2245-7070. (www.2dgf.dk/publikationer/bulletin).

Lower Cretaceous sediments from the Wollaston Forland–Kuhn Ø area in North-East Greenland have been analyzed for stable carbon isotopes, total organic carbon (TOC) content, and major and trace elements, aiming at a lithological characterization and reconstruction of the depositional environments. The marine sediments of Ryazanian–Barremian age were deposited in North-East Greenland directly after a major Late Jurassic – earliest Cretaceous rifting event. The Lower Cretaceous post-rift sediments are composed of fossiliferous calcareous mud- and marlstones assigned to the Albrechts Bugt (upper Ryazanian – Valanginian) and Rødryggen (Hauterivian) Members. The calcareous sediments are commonly sandwiched between black mudstones of Late Jurassic – earliest Cretaceous (Bernbjerg Formation) and mid Cretaceous (unnamed formation) age. The carbon isotope curves present the first record for the Lower Cretaceous (upper Ryazanian – Barremian) of North-East Greenland. The Ryazanian – Hauterivian sediments are characterized by a mixture of terrigenous detrital matter (quartz, clay minerals, heavy minerals) similar to average shale, with varying $CaCO_3$ concentrations. The Barremian black mudstones on the contrary have lower $CaCO_3$ and higher clay mineral contents. The deposition of the Bernbjerg Formation took place under anoxic bottom water conditions. The depositional environment of the Albrechts Bugt and Rødryggen Members is characterized by well-oxygenated sea-floor conditions, hemipelagic sedimentation of fine-grained terrigeneous detrital matter, and biogenic carbonate settling. After this relatively short interval of carbonate sedimentation under oxic conditions, bottom waters were affected by dysoxic conditions, responsible for the burial of organic matter in the Barremian.

Keywords: Carbon isotope record, TOC, sediment geochemistry, North-East Greenland, Bernbjerg Formation, Albrechts Bugt Member, Rødryggen Member, depositional environment.

Received 28 May 2012
Accepted in revised form
25 June 2013
Published online
23 August 2013

Sebastian Pauly [sebastian.pauly@rub.de], Jörg Mutterlose [joerg.mutterlose@rub.de], Institute of Geology, Mineralogy and Geophysics, Ruhr-University Bochum, Universitätsstrasse 150, D-44801, Germany. Peter Alsen [pal@geus.dk], Geological Survey of Denmark and Greenland (GEUS), Øster Voldgade 10, DK-1350 Copenhagen K, Denmark.

The Greenland–Norwegian Seaway is an important area for understanding the Early Cretaceous palaeoclimate and palaeoceanography. Marine sediments of Early Cretaceous age occur both in North-East Greenland (e.g. Alsen 2006; Pauly *et al*. 2012a) and along the shelf area of Norway and in the Barents Sea (Mutterlose *et al*. 2003). New assessments of undiscovered oil and gas resources suggest that North-East Greenland will form a significant future petroleum province. The potential for the Mesozoic rift basin sediments to serve as a source and a reservoir rock for hydrocarbon explain the intensification of the geological and palaeontological investigations in North-East Greenland.

Important sedimentological and stratigraphic studies of the Jurassic–Cretaceous successions of North-East Greenland were undertaken by Surlyk *et al*. (1973), Surlyk & Clemmensen (1975a,b) and Surlyk (1978, 1984, 2003). Nøhr-Hansen (1993) examined the dinoflagellate cyst stratigraphy of Early Cretaceous successions. Alsen & Rawson (2005) and Alsen (2006) investigated the Lower Cretaceous ammonite faunas, palaeobiogeographical aspects of Early Cretaceous brachiopods were covered by Harper *et al*. (2005), and belemnites by Alsen & Mutterlose (2009). Most recent publications deal with the integrated stratigraphy and palaeoecology of Lower Cretaceous sediments from

Wollaston Forland and Kuhn Ø (Pauly *et al*. 2012a,b). The accumulation of the high latitudinal calcareous sediments is related to an important influx of calcareous nannofossils into the Greenland–Norwegian Seaway. The unusually well-preserved calcareous nannofossil assemblages exhibit an influx of Tethyan and low-to-mid latitudinal taxa, synchronous with observed influxes of Tethyan ammonite and belemnite species (Alsen 2006; Alsen & Mutterlose 2009). These influxes suggest the occurrence of northward flowing surface currents, which allowed Tethyan nekton and plankton to spread as far north as North-East Greenland (55°N palaeolatitude). Further fluctuations in the composition of calcareous nannofossil assemblages indicate a general cooling trend for the late Ryazanian – Valanginian and a subsequent change to warmer climatic conditions in the Hauterivian–Barremian (Pauly *et al*. 2012b).

This study aims at the lithological characterization of black mudstones and marlstones of Early Cretaceous age from Wollaston Forland and Kuhn Ø. Further it is intended to reconstruct the depositional environment on the basis of the total organic matter (TOC) and major and trace element concentrations. For a further characterization of the sedimentary units and detection of possible diagenetic alteration, stable carbon isotope records ($\delta^{13}C_{org}$ and $\delta^{13}C_{carb}$) are presented.

Geological setting and stratigraphy

The Upper Jurassic – Lower Cretaceous sedimentary succession in North-East Greenland reflects deposition during different stages of rifting between Greenland and Norway, related to the opening of the North Atlantic. The up to 3000 m thick sedimentary successions are characterized by coarse clastic sediments that accumulated in submarine fans along fault scarps in westward-tilted half-grabens (Surlyk 1978, 2003). The half-grabens were flooded in the middle Jurassic, reflected by marine deposits resting on Permian rocks or crystalline basement (Surlyk 1978, 2003). A maximum sea-level rise occurred in the Oxfordian to early Volgian, expressed by black mudstones assigned to the Bernbjerg Formation (Surlyk 1990). The rift climax in the middle Volgian to late Ryazanian led to basin infill by coarse clastic deposits, which were draped by thin late Ryazanian – Hauterivian marine deposits at the end and shortly after the major rifting event (Surlyk 1978). These late Ryazanian – Hauterivian sediments are characterized by fossiliferous, calcareous nannofossil bearing mud- and marlstones assigned to the Albrechts Bugt and Rødryggen Members (Palnatokes Bjerg Formation). Integrated calcareous nannofossil and ammonite data from the Wollaston Forland–Kuhn Ø area (Fig. 1) allow a biostratigraphic zonation scheme for the Early Cretaceous Boreal-Arctic Province of the Boreal Realm which give a precise age for the first time. At the studied sections, the 22–34 m thick Albrechts Bugt Member is assigned to the Boreal calcareous nannofossil zones BC 1–5 (upper Ryazanian to Valanginian), and the 3.5–5 m thick Rødryggen Member to zones BC6–11 (Hauterivian) (Pauly *et al*. 2012a). The calcareous sediments are commonly sandwiched within a kilometre-thick mid Jurassic to mid Cretaceous black mudstone succession.

Material and methods

Sections

Rødryggen: The Rødryggen section is situated in the central northern part of Wollaston Forland (Fig. 1) on the western shoulder of a ridge (74°32′47.1″N, 19°50′35.5″W, 65 m a.s.l.), spanning the upper Ryazanian (BC1 Zone) to Hauterivian/Barremian boundary (BC11 Zone) (Pauly *et al*. 2012a). The Albrechts Bugt and Rødryggen Members are here under- and overlain by black mudstones of Ryazanian (Bernbjerg Formation) and Barremian age respectively. The Albrechts Bugt (22 m thick) and Rødryggen members (5 m thick) are composed of calcareous mudstones. A total of 150 rock samples were collected at 20 cm intervals from the Bernbjerg Formation, Albrechts Bugt and Rødryggen Members, and the Barremian (unnamed formation).

Perisphinctes Ravine: At the east coast of Kuhn Ø (74°48′07.1″N, 19°52′56.2″W, 124 m a.s.l.) (Fig. 1) the upper Ryazanian – Valanginian Albrechts Bugt Member and Hauterivian Rødryggen Member are exposed on a steep slope in a ravine, spanning the upper Ryazanian (BC1 Zone) to Hauterivian/Barremian boundary (BC11 Zone) (Pauly *et al*. 2012a). Both units are sandwiched by Ryazanian and Barremian black mudstones. The Albrechts Bugt (34 m thick) and Rødryggen Members (3.5 m thick) consist of calcareous mudstones. A total of 140 rock sediment samples were collected at 25 cm intervals from the Bernbjerg Formation, Albrechts Bugt and Rødryggen Members.

Carbon and oxygen isotope analyses ($\delta^{13}C_{carb}$, $\delta^{18}O_{carb}$ and $\delta^{13}C_{org}$)

Carbon and oxygen isotope analysis of bulk-rock samples was performed on 102 samples with >6% $CaCO_3$ (49 from the Rødryggen section, 53 from the Perisphinctes Ravine section) for the upper Ryaza-

nian – Hauterivian, using a Finnigan MAT 251 mass spectrometer, coupled to the Carbo Kiel device at the Leibniz-Laboratory for Radiometric Dating and Stable Isotope Research in Kiel. The measurements yielded a precision of 0.06‰ for carbon and 0.07‰ for oxygen isotopes. Carbon isotope analysis of organic carbon was performed on 119 samples (70 from the Rødryggen section, 49 from the Perisphinctes Ravine section) for the lower Ryazanian – Barremian. Samples with a minimum of 0.02% TOC have been decarbonised on a hot plate (60°C) using 10% HCl and measured with an elemental analyser (Carlo-Erba 1110) connected online to a ThermoFinnigan Delta Plus mass spectrometer at the GeoZentrum Nordbayern, Erlangen. Reproducibility was better than ± 0.08‰ (1σ). All isotope values are reported in the conventional δ-notation in per mil relative to V-PDB (Vienna-PDB).

Total organic carbon, major and trace element analysis

Total organic carbon (TOC) analysis was performed on 88 samples (63 from the Rødryggen section, 25 from the Perisphinctes Ravine section) with a Deltatronik coulometer at the Ruhr-University Bochum, Germany. TOC was calculated as the difference between total carbon (TC) and total inorganic carbon (TIC): TOC=TC–TIC.

X-ray fluorescence (XRF) analysis for major and trace elements was carried out on 86 samples (62 from the Rødryggen section, 24 from the Perisphinctes Ravine section) with a Philips® PW 2400 X-ray spectrometer at the Department of Microbiogeochemistry, University of Oldenburg. An amount of 600 mg sample powder was mixed with 3600 mg of a 1:1 mixture of dilithium-tetraborate ($Li_2B_4O_7$) and lithium-metaborate ($LiBO_2$), or with 100% dilithium-tetraborate for carbonate-rich samples, pre-oxidized at 500°C with NH_4NO_3 (p.a.) and fused to glass beads.

Results

Carbon isotopes

The $\delta^{13}C_{carb}$ record is characterized by major variations (-11.1 to -0.3‰) in both sections (Fig. 2; Tables 1, 2). The samples show a distinctive ^{13}C depletion resulting in light $\delta^{13}C_{carb}$ values averaging -4.8‰ (Rødryggen section) and -3.8‰ (Perisphinctes Ravine section). The $\delta^{18}O_{carb}$ values are not presented due to the observed diagenetic overprint.

$\delta^{13}C_{org}$ values of the ***Rødryggen section*** range between -28.2 and -20.9‰ (Fig. 2).

Bernbjerg Formation (0–19 m, 5 samples): $\delta^{13}C_{org}$ values show a relatively stable development around -27.8‰.

Albrechts Bugt Member (19–41 m, 28 samples): Isotope ratios vary between -26.0 and -23.9‰ (average -25‰) in the Ryazanian interval, followed by an increase to -20.9‰ and a shift to -26.1‰ in the lower Valanginian interval. In the upper Valanginian interval, after a sample gap, $\delta^{13}C_{org}$ values stay relatively constant around -23‰ and increase to values around -25‰ at the top.

Rødryggen Member (41–46 m, 6 samples): $\delta^{13}C_{org}$ values are relatively constant around -25‰.

Barremian (46–77 m, 31 samples): Carbon isotope values show minor variations around -25‰ in the lower part (46–60 m) and -24‰ in the upper part (60–77 m).

$\delta^{13}C_{org}$ values of the ***Perisphinctes Ravine section*** vary between -27.7 and -22.5‰.

Bernbjerg Formation (0–4 m, 2 samples): $\delta^{13}C_{org}$ is relatively stable showing values around -27.6‰.

Albrechts Bugt Member (4–38 m, 39 samples): In the Ryazanian – lower Valanginian interval $\delta^{13}C_{org}$ values range between -25.6 and -24.2‰ (average -25‰). The upper Valanginian $\delta^{13}C_{org}$ record continues the previous trend before it marks a shift to lighter values (-27‰), followed by a shift to -25‰.

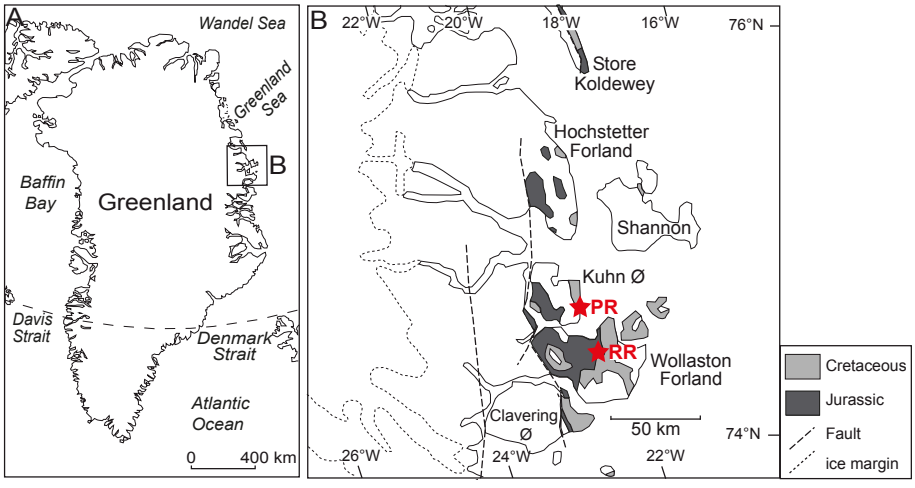

Fig. 1. Maps showing the location of the studied sections in North-East Greenland. **A:** Greenland. **B:** North-East Greenland (74°–76°N), showing the Wollaston Forland–Kuhn Ø area; RR: Rødryggen section; PR: Perisphinctes Ravine section (modified after Alsen 2006).

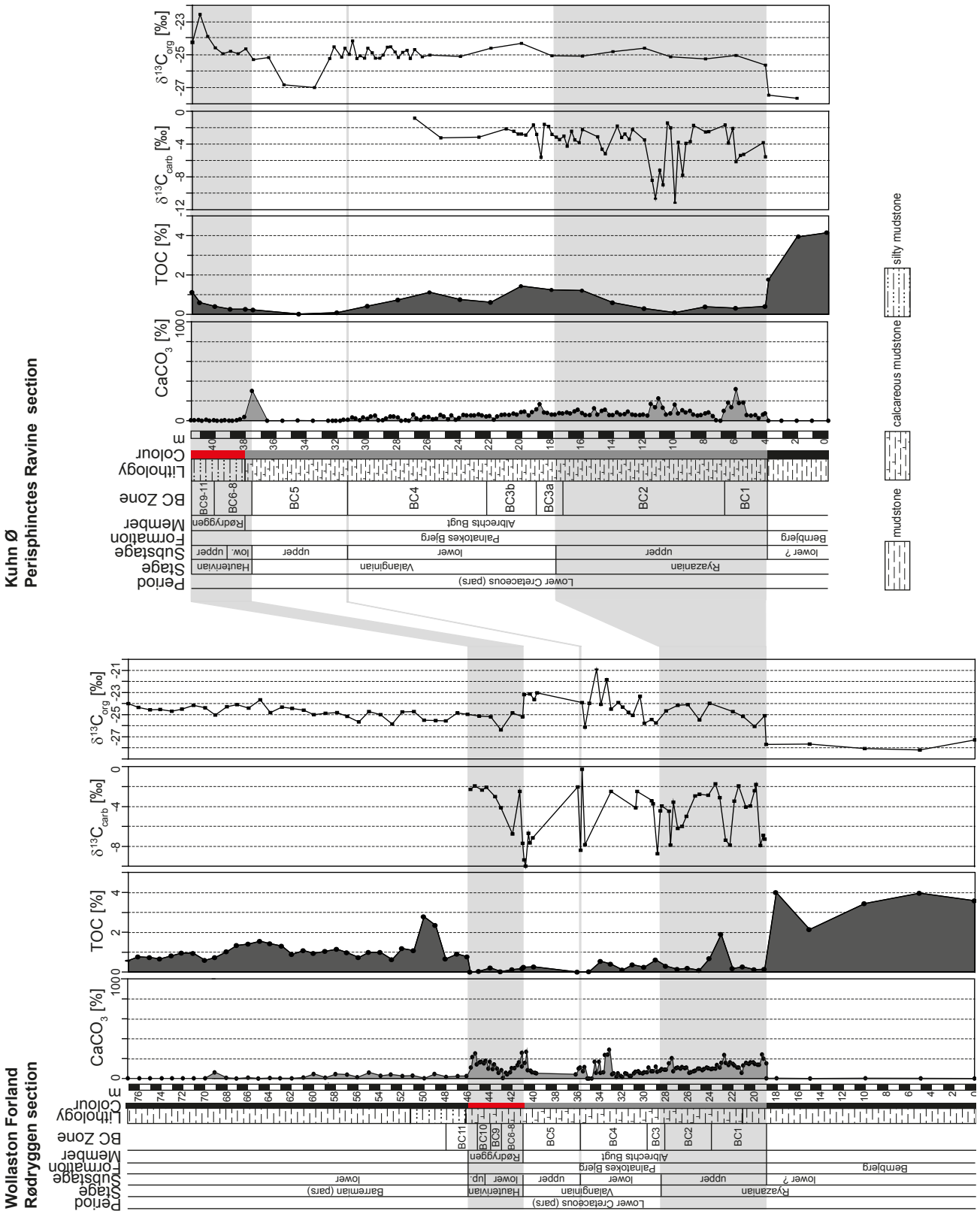

Fig. 2. Lithological logs of the Rødryggen and Perisphinctes Ravine sections showing the calcium carbonate (after Pauly *et al.* 2012b) and TOC contents and carbon isotope records ($\delta^{13}C_{carb}$, $\delta^{13}C_{org}$).

Table 1. $CaCO_3$ (from Pauly *et al*. 2012b) and TOC contents, $\delta^{13}C_{carb}$ and $\delta^{13}C_{org}$ values of the Rødryggen section (Wollaston Forland)

Sample no.	m	$CaCO_3$ [%]	TOC [%]	$\delta^{13}C_{carb}$ [‰]	±s	$\delta^{18}O_{carb}$ [‰]	±s	$\delta^{13}C_{org}$ [‰]
469521	77	2.3	0.6					-23.99
469520	76	0.5	0.8					-24.32
469519	75	2.8	0.7					-24.56
469518	74	0.3	0.7					-24.51
469517	73	4.1	0.8					-24.66
469516	72	0.1	1.0					-24.50
469515	71	0.2	0.9					-24.13
469514	70	2.5	0.6					-24.36
469513	69	6.2	0.7	-7.92	0.02	-10.34	0.02	-25.01
469512	68	0.7	1.0					-24.28
469511	67	0.1	1.4					-24.09
469510	66	0.8	1.4					-24.38
469509	65	0.1	1.6					-23.64
469508	64	0.5	1.4					-24.79
469507	63	0.2	1.3					-24.31
469506	62	0.2	0.9					-24.43
469505	61	1.0	1.1					-24.59
469504	60	4.6	1.0					-24.99
469503	59	0.8	1.1					-24.87
469502	58	4.5	1.2					-24.80
469501	57	3.9	1.0					-25.13
469500	56	1.3	0.7					-25.65
469499	55	6.0	1.0					-24.70
469498	54	2.8	1.0					-25.00
469497	53	4.0	0.6					-25.83
469496	52	2.5	1.2					-24.73
469495	51	2.9	1.1					-24.71
469494	50	0.2	2.8					-25.49
469493	49	4.6	2.4					-25.53
469492	48	1.6	0.7					-25.55
469491	47	2.4	0.9					-24.82
469490	46.1	2.5	0.8					-24.96
469489	45.8	11.1	0.0	-2.28	0.03	-4.40	0.03	
469488	45.6	21.6						
469487	45.4	25.3		-1.92	0.03	-3.61	0.03	
469486	45.2	14.2						
469485	45	16.3	0.0					-25.11
469484	44.8	16.8		-2.33	0.01	-5.89	0.01	
469483	44.6	15.3						
469482	44.4	17.9		-2.05	0.01	-5.00	0.02	
469481	44.2	10.0						
469480	44	16.8	0.2					-25.16
469479	43.8	9.5						
469478	43.6	14.2		-3.02	0.02	-2.10	0.01	
469477	43.4	10.0						
469476	43.2	5.8						
469475	43.0	8.4	0.0	-4.12	0.02	-3.88	0.01	-26.37
469474	42.8	0.5						
469473	42.6	5.8						
469472	42.4	4.2						
469471	42.2	6.3						
469470	42	10.5	0.1	-6.75	0.02	-5.44	0.03	-24.84
469469	41.8	10.5						
469468	41.6	13.4						
469467	41.4	16.3		-2.50	0.02	-5.25	0.01	
469466	41.2	25.8						
469465	41.1	12.1	0.2	-7.69	0.01	-6.14	0.01	-25.17
469464	40.9	15.8	0.3	-9.35	0.04	-7.35	0.05	-23.18
469463	40.8	26.8		-10.02	0.02	-6.42	0.05	
469462	40.6	8.4		-6.70	0.01	-7.75	0.01	
469461	40.4	7.9		-7.65	0.01	-8.06	0.02	-23.12
469460	40.2	6.3		-7.12	0.02	-7.66	0.02	
469459	40	5.8	0.3					-23.61
469458	39.8	5.3						-23.01
469457	36.2	4.2						
469456	36	10.0	0.0	-2.02	0.01	-8.66	0.02	
469455	35.8	11.1		-8.37	0.01	-5.98	0.03	
469454	35.6	7.4		-0.27	0.01	-8.25	0.02	-23.89
469453	35.4	11.6		-7.82	0.01	-6.80	0.03	-26.12
469452	35	0.0						
469451	35	0.0	0.0					-23.95
469450	35	0.0						
469449	34.6	16.8						
469448	34	5.8						-20.88
469447	34	16.8						
469446	34	5.8	0.5					-24.06
469445	34	6.3						
469444	34	23.7						
469443	33	24.2						-21.84
469442	33	29.0						
n		157	63	49		49		70

Sample no.	m	$CaCO_3$ [%]	TOC [%]	$\delta^{13}C_{carb}$ [‰]	±s	$\delta^{18}O_{carb}$ [‰]	±s	$\delta^{13}C_{org}$ [‰]
469441	33	4.3	0.4	-2.48	0.03	-5.49	0.04	-24.48
469440	32.8	5.3						
469439	33	1.6						
469438	32.4	5.3						-23.90
469437	32	2.6						
469436	32	1.4	0.1					-24.29
469435	32	5.3						
469434	31.6	4.7						
469433	31.4	2.6						-24.76
469432	31.2	2.6						
469431	31.0	5.3	0.4					-25.04
469430	31	6.8		-4.12	0.02	-6.67	0.03	
469429	30.6	7.4		-2.49	0.02	-5.51	0.02	
469428	30	5.8						-23.34
469427	30.2	5.3						
469426	30	6.3	0.3					-25.78
469425	29.8	6.3						
469424	29.6	11.1						
469423	29.4	7.4		-3.41	0.02	-5.88	0.03	-25.43
469422	29.2	7.4		-3.73	0.02	-5.30	0.01	
469421	29.0	12.0	0.6					-25.73
469420	28.8	6.8		-8.75	0.02	-10.08	0.05	
469419	28.6	7.9		-4.43	0.01	-3.93	0.03	
469418	28.4	9.5		-3.95	0.02	-4.76	0.02	
469417	28.2	9.0						
469416	28	9.0	0.3					-24.63
469415	27.8	15.3		-4.46	0.02	-5.15	0.02	
469414	27.6	20.5		-7.88	0.02	-6.73	0.02	
469413	27.4	7.4		-3.55	0.02	-5.33	0.02	
469412	27.2	10.5						
469411	27.0	11.1	0.1	-6.19	0.02	-4.90	0.01	-24.14
469410	26.8	10.0						
469409	26.6	11.6		-5.99	0.03	-4.91	0.03	
469408	26.4	10.5						
469407	26.2	11.1		-4.98	0.02	-4.17	0.04	
469406	26	5.8	0.2					-24.07
469405	25.8	6.3						
469404	25.6	7.4						
469403	25.4	7.9		-2.92	0.01	-5.05	0.03	
469402	25.2	10.0						
469401	25.0	10.0	0.1	-2.75	0.03	-5.19	0.02	-25.46
469399	24.8	8.4						
469398	24.6	9.5						
469397	24.4	11.1						
469396	24.2	10.5		-2.85	0.01	-4.54	0.02	
469395	24	9.5	0.7					-23.94
469394	23.8	10.0						
469393	23.6	10.0		-1.71	0.03	-4.71	0.03	
469392	23.4	13.7						
469391	23.2	11.1		-3.10	0.01	-4.56	0.01	
469390	23.0	15.8	1.9					
469389	22.8	23.7						
469388	22.6	15.8		-7.39	0.02	-5.55	0.02	
469387	22.4	13.7						
469386	22.2	16.3		-7.85	0.06	-4.84	0.07	
469385	22	14.7	0.2					-24.71
469384	21.8	13.2		-3.45	0.02	-5.54	0.03	
469383	21.6	11.1						
469382	21.4	11.1		-1.91	0.03	-5.99	0.03	
469381	21.2	5.8						
469380	21.0	13.2	0.3					-25.13
469379	20.8	15.8		-4.03	0.04	-5.61	0.04	
469378	20.6	14.7						
469377	20.4	16.3		-3.95	0.04	-6.06	0.05	
469376	20.2	16.3						
469375	20	14.7	0.1	-2.41	0.02	-4.48	0.04	-26.04
469374	19.8	13.9		-1.80	0.02	-5.56	0.02	
469373	19.6	13.9						
469372	19.4	24.2		-7.90	0.02	-8.21	0.03	
469371	19.2	20.0		-6.89	0.02	-7.40	0.03	
469370	19	15.3	0.2	-7.28	0.02	-6.90	0.04	-25.07
469369	18.9	0.2						-27.66
469368	18	0.0	4.0					
469365	15	0.0	2.1					-27.63
469360	10	0.0	3.5					-28.06
469355	5	0.0	4.0					-28.17
469351	0	0.0	3.6					-27.28
n		157	63	49		49		70

Table 2. $CaCO_3$ (from Pauly *et al*. 2012b) and TOC contents, $\delta^{13}C_{carb}$ and $\delta^{13}C_{org}$ values of the Perisphinctes Ravine section (Kuhn Ø)

Sample no.	m	$CaCO_3$ [%]	TOC [%]	$\delta^{13}C_{carb}$ [‰]	±s	$\delta^{18}O_{carb}$ [‰]	±s	$\delta^{13}C_{org}$ [‰]
518278	41.5	0.5	1.1					-24.24
518277	41.25	0.5						
518276	41	0.8	0.6					-22.53
518275	40.75	0.0						
518274	40.5	1.0						-23.89
518273	40.25	0.0						
518272	40	0.5	0.4					-24.57
518271	39.75	0.0						
518270	39.5	0.0						-24.94
518269	39.25	0.5						
518268	39	0.1	0.3					-24.80
518267	38.75	0.0						
518266	38.5	0.5						-24.93
518265	38.25	1.5						
518264	38	3.9	0.3					-24.64
518263	37.5	30.2	0.2					-25.30
518262	36.5	0.0						-25.17
518261	35.5	0.0						-26.83
518260	34.5	0.3	0.0					
518259	33.5	0.0						-26.99
518258	32.5	0.0						-25.24
518257	32.25	0.0						-24.51
518256	32	0.0	0.1					
518255	31.75	0.0						-25.14
518254	31.5	1.0						-24.61
518253	31.25	1.0						-24.97
518252	31	3.4						-24.16
518251	30.75	2.4						-25.23
518250	30.5	0.5						-25.06
518249	30.25	3.4						-25.22
518248	30	2.0	0.4					-24.61
518247	29.75	4.4						-24.87
518246	29.5	5.3						-25.20
518245	29.25	0.5						-25.20
518244	29	0.5						-25.03
518243	28.75	2.4						-24.54
518242	28.5	4.4						-24.51
518241	28.25	4.4						-24.83
518240	28	3.4	0.8					-25.16
518239	27.75	0.0						-24.85
518238	27.5	0.5						-24.73
518237	27.25	0.0						-25.23
518236	27	6.3		-0.80	0.00	-6.79	0.00	-24.69
518235	26.75	2.4						
518234	26.5	1.0						-25.12
518233	26.25	3.9						
518232	26	3.9	1.1					-25.02
518231	25.75	1.5						
518230	25.5	2.0						
518229	25.25	5.9		-3.22	0.01	-6.44	0.02	
518228	25	4.4						
518227	24.75	1.5						
518226	24.5	5.4						
518225	24.25	1.0						
518224	24	2.9	0.8					-25.11
518223	23.75	5.9						
518222	23.5	5.4						
518221	23.25	5.4						
518220	23	5.4						
518219	22.75	6.4		-3.12	0.00	-6.00	0.01	
518218	22.5	5.4						
518217	22.25	4.4						
518216	22	4.9	0.6					-24.61
518215	21.75	1.1						
518214	21.5	4.4						
518213	21.25	5.9						
518212	21	6.3		-2.12	0.01	-5.76	0.02	
518211	20.75	5.9						
518210	20.5	7.3		-2.44	0.01	-7.07	0.02	
518209	20.25	6.3		-2.77	0.00	-6.83	0.01	
518208	20	8.8	1.5	-2.76	0.01	-6.32	0.01	-24.30
518207	19.75	9.3		-2.90	0.00	-6.49	0.01	
518206	19.5	5.4						
518205	19.25	8.8		-1.66	0.01	-6.46	0.01	
518204	19	11.6		-2.82	0.00	-5.45	0.02	
518203	18.75	16.8		-5.60	0.01	-4.79	0.01	
518202	18.5	8.4		-1.57	0.00	-6.43	0.01	
518201	18.25	7.9		-1.85	0.01	-6.02	0.03	
518199	18	6.3	1.3	-2.79	0.00	-6.41	0.02	-25.07
n		140	25	53		53		49

Sample no.	m	$CaCO_3$ [%]	TOC [%]	$\delta^{13}C_{carb}$ [‰]	±s	$\delta^{18}O_{carb}$ [‰]	±s	$\delta^{13}C_{org}$ [‰]
518198	17.75	6.3		-3.13	0.00	-5.51	0.02	
518197	17.5	7.8		-3.42	0.00	-5.73	0.01	
518196	17.25	7.4		-3.02	0.01	-6.04	0.01	
518195	17	8.4		-4.23	0.00	-5.49	0.02	
518194	16.75	7.4		-2.44	0.00	-5.52	0.01	
518193	16.5	9.5		-3.47	0.01	-4.55	0.01	
518192	16.25	11.2		-3.83	0.00	-5.62	0.00	
518191	16	7.8	1.2	-2.22	0.01	-4.62	0.02	-25.09
518190	15.75	5.8						
518189	15.5	5.8						
518188	15.25	12.6						
518187	15	6.3		-3.08	0.00	-5.84	0.01	
518186	14.75	10.0		-4.62	0.01	-5.22	0.01	
518185	14.5	11.2		-5.15	0.01	-3.93	0.03	
518184	14.25	5.8						
518183	14	5.8	0.6					-24.82
518182	13.75	8.4		-1.78	0.00	-3.42	0.01	
518181	13.5	6.3		-3.16	0.01	-5.07	0.01	
518180	13.25	6.8		-2.74	0.01	-4.82	0.03	
518179	13	9.3		-3.38	0.00	-4.77	0.01	
518178	12.75	6.3		-2.21	0.01	-6.06	0.03	
518177	12.5	5.8						
518176	12.25	5.8						
518175	12	6.3	0.3	-3.46	0.00	-6.20	0.01	-24.59
518174	11.75	5.3						
518173	11.5	17.1		-8.41	0.00	-6.24	0.00	
518172	11.25	13.7		-10.63	0.01	-4.40	0.02	
518171	11	22.6		-7.17	0.00	-6.67	0.01	
518170	10.75	13.2		-8.95	0.00	-7.30	0.01	
518169	10.5	6.3		-1.40	0.01	-5.45	0.02	
518168	10.25	7.4		-2.01	0.00	-5.35	0.01	-25.12
518167	10	16.3	0.1	-11.12	0.00	-4.20	0.01	
518166	9.75	7.4		-3.76	0.01	-4.35	0.01	
518165	9.5	10.7		-7.75	0.01	-3.20	0.01	
518164	9.25	8.4		-3.89	0.00	-4.47	0.01	
518163	9	10.0		-3.68	0.00	-4.84	0.01	
518162	8.75	6.3		-1.70	0.00	-5.91	0.02	
518161	8.5	5.3						
518160	8.25	5.8						
518159	8	7.4	0.4	-2.49	0.00	-6.85	0.02	-25.25
518158	7.75	8.4		-2.47	0.00	-6.82	0.02	
518157	7.5	4.7						
518156	7.25	0.5						
518155	7	0.0						
518154	6.75	10.0		-1.67	0.00	-5.05	0.01	
518153	6.5	18.4		-3.85	0.00	-5.35	0.02	
518152	6.25	13.7		-2.09	0.01	-4.74	0.01	
518151	6	32.0	0.3	-6.12	0.00	-6.62	0.01	-25.05
518150	5.75	17.9		-5.35	0.00	-6.02	0.01	
518149	5.5	18.4		-5.24	0.00	-5.83	0.01	
518148	5.25	5.8						
518147	5	5.3						
518146	4.75	5.8						
518145	4.5	2.6						
518144	4.25	6.3		-3.79	0.01	-4.83	0.01	
518143	4.1	7.4	0.4	-5.52	0.00	-3.75	0.02	-25.63
518142	3.9	0.0	1.8					-27.47
518141	3	0.0						
518140	2	0.0	3.9					-27.66
518139	1	0.0						
518138	0	0.0	4.2					
n		140	25	53		53		49

Rødryggen Member (38–42 m, 8 samples): The initial interval shows $\delta^{13}C_{org}$ values around -25‰ followed by a peak towards -22.5‰.

Total organic carbon (TOC)

TOC contents are shown in Fig. 2. The black mudstones of the Rødryggen section show a TOC content averaging 3.4% (2.1–4.0%, 5 samples), the Ryazanian–Valanginian mudstones of the Albrechts Bugt Member averaging 0.4% (0–1.9%, 20 samples), the Hauterivian Rødryggen Member averaging 0.1% (0–2.2%, 6 samples) and the Barremian black mudstones averaging 1.1% (0.6–2.8%, 32 samples). The samples from the Perisphinctes Ravine section yield slightly higher TOC contents than those from the Rødryggen section. The underlying black mudstones have a TOC content averaging 3.3% (1.8–4.2%, 3 samples), the mudstones of the Albrechts Bugt and Rødryggen Members average 0.6% (0–1.4%, 17 samples) and 0.5% (0.3–1.2%, 5 samples), respectively.

Major and trace elements

All major and trace element data are documented in the Supplementary data files 1 and 2 available at the web site http://2dgf.dk/publikationer/bulletin/191bull61.html.

Triangular diagrams for both sections, showing the three major chemical components Al_2O_3 (clay minerals), CaO ($CaCO_3$) and SiO_2 (quartz), are illustrated in Fig. 3. In order to centre the data in the graph, arbitrary multipliers (Al_2O_3×5 and CaO×2) were used. Additionally, the composition of average shale following Wedepohl (1971, 1991) is given for comparison. Sediments are composed of a mixture of average shale components with varying amounts of calcium carbonate. A few samples from the Albrechts Bugt Member have higher calcium carbonate or quartz contents compared to the majority of sediments. The Barremian mudstones have in contrast a higher proportion of clay minerals. Relatively high average correlation coefficients of the sections have been observed between SiO_2, Al_2O_3, K_2O, TiO_2 and with trace elements Zr and Rb (except Ba), representing the detrital origin of these elements (Table 3).

Concentrations of all analyzed elements were normalized with respect to Al (element/Al ratios) to compensate for calcium dilution. Major element ratios are expressed as weight ratios, trace element ratios are expressed as weight ratios multiplied by 10^4. This normalization enables one to observe also minor variations in the chemical composition, which otherwise would be masked by changes in the calcium carbonate content. Sediments of the Bernbjerg Formation and Albrechts Bugt Member yield relatively stable Al (Al_2O_3) concentrations similar to average shale (according to Wedepohl 1971, 1991; Table 4). Al concentrations of the Rødryggen Member show a slight decrease in the samples of the Rødryggen section; no major changes have been observed for the Perisphinctes Ravine section. The Barremian black mudstones have the highest Al concentrations.

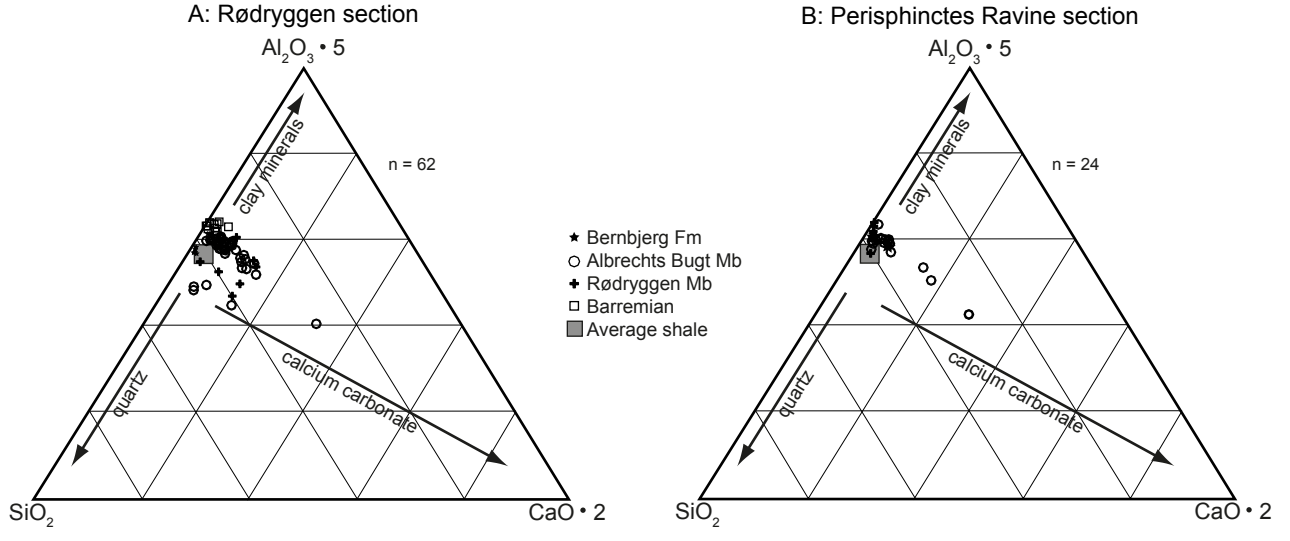

Fig. 3. Ternary diagrams of Al_2O_3×5 – CaO×2 – SiO_2 for the studied sections illustrating the composition of the sediments of the Bernbjerg Formation, Albrechts Bugt and Rødryggen Members and Barremian, in comparison to average shale (Wedepohl 1971, 1991).

Table 3. Correlation coefficients for selected major and trace elements for the Rødryggen and Perisphinctes Ravine sections

Rødryggen section						**Perisphinctes Ravine section**					
	r		r		r		r		r		r
	n = 62		n = 62 (TOC n = 32)		n = 62		n = 24		n = 24		n = 24
SiO_2 - TiO_2	0.440	Al_2O_3 - Co	0.458	U - V	0.605	SiO_2 - TiO_2	0.930	Al_2O_3 - Co	0.034	U - V	0.222
SiO_2 -Al_2O_3	0.396	Al_2O_3 - Cr	0.421	U - Zn	0.284	SiO_2 -Al_2O_3	0.906	Al_2O_3 - Cr	0.035	U - Zn	0.280
SiO_2 - K_2O	0.535	Al_2O_3 - Cu	0.036	U - Cr	0.333	SiO_2 - K_2O	0.911	Al_2O_3 - Cu	0.452	U - Cr	0.222
SiO_2 - Ba	0.295	Al_2O_3 - Mo	-0.009	U - Cu	0.099	SiO_2 - Ba	0.238	Al_2O_3 - Mo	0.275	U - Cu	0.054
SiO_2 - Rb	0.509	Al_2O_3 - Ni	0.469	V - Zn	0.498	SiO_2 - Rb	0.900	Al_2O_3 - Ni	0.059	V - Zn	-0.166
SiO_2 - Zr	0.551	Al_2O_3 - U	0.257	V - Cr	0.529	SiO_2 - Zr	0.685	Al_2O_3 - U	0.239	V - Cr	0.407
TiO_2 - K_2O	0.951	Al_2O_3 - V	0.116	V - Cu	0.011	TiO_2 - K_2O	0.928	Al_2O_3 - V	0.088	V - Cu	-0.419
TiO_2 - Al_2O_3	0.917	Al_2O_3 - Zn	0.035	Zn - Cr	0.425	TiO_2 - Al_2O_3	0.967	Al_2O_3 - Zn	0.385	Zn - Cr	-0.040
TiO_2 - Ba	0.071	TOC - Co/Al	-0.586	Zn - Cu	0.387	TiO_2 - Ba	0.431	TOC - Co/Al	-0.128	Zn - Cu	0.736
TiO_2 - Rb	0.881	TOC - Cr/Al	0.367	Cr - Cu	0.178	TiO_2 - Rb	0.937	TOC - Cr/Al	0.393	Cr - Cu	-0.061
TiO_2 - Zr	-0.023	TOC - Cu/Al	-0.303			TiO_2 - Zr	0.730	TOC - Cu/Al	-0.548		
Al_2O_3 - K_2O	0.927	TOC - Mo/Al	0.646			Al_2O_3 - K_2O	0.904	TOC - Mo/Al	0.729		
Al_2O_3 - Ba	0.053	TOC - Ni/Al	-0.608			Al_2O_3 - Ba	0.367	TOC - Ni/Al	-0.053		
Al_2O_3 - Rb	0.932	TOC - U/Al	0.559			Al_2O_3 - Rb	0.972	TOC - U/Al	0.210		
Al_2O_3 - Zr	-0.209	TOC - V/Al	0.620			Al_2O_3 - Zr	0.617	TOC - V/Al	0.914		
K_2O - Ba	0.068	TOC - Zn/Al	-0.038			K_2O - Ba	0.169	TOC - Zn/Al	-0.249		
K_2O - Rb	0.960	Mo - U	0.560			K_2O - Rb	0.982	Mo - U	0.285		
K_2O - Zr	0.004	Mo - V	0.721			K_2O - Zr	0.773	Mo - V	0.926		
Ba - Rb	0.118	Mo - Zn	0.012			Ba - Rb	0.104	Mo - Zn	-0.208		
Ba - Zr	0.206	Mo - Cr	0.265			Ba - Zr	0.277	Mo - Cr	0.266		
Rb - Zr	-0.069	Mo - Cu	-0.153			Rb - Zr	0.777	Mo - Cu	0.429		

Table 4. Average major and trace element/Al ratios for the different lithological units of the Rødryggen and Perisphinctes Ravine sections

	Rødryggen section				**Perisphinctes Ravine section**			
	Bernbjerg Fm.	Albrechts Bugt Mb.	Rødryggen Mb.	Barremian	Bernbjerg Fm.	Albrechts Bugt Mb.	Rødryggen Mb.	average shale Wedepohl 1971, 1991
	n = 6	n = 32	n = 8	n = 16	n = 3	n = 17	n = 4	
CaCO3 [%]	0.2	10.4 (n = 94)	12.7 (n = 25)	2.1 (n = 32)	0	6.5 (n = 120)	0.6 (n = 15)	3.9
TOC [%]	3.4 (n = 5)	0.4 (n = 20)	0.1 (n = 6)	1.1 (n = 32)	3.3	0.6	0.5 (n = 5)	0.2
Al [%]	8.83	8.86	8.16	10.28	9.13	9.07	10.01	8.89
Si/Al	2.92	2.83	2.95	2.53	2.73	2.72	2.64	3.05
Ti/Al	0.049	0.051	0.051	0.057	0.048	0.051	0.051	0.053
Fe/Al	0.43	0.46	0.65	0.42	0.37	0.53	0.65	0.54
K/Al	0.24	0.24	0.25	0.26	0.25	0.26	0.28	0.32
Ba/Al	69	69	70	56	60	73	63	65
Co/Al	0.1	1.7	1.5	2.0	0.6	1.8	1.5	2.1
Cr/Al	13.8	9.2	11.4	11.2	12.7	9.9	11.4	10.1
Cu/Al	4	5	2	5	2	4	4	10
Mo/Al	6.19	–	–	–	2.48	–	–	0.15
Ni/Al	1.6	4.5	6.2	6.1	3.6	5.8	6.2	7.6
Pb/Al	3.1	2.7	3.3	2.5	3.0	2.8	2.3	2.5
Rb/Al	12.57	12.44	13.07	12.30	12.60	13.50	14.24	15.75
Sr/Al	16.90	27.92	35.00	11.57	15.68	25.58	12.95	33.75
U/Al	0.893	0.533	0.525	0.498	0.695	0.524	0.448	0.416
V/Al	58	15	19	23	39	16	18	15
Zn/Al	11	9	9	11	9	9	9	11
Zr/Al	20	28	35	25	20	24	25	18

Major element ratios are given as weight ratios; trace element ratios are expressed as weight ratios multiplied by10^4

Major element/Al ratios (Si, Ti, K, Zr), being important for the characterization of the detrital matter content, are given in Figs. 4, 5. Si/Al and Zr/Al are relatively constant throughout the studied interval, but both show distinctive peaks in the uppermost part of the Albrechts Bugt Member of the Rødryggen section. Ti/Al and K/Al underlie a relatively stable developing in the Bernbjerg Formation – Rødryggen Member but they show higher values in the Barremian. Fe concentrations are on average higher in the Rødryggen Member in contrast to the remaining sediments (Table 4).

In the Rødryggen section, Sr/Al ratios show a strong correlation with the calcium carbonate content; in the Perisphinctes Ravine section this is less pronounced. Ba/Al ratios are similar to average shale throughout the studied intervals, peaking in the lower part of the Albrechts Bugt Member and have lower values in the Barremian.

Redox-sensitive trace elements (Cr, Mo, U, V, Zn) hold relatively high element/Al ratios in the TOC rich Bernbjerg Formation (Figs. 6, 7). Cu/Al and Cr/Al ratios show also marked peaks in the TOC poor Albrechts Bugt and Rødryggen Members. Co, Cu and Ni have varying element/Al ratios, which are below the values of average shale (Table 4). A strong correlation between Co and Ni has been observed in both sections ($r = 0.767$ and $r = 0.974$). The Bernbjerg Formation constitutes a depletion of Co and Ni. Correlation factors between the redox-sensitive elements mutually, as well as between redox-sensitive elements and TOC (Table 3) are relatively high especially for Mo, U and V; they show, however, a relatively low correlation with Al_2O_3.

Discussion

Carbon isotopes

The carbon isotope record of the Cretaceous is marked by several excursions related to perturbations of the carbon cycle (e.g. Weissert 1989; Weissert & Chanell 1989; Menegatti *et al*. 1998; Weissert & Erba 2004; Jenkyns 2010). A prominent feature of the earliest Cretaceous is the mid-Valanginian $\delta^{13}C$-excursion (Lini *et al*. 1992; Channell *et al*. 1993; Weissert & Erba 2004), which is characterized by an excursion from 1 to 3‰. The $\delta^{13}C$-isotope event is documented in the marine carbonate reservoirs, fossil shell material (e.g. belemnite guards) terrestrial (i.e. land plants) and marine organic matter (e.g. Gröcke *et al*. 1999, 2003, 2005; Ferreri *et al*. 1997; Aguirre-Urreta *et al*. 2008; Nunn *et al*. 2010), suggesting this event to be global.

The $\delta^{13}C_{carb}$ values observed in this study (Fig. 2) are on average much lighter than contemporaneous values presented for the Tethyan bulk-rock carbonate (1–3‰) (Weissert & Erba 2004) and belemnite guards (-2 to 1‰) (McArthur *et al*. 2007). Swientek (2003) studied Kimmeridgian–Barremian sediments from Norway and the Barents Sea showing similar $\delta^{13}C_{carb}$ values (-15.5 to 0.3‰) to those of Greenland. The ^{13}C depletion may be explained by early diagenesis accompanied by microbial decomposition of organic matter. Bacterial sulfate reduction and methanogenesis coupled with authigenic carbonate precipitation may have altered the isotopic composition of the sediments (e.g. Berner 1981; Lein 2004; Decampo 2010). Microbial processes produce additional bicarbonate (HCO_3^-), shifting the $\delta^{13}C_{carb}$ composition towards values similar to those of $\delta^{13}C_{org}$ (-28 to -20‰). If methanogenesis would have affected the isotopic composition, $\delta^{13}C_{carb}$ values were expected to be much lighter than those observed. Well-preserved calcareous nannofossils constitute a significant carbonate source in samples with low carbonate contents (Pauly *et al*. 2012b). Samples having relatively high carbonate contents are characterized by moderate to poorly preserved nannofossil assemblages, micrite-rich or even barren samples, which support the consideration of authigenic carbonate precipitation.

The $\delta^{13}C_{org}$ values of the investigated sediments (average -25‰; Fig. 2) are similar to $\delta^{13}C_{org}$ values recorded for marine sediments from offshore Morocco, France and Poland (Wortmann & Weissert 2000; Kujau *et al*. 2013), allowing us to exclude major diagenetic alteration. The $\delta^{13}C_{org}$ values of the TOC-rich Bernbjerg Formation are slightly lighter (2–3‰) than those of the remaining sediments. This ^{13}C depletion may indicate bacterial sulfate reduction, which is very likely in the oxygen-depleted depositional environment of the Bernbjerg Formation (Surlyk 1977; Strogen et al 2005). The $\delta^{13}C_{org}$ values of the Albrechts Bugt Member, Rødryggen Member and Barremian are relatively stable (around -25‰). Strong deviations may indicate a poor preservation of organic matter, changing ratios of marine and terrestrial organic matter, or early diagenesis (bacterial sulfate reduction and authigenic carbonate formation). The well-defined $\delta^{13}C$ excursion, however, is not recorded in the Valanginian sediments from North-East Greenland, either due to the high condensation of the strata and the related sample density, or a hiatus in the sedimentary record.

Major and trace elements

The studied sediments show a significant input of terrigenous material (quartz, clay minerals) similar to average shale and with varying biogenic calcium

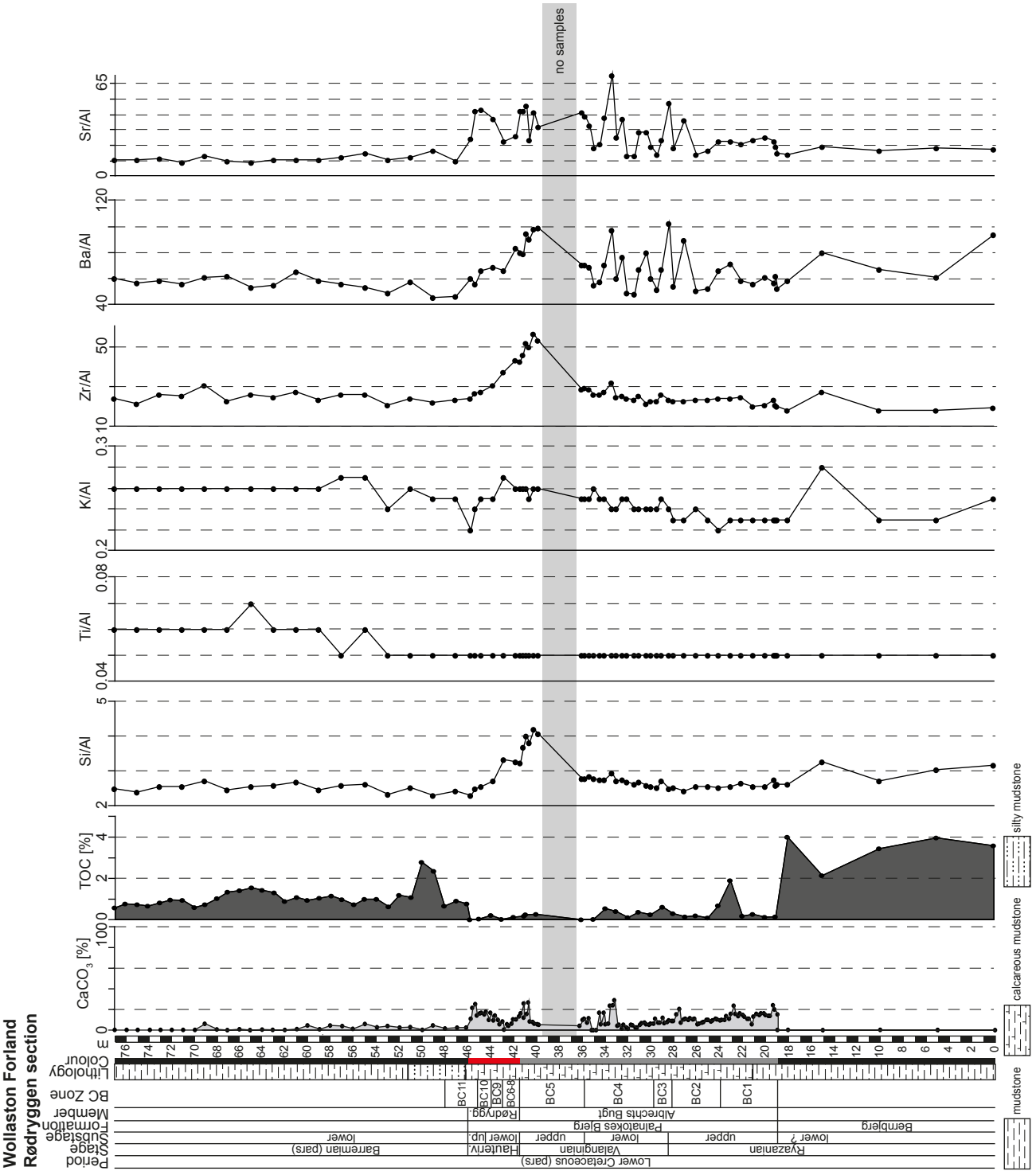

Fig. 4. Lithological log of the Rødryggen section showing the Boreal calcareous nannofossil (BC) zones and $CaCO_3$ (from Pauly *et al*. 2012b) and TOC contents, Si/Al, Ti/Al, K/Al, Zr/Al, Ba/Al and Sr/Al ratios. Major element ratios are given as weight ratios; trace element ratios are expressed as weight ratios multiplied by 10^4.

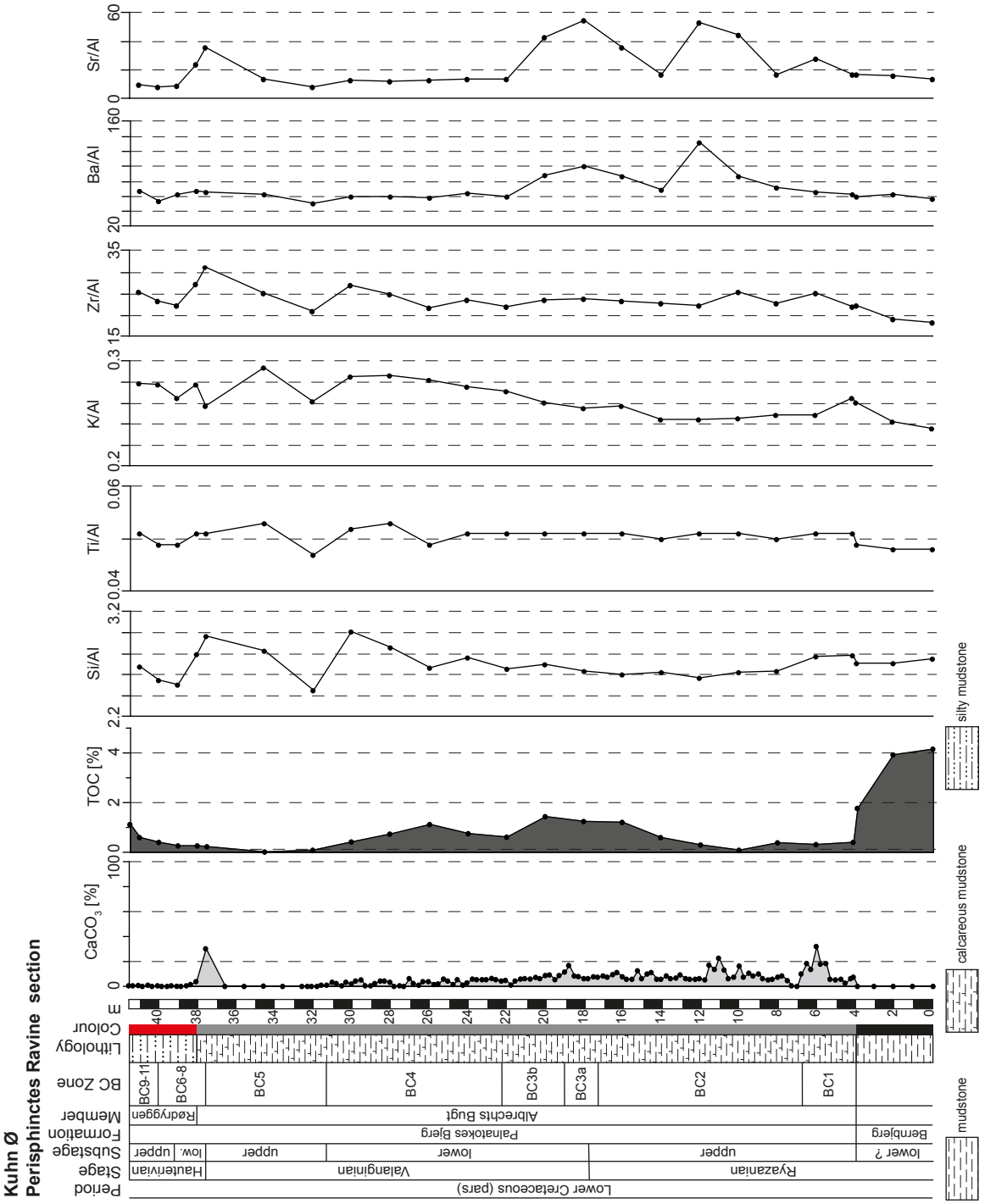

Fig. 5. Lithological log of the Perisphinctes Ravine section showing the Boreal calcareous nannofossil (BC) zones and $CaCO_3$ (from Pauly *et al*. 2012b) and TOC contents, Si/Al, Ti/Al, K/Al, Zr/Al, Ba/Al and Sr/Al ratios. Major element ratios are given as weight ratios; trace element ratios are expressed as weight ratios multiplied by 10^4.

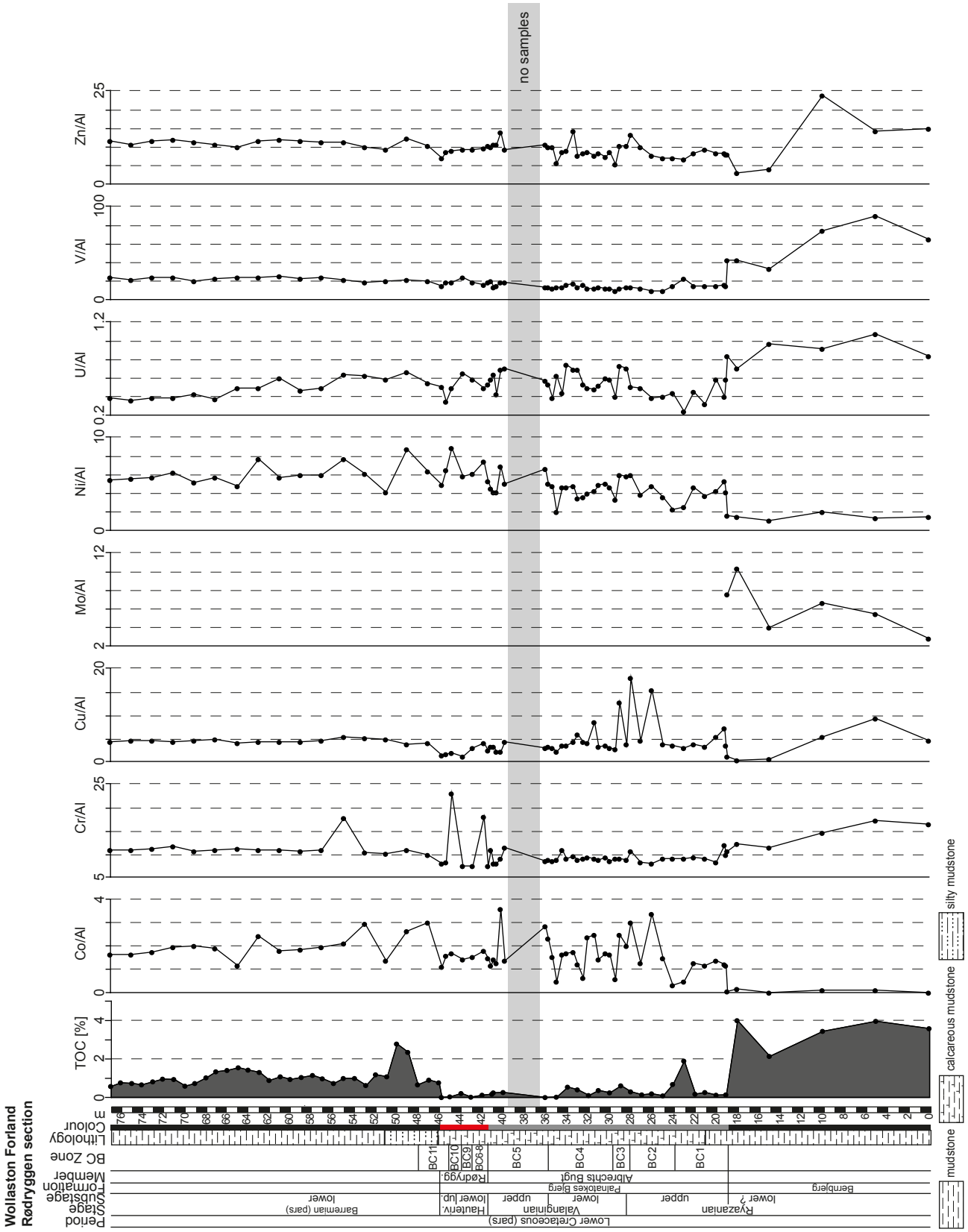

Fig. 6. Lithological log of the Rødryggen section (BC zones from Pauly *et al*. 2012b) showing the TOC contents, Co/Al, Cr/Al, Cu/Al, Mo/Al, Ni/Al, U/Al, V/Al and Zn/Al ratios. Trace element/Al ratios are given as weight ratios multiplied by 10^4.

carbonate concentrations. Although the lithology is relatively uniform throughout the sections, minor variations in the composition of the detrital matter have been observed. These are manifested in changing Si/Al (quartz, clay minerals), K/Al (clay minerals) and Zr/Al (heavy minerals) ratios. The Barremian sediments show increased Ti/Al ratios (heavy minerals) and a higher clay mineral content, which correlate well with the observed increase of the K/Al ratios (Fig. 4, 5).

Major mechanisms controlling the concentration of the trace elements are the rate of terrigenous input, redox conditions during deposition, and the coupling to biogenic cycles in the water column. Strontium shows a strong correlation with Ca because it is fixed

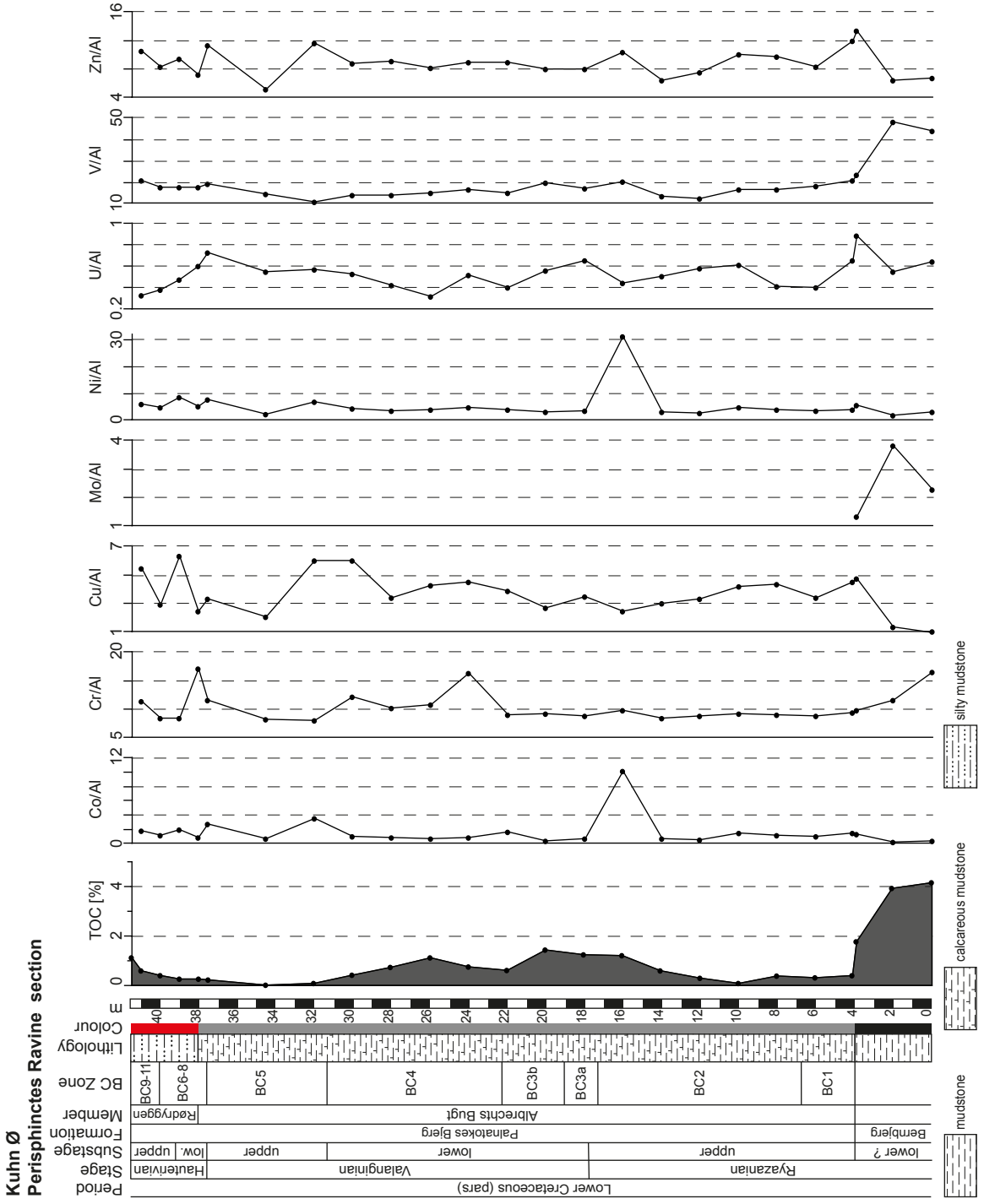

Fig. 7. Lithological log of the Perisphinctes Ravine section (BC zones from Pauly *et al.* 2012b) showing the TOC contents, Co/Al, Cr/Al, Cu/Al, Mo/Al, Ni/Al, U/Al, V/Al and Zn/Al ratios. Trace element/Al ratios are given as weight ratios multiplied by 10^4.

in the carbonate lattice where it can substitute Ca. Barium is considered to be indicative for high palaeoproductivity (e.g. McManus *et al*. 1998; Gingele *et al*. 1999; Bains *et al*. 2000; Prakash Babu *et al*. 2002). The observed Ba/Al ratios suggest an average productivity for the Ryazanian–Hauterivian with phases of increased productivity during the early Valanginian and a reduced productivity in the Barremian, which is in accordance with the total nannofossil abundance (Pauly *et al*. 2012b).

Redox-sensitive trace elements (Cr, Mo, U, V, Zn) in organic-rich sediments are commonly used as indicators for redox conditions during deposition (e.g. Brumsack & Gieskes 1983; Algeo & Maynard 2004; Tribovillard *et al*. 2004, 2005, 2006; Brumsack 2006). Under anoxic conditions, Mo, V and U show a relatively low enrichment in the sediment but a relatively high correlation with TOC, because the uptake of trace elements is mainly limited by the availability of organic matter (Algeo & Maynard 2004, Tribovillard *et al*. 2006). Under euxinic conditions (free H_2S), insoluble metal sulphides or oxyhydroxides can precipitate directly from the water column or at the sediment–water interface, which results in strong enrichments of Mo, V and U and weak correlations with TOC (Algeo & Maynard, 2004; Tribovillard *et al*. 2004, 2006). The sediments of the Bernbjerg Formation show a good correlation of trace elements (Mo,V, U) with TOC (Figs 6,7; Table 3), implying coupling to organic matter. Although a concurrent enrichment in U, V and Mo could be recognized, concentrations of redox-sensitive trace elements are mostly lower (e.g. Mo: average 50 ppm, max. 100 ppm) in comparison to modern euxinic environments (Mo: 70–160 ppm) observed by e.g. Lyons *et al*. (2009). The enrichment of the redox-sensitive elements (Mo, U, V) together with relatively high TOC concentrations in the Bernbjerg Formation thus indicates predominantly anoxic bottom water conditions with occasional free H_2S.

Observed peaks of Cu and Cr in the well-oxygenated Albrechts Bugt and Rødryggen Members are suggestive of a detrital origin, these elements residing in oxides or hydroxides. Cobalt has a chemical behaviour like Mn, forming insoluble sulphide (CoS) that can be taken up in solid solution by authigenic Fe-sulphides (Huerta-Diaz & Morse 1992; Algeo & Maynard 2004). Cobalt concentrations may be limited in authigenic sulphides as Co uptake is kinetically slow (Morse & Luther 1999). It is also uncertain to which extent Co is influenced by the Fe–Mn redox cycling (Algeo & Maynard 2004). The depletion of Ni in the Bernbjerg Formation, which on the other hand is enriched in redox-sensitive trace elements, may imply lowered Ni concentrations in the seawater or post-sedimentary diagenesis. The depletion of Co and Cu in the seawater in the Greenland–Norwegian Seaway is probably related to decreased sediment transport that may explain the low concentrations of these elements in comparison to average shale. Following Tribovillard *et al.* (2006) Co is under a strong detrital influence that rather limits the use as a reliable redox proxy.

Depositional environment

The Bernbjerg Formation (Kimmeridgian/early Ryazanian), composed of black, rhythmically laminated, non-bioturbated, silt-rich mudstones, has been viewed as a low-energy, euxinic shelf facies (Surlyk 1977; Surlyk & Clemmensen 1975a; Surlyk & Clemmensen 1983). Relatively high contents of organic matter and the enrichment of redox-sensitive trace elements support the interpretation of anoxic bottom water conditions with occasional free H_2S during the deposition of this formation (Fig. 8), similar to the Volgian–Ryazanian sedimentary units of mid and north Norway (Mutterlose *et al*. 2003).

The Albrechts Bugt Member (late Ryazanian to Valanginian), consisting of light grey laminated calcareous mudstones, is characterized by low TOC contents, rich benthic fauna, common trace fossils (*Zoophycos*, *Thalassinoides*), ammonites, belemnites, brachiopods and bivalves (Surlyk & Clemmensen 1975a; Surlyk 1978; Alsen 2006; Alsen & Mutterlose 2009). Calcareous nannofossils and unidentifiable micrite constitute the major carbonate source of the Albrechts Bugt Member (Pauly *et al*. 2012b), forming thereby the first calcareous sediments in North-East Greenland since the late Permian (Maync 1949; Alsen 2006). The sedimentological, palaeontological and geochemical analyses indicate a low-energy open marine shelf environment below the storm wave base, hemipelagic sedimentation of fine-grained terrigenous material, biogenic carbonate production, and well-oxygenated sea-floor conditions. Surface water temperatures were cool to cold with changing surface water fertility (mesotrophic–oligotrophic) as suggested by fluctuation of the calcareous nannofossil assemblages (Pauly *et al*. 2012b) and varying Ba concentrations.

The Rødryggen Member (Hauterivian) is composed of red, calcareous mudstones with almost no sedimentary structures (Surlyk & Clemmensen 1975a). Similar to the underlying Albrechts Bugt Member, the calcium carbonate is derived mainly from calcareous nannofossils and unidentifiable micrite (Pauly *et al*. 2012b). The colour is based on a high content of oxidized iron minerals (haematite and goethite), derived from weathering in the hinterland (Alsen 2006). This view is promoted by the observed increase of Fe/Al ratios and increased surface water fertility during warm climatic conditions (Pauly *et al*. 2012b).

The Barremian black laminated mudstones, devoid of benthic fossils and trace fossils (Surlyk 1978) and with slightly increased TOC values, mark a major palaeoceanographic change from well oxygenated to likely dysoxic bottom water conditions. This, however, is not supported by the redox-sensitive trace element data (V/Al, U/Al, Cr/Al and Cu/Al ratios) that show comparable values to the Albrechts Bugt and the Rødryggen Member. Biogenic carbonate formation by calcareous nannoplankton declined in the Barremian although it is difficult to distinguish between primary signals (primary productivity) and preservation effects.

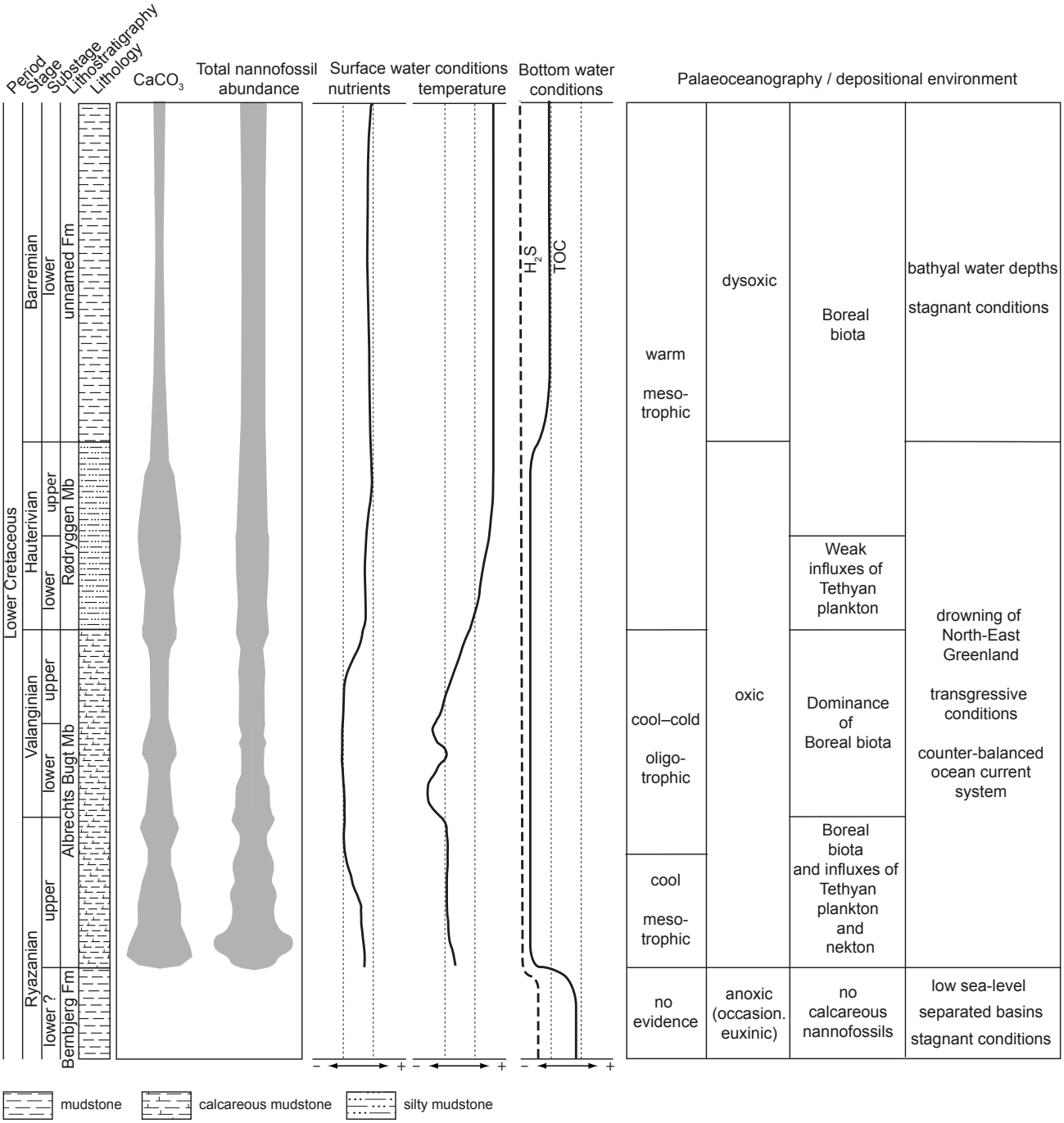

Fig. 8. Synthesis of the most important findings and their implications for palaeoceanography and depositional environments. $CaCO_3$ content and total nannofossil abundance taken from Pauly *et al.* (2012b); palaeoceanography and depositional environment from Alsen 2006 and references therein, and Pauly *et al.* (2012b).

Conclusions

The $\delta^{13}C_{org}$ curve presents the first record of this kind for the Lower Cretaceous (upper Ryazanian – Barremian) of North-East Greenland. The well-defined mid-Valanginian carbon isotope excursion has not been recorded, either due to condensation of the lower Cretaceous sediment units or a hiatus in the sedimentary record. The $\delta^{13}C_{carb}$ values exhibit strong ^{13}C depletion, indicating early diagenesis accompanied by microbial decomposition of organic matter.

The Lower Cretaceous sediments are characterized by a mixture of terrigenous detrital matter (quartz, clay minerals, heavy minerals) similar to average shale and with varying $CaCO_3$ concentrations. The Barremian black mudstones have lower calcium carbonate and higher clay mineral contents than the underlying sediments.

The deposition of the Bernbjerg Formation took place under prevailing anoxic bottom water conditions related to a low sea-level, separated basins and restricted conditions (Fig. 8). The depositional environment of the Albrechts Bugt and Rødryggen Members is characterized by well-oxygenated sea-floor conditions, hemipelagic sedimentation of fine-grained terrigenous detrital matter and biogenic carbonate settling. This relatively short period of carbonate sedimentation was followed by a decrease of carbonate accumulation and a return of likely dysoxic bottom water conditions. Bathyal water depths and a sluggish ocean circulation during the Barremian caused stagnant conditions and thereby the burial of organic matter.

During most of the Jurassic and Early Cretaceous stagnant bottom water masses resulted in the deposition of black mudstones in the Greenland–Norwegian Seaway (Mutterlose *et al*. 2003). A change to well oxygenated sea-floor conditions took place during a relatively short period with deposition of calcareous sediments. This palaeoceanographic change is also recorded in contemporaneous sediments in the north-eastern part of the Greenland–Norwegian Seaway, the Klippfisk and Lange Formations (offshore Norway) (Århus *et al*. 1990; Århus, 1991; Smelror *et al*. 1998; Mutterlose *et al*. 2003) and the Leira and Skjermyrbekken Members at Andøy (North Norway) (Dalland 1975).

Acknowledgements

GEUS (Geological Survey of Denmark and Greenland) and its members are thanked for field work management, assistance, and collaboration. We are grateful to N. Andersen (CAU Kiel) for $\delta^{13}C_{carb}$ and M. Joachimski (GeoZentrum Nordbayern) for $\delta^{13}C_{org}$ analyses. T. Goral (Ruhr-University Bochum) is thanked for carbon measurements and H. Brumsack (University of Oldenburg) for major and trace element analyses. We also thank L. Clemmensen and M. Lenniger for their helpful comments on the manuscript. Financial support by the German Research Foundation (DFG, MU 667/38-1) is gratefully acknowledged.

References

Aguirre-Urreta, M.B., Price, G.D., Ruffell, A.H., Lazo, D.G., Kalin, R.M., Ogle, N. & Rawson, P.F. 2008: Southern Hemisphere Early Cretaceous (Valanginian–Early Barremian) carbon and oxygen isotope curves from the Neuquén Basin, Argentina. Cretaceous Research 29 (1), 87–99.

Algeo, T.J. & Maynard, J.B. 2004: Trace-element behaviour and redox facies in core shales of Upper Pennsylvanian Kansas-type cyclothems. Chemical Geology 206, 289–318.

Alsen, P. 2006: The Early Cretaceous (Late Ryazanian–Early Hauterivian) ammonite fauna of North-East Greenland: taxonomy, biostratigraphy, and biogeography. Fossils and Strata 53, 229 pp.

Alsen, P. & Mutterlose, J. 2009: The Early Cretaceous of North-East Greenland: A crossroads of belemnite migration. Palaeogeography, Palaeoclimatology, Palaeoecology 280, 168–182.

Alsen, P. & Rawson, P.F. 2005: The Early Valanginian (Early Cretaceous) ammonite *Delphinites* (*Pseudogarniera*) from North-East Greenland. Bulletin of the Geological Society of Denmark 52, 201–212.

Århus, N. 1991: The transition from deposition of condensed carbonates to dark claystones in the Lower Cretaceous succession of the southwestern Barents Sea. Norsk Geologisk Tidsskrift 71, 259–263.

Århus, N., Kelly, S.R.A., Collins, J.S.H. & Sandy, M.R. 1990: Systematic palaeontology and biostratigraphy of two Early Cretaceous condensed sections from the Barents Sea. Polar Research 8, 165–194.

Bains, S., Norris, R.D., Corfield, R.M. & Faul, K.L. 2000: Termination of global warmth at the Palaeocene/Eocene boundary through productivity feedback. Nature 407, 171–174.

Berner, R.A., 1981: A new geochemical classification of sedimentary environments. Journal of Sedimentary Petrology 51, 359–365.

Brumsack, H.-J. 2006: The trace metal content of recent organic carbon-rich sediments: Implication for Cretaceous black shale formation. Palaeogeography, Palaeoclimatology, Palaeoecology 232 (2-4), 344–361.

Brumsack, H.-J. & Gieskes, J.M. 1983: Interstitial water trace-metal chemistry of laminated sediments from the Gulf of California, Mexico. Marine Chemistry 14, 89–106.

Channell, J.E.T., Erba, E. & Lini, A. 1993: Magnetostratigraphic

calibration of the late Valanginian carbon isotope event in pelagic limestones from northern Italy and Switzerland. Earth and Planetary Science Letters 118, 145–166.

Dalland, A. 1975: The Mesozoic rocks of Andøy, Northern Norway. Norges Geologiske Undersøgelse Bulletin 316, 271–287.

Decampo, D.M. 2010: The Geochemistry of Continental Carbonates. In: Alonso-Zarza, A.M. & Tanner, L.H. (eds), Carbonates in Continental Settings, Geochemistry, Diagenesis and Applications. Developments in Sedimentology 62, 1–59. Amsterdam: Elsevier.

Ferreri, V., Weissert, H., D'Argenio, B. & Buonocunto, F.P. 1997: Carbon isotope stratigraphy: a tool for basin to carbonate platform correlation. Terra Nova 9, 57–61.

Gingele, F.X., Zabel, M., Kasten, S., Bonn, W.J. & Nurnberg, C.C. 1999: Biogenic barium as a proxy for paleoproductivity: Methods and limitations of application. In: Fischer, G. & Wefer, G. (eds), Use of Proxies in Paleoceanography, 345–364. Berlin: Springer-Verlag.

Gröcke, D.R., Hesselbo, S.P. & Jenkyns, H.C. 1999: Carbon isotope composition of Lower Cretaceous fossil wood; ocean–atmosphere chemistry and relation to sea-level change. Geology 27, 155–158.

Gröcke, D.R., Price, G.D., Baraboshkin, E., Mutterlose, J. & Ruffell, A.H. 2003: The Valanginian terrestrial carbon isotope record. Geophysical Research Abstracts 5.

Gröcke, D.R., Price, G.D., Robinson, S.A., Baraboshkin, E.Y., Mutterlose, J. & Ruffell, A.H. 2005: The Upper Valanginian (Early Cretaceous) positive carbon isotope event recorded in terrestrial plants. Earth and Planetary Science Letters 240, 495–509.

Harper, D.A.T., Alsen, P., Owen, E.F. & Sandy, M.R. 2005: Early Cretaceous brachiopods from East Greenland: biofacies and biogeography. Bulletin of the Geological Society of Denmark 52, 213–225.

Huerta-Diaz, M.G. & Morse, J.W. 1992: Pyritization of trace metals in anoxic marine sediments. Geochimica et Cosmochimica Acta 56, 2681–2702.

Jenkyns, H.C. 2010: Geochemistry of oceanic anoxic events. Geochemistry, Geophysics, Geosystems 11 (3), Q03004, doi: 10.1029/2009GC002788.

Kujau, A., Heimhofer, U., Hochuli, P., Pauly, S., Morales, C., Adatte, T., Föllmi, K.B., Ploch, I. & Mutterlose, J. 2013: Reconstructing Valanginian (Early Cretaceous) mid-latitude vegetation and climate dynamics based on spore-pollen assemblages. Review of Palaeobotony and Palynology 197, 50–69.

Lein, A.Y. 2004: Authigenic carbonate formation in the ocean. Lithology and Mineral Resources 39, 1–30.

Lini, A., Weissert, H. & Erba, E. 1992: The Valanginian carbon isotope event: a first episode of greenhouse climate conditions during the Cretaceous. Terra Nova 4, 374–384.

Lyons, T.W., Anbar, A.D., Severmann, S., Scott, C. & Gill, B. 2009: Tracking euxinia in the ancient ocean: a multiproxy perspective and Proterozoic case study. Annual Review of Earth and Planetary Sciences 37, 507–34.

Maync, W. 1949: The Cretaceous beds between Kuhn Island and Cape Franklin (Gauss Peninsula), Northern East Greenland. Meddelelser om Grønland 133 (3), 291 pp.

McArthur, J.M., Janssen, N.M.M., Reboulet, S., Leng, M.J., Thirlwall, M.F. & van de Schootbrugge, B. 2007: Palaeotemperatures, polar ice-volume, and isotope stratigraphy (Mg/Ca, $\delta^{18}O$, $\delta^{13}C$, $^{87}Sr/^{86}Sr$): The Early Cretaceous (Berriasian, Valanginian, Hauterivian). Palaeogeography, Palaeoclimatology, Palaeoecology 248, 391–430.

McManus, J. *et al.* 1998: Geochemistry of barium in marine sediments: Implications for its use as a paleoproxy. Geochimica et Cosmochimica Acta 62, 3453–3473.

Menegatti, A.P., Weissert, H., Brown, R.S., Tyson, R.V., Farrimond, P., Strasser, A. & Caron, M. 1998: High-resolution $\delta^{13}C$-stratigraphy through the early Aptian "Livello Selli" of the Alpine Tethys. Paleoceanography 13, 530–545.

Morse, J.W. & Luther III, G.W. 1999: Chemical influences on trace metal-sulphide interactions in anoxic sediments. Geochimica et Cosmochimica Acta 63, 3373–3378.

Mutterlose, J. *et al* 2003: The Greenland–Norwegian Seaway: A key area for understanding Late Jurassic to Early Cretaceous paleoenvironments. Paleoceanography 18 (1), 1–26.

Nøhr-Hansen, H. 1993: Dinoflagellate cyst stratigraphy of the Barremian to Albian, Lower Cretaceous, North-East Greenland. Bulletin Grønlands Geologiske Undersøgelse 166, 171 pp.

Nunn, E.V., Price, G.D., Gröcke, D.R., Baraboshkin, E.Y., Leng, M.J. & Hart, M.B. 2010: The Valanginian positive carbon isotope event in Arctic Russia: evidence from terrestrial and marine isotope records and implications for global carbon cycling. Cretaceous Research 31 (6), 577–592.

Pauly, S., Mutterlose, J. & Alsen, P. 2012a: Lower Cretaceous (upper Ryazanian–Hauterivian) chronostratigraphy of high latitudes (North-East Greenland). Cretaceous Research 34, 308–326.

Pauly, S., Mutterlose, J. & Alsen, P. 2012b: Early Cretaceous palaeoceanography of the Greenland–Norwegian Seaway evidenced by calcareous nannofossils. Marine Micropaleontology 90–91, 72–85.

Prakash Babu, C., Brumsack, H.-J., Schnetger, B. & Böttcher, M.E. 2002: Barium as a productivity proxy in continental margin sediments: a study from the eastern Arabian Sea. Marine Geology 184, 189–206.

Smelror, M., Mørk, A., Monteil, E., Rutledge, D. & Leereveld, H. 1998: The Klippfisk Formation – a new lithostratigraphic unit of Lower Cretaceous platform carbonates on the Western Barents Shelf. Polar Research 17 (2), 181–202.

Strogen, D.P., Burwood, R. & Whitham, A.G. 2005: Sedimentology and geochemistry of Late Jurassic organic-rich shelfal mudstones from East Greenland: regional and stratigraphic variations in source-rock quality. In: Doré, A.G. & Vining, B.A. (eds): Petroleum Geology: North-West Europe and Global Perspectives. Proceedings of the 6th Petroleum Geology Conference, 903–912. London: The Geological Society.

Surlyk, F. 1977: Stratigraphy, tectonics and palaeogeography of the Jurassic sediments of the areas north of Kong Oscars Fjord, East Greenland. Bulletin Grønlands Geologiske Undersøgelse 123, 56 pp.

Surlyk, F. 1978: Submarine fan sedimentation along fault scarps on tilted fault blocks (Jurassic–Cretaceous boundary, East Greenland). Bulletin Grønlands Geologiske Undersøgelse 128, 108 pp.

Surlyk, F. 1984: Fan-delta to submarine fan conglomerates of the Volgian–Valanginian Wollaston Forland Group, East Greenland. In: Koster, E.H. & Steel, R.J. (eds), Sedimentology of gravels and conglomerates. Canadian Society of Petroleum Geologists, Memoir 10, 359–382.

Surlyk, F. 1990: A Jurassic sea-level curve for East Greenland. Palaeogeography, Palaeoclimatology, Palaeoecology 78, 71–85.

Surlyk, F. 2003: The Jurassic of East Greenland: a sedimentary record of thermal subsidence, onset and culmination of rifting. Geological Survey of Denmark and Greenland Bulletin 1, 659–722.

Surlyk, F. & Clemmensen, L.B. 1975a: A Valanginian turbidite sequence and its palaegeographical setting (Kuhn Ø, East Greenland). Geological Society of Denmark Bulletin 24, 61–73.

Surlyk, F. & Clemmensen, L.B. 1975b: Sedimentology and stratigraphy of the Middle Jurassic–Lower Cretaceous rocks of the Wollaston Forland–Kuhn Ø area, central East Greenland. Rapport Grønlands Geologiske Undersøgelse 75, 110–115.

Surlyk, F. & Clemmensen, L.B. 1983: Rift progradation and eustacy as controlling factors during Jurassic inshore and shelf sedimentation in northern East Greenland. Sedimentary Geology 34, 119–143.

Surlyk, F., Callomon, J.H., Bromley, R.G. & Birkelund, T. 1973: Stratigraphy of the Jurassic–Lower Cretaceous sediments of Jameson Land and Scoresby Land, East Greenland. Bulletin Grønlands Geologiske Undersøgelse 105, 76 pp.

Swientek, O. 2003: The Greenland–Norwegian Seaway: climatic and cyclic evolution of Late Jurassic–Early Cretaceous sediments. Inaugural Dissertation, PhD thesis, University of Cologne, Germany, 148 pp.

Tribovillard, N., Riboulleau, A., Lyons, T. & Baudin, F. 2004: Enhanced trapping of molybdenum by sulfurized marine organic matter of marine origin in Mesozoic limestones and shales. Chemical Geology 213, 385–401.

Tribovillard, N., Ramdani, A. & Trentesaux, A. 2005: Controls on organic accumulation in Late Jurassic shales of northwestern Europe as inferred from trace-metal geochemistry. In: Harris, N. (ed.), The Deposition of Organic-Carbon-Rich Sediments: Models, Mechanisms, and Consequences. SEPM Special Publication 82, 145–164.

Tribovillard, N., Algeo, T.J., Lyons, T. & Riboulleau, A. 2006: Trace metals as paleoredox and paleoproductivity proxies: an update. Chemical Geology 232, 12–32.

Wedepohl, K.H. 1971: Environmental influences on the chemical composition of shales and clays. In: Ahrens, L. H., Press, F., Runcorn, S. K. & Urey, H. C. (eds), Physics and Chemistry of the Earth, 305–333. Oxford: Pergamon.

Wedepohl, K.H. 1991: The composition of the upper earth's crust and the natural cycles of selected metals. Metals in natural raw materials. Natural resources. In: Merian, E. (ed.), Metals and their compounds in the environment, 3–17. Weinheim: VCH-Verlagsgesellschaft.

Weissert, H. 1989: C-isotope stratigraphy, a monitor of paleoenvironmental change: a case study from the early Cretaceous. Surveys in Geophysics 10, 1–61.

Weissert, H. & Channell, J.E.T. 1989: Tethyan carbonate carbon isotope stratigraphy across the Jurassic–Cretaceous boundary: an indicator of decelerated carbon cycling. Paleoceanography 4, 483–494.

Weissert, H. & Erba, E. 2004: Volcanism, CO_2 and palaeoclimate: a Late Jurassic–Early Cretaceous carbon and oxygen isotope record. Journal of the Geological Society, London 161, 695–702.

Wortmann, U.G. & Weissert, H. 2000: Tying platform drowning to perturbations of the global carbon cycle with a $\delta^{13}C_{org}$-curve from the Valanginian of DSDP Site 416. Terra Nova 12, 289–294.

Taxonomic Index

Associated skeletal and dental remains of a fossil odontaspidid shark (Elasmobranchii: Lamniformes) from the Middle Eocene Lillebælt Clay Formation in Denmark

BITTEN BOLVIG HANSEN, GILLES CUNY, BO WILHELM RASMUSSEN, KENSHU SHIMADA, PERRI JACOBS & CLAUS HEILMANN-CLAUSEN

Hansen, B.B., Cuny, G., Rasmussen, B.W., Shimada, K., Jacobs, P. & Heilmann-Clausen, C., 2013. Associated skeletal and dental remains of a fossil odontaspidid shark (Elasmobranchii: Lamniformes) from the Middle Eocene Lillebælt Clay Formation in Denmark. ©2013 by Bulletin of the Geological Society of Denmark, Vol. 61, pp. 37–46. ISSN 2245-7070. (www.2dgf.dk/publikationer/bulletin).

A set of associated vertebrae and teeth of a fossil shark was collected from the lower Lutetian (Middle Eocene) part of the Lillebælt Clay Formation in Denmark. Its vertebral morphology indicates that the individual belongs to an odontaspidid lamniform shark. Although it is here identified as Odontaspididae indet., its tooth morphology suggests that the fossil shark possibly belongs to an undescribed taxon closely allied to *Odontaspis* or *Palaeohypotodus*. Based on comparisons with extant *Odontaspis*, the fossil individual possibly measured about 333 cm in total length. The disarticulated nature of the specimen in a low-energy deposit indicates that the shark carcass must have been lying on the sea floor for some time before its burial. The fossil individual was found along with a possible shed tooth of another indeterminate odontaspidid taxon.

Keywords: Denmark, Eocene, Lamniformes, shark, teeth, vertebrae.

Received 26 February 2013
Accepted in revised form
21 August 2013
Published online
20 September 2013

Bitten Bolvig Hansen [bottenhansen@hotmail.com], Gilles Cuny [gilles@snm.ku.dk], Bo Wilhelm Rasmussen [bwrasmussen@snm.ku.dk], Natural History Museum of Denmark, University of Copenhagen, Øster Voldgade 5–7, DK-1350 Copenhagen K, Denmark. Kenshu Shimada [kshimada@depaul.edu], Department of Environmental Science and Studies and Department of Biological Sciences, DePaul University, 2325 N. Clifton Avenue, Chicago, Illinois 60614, USA, and Sternberg Museum of Natural History, 3000 Sternberg Drive, Hays, Kansas 67601, USA. Perri Jacobs [perrijacobs@gmail.com], Department of Biological Sciences, DePaul University, 2325 N. Clifton Avenue, Chicago, Illinois 60614, USA. Claus Heilmann-Clausen [claus.heilmann@geo.au.dk], Department of Geoscience, Aarhus University, DK-8000 Aarhus C, Denmark.

In 2007, a set of fossil shark vertebrae and teeth was collected at a Danish Middle Eocene locality on the southeast coast of Trelde Næs, north of Fredericia (GPS coordinates: N 55°36'05.2", E 09°48'38.6"; Fig. 1). The site is situated immediately south-west of the Vesterskov Section described by Schnetler & Heilmann-Clausen (2011). The fossil assemblage was collected by three paleontology enthusiasts. Dennis Løndal Rasmussen found the first seven vertebrae and, together with Mogens Madsen, he discovered two more vertebrae in the same area two days later. One week later, he went back to the site with Søren Nielsen-Englyst to open an excavation where the rest of the vertebrae were retrieved. In addition, 20 kg of sediments were taken during the excavation and were screen-washed at the Natural History Museum of Denmark in Copenhagen by Sten Lennart Jakobsen. This yielded additional materials, including one vertebra and six tooth remains.

All the components of the fossil assemblage were found within a volume of approximately 1.5 × 1.5 m × 2 m. They are all but one tooth interpreted to come from a single individual shark because of identical morphological characteristics and preservation among the vertebrae and teeth found within the small area at a single stratigraphic horizon. The fossil assemblage is now housed in the Natural History Museum of Denmark under the catalogue number DK541 after it was declared 'Danekræ' (Christensen & Hald 1991) in 2008. Associated remains of sharks are rare in the fossil record due to the cartilaginous nature of their skeleton. The fossil assemblage that largely constitutes a single shark individual is thus significant. The aim of this paper is to describe the fossil shark and to discuss its palaeobiological significance along with another shark that co-occurred as an isolated tooth. The anatomical terminology used here largely follows Ridewood (1921) and Cappetta (1987).

Geological context

The 6 km long south-east coast of the Trelde Næs peninsula is dominated by outcrops of mainly grey-green, hemipelagic clays of the Lillebælt Clay Formation (Heilmann-Clausen *et al.* 1985). This formation spans the Lower to Middle Eocene (upper Ypresian – lower Lutetian) and its thickness at Trelde Næs is estimated to be about 70 m (Schnetler & Heilmann-Clausen 2011). The Lillebælt Clay Formation is underlain by the Ypresian Røsnæs Clay Formation and overlain by the Lutetian-Priabonian Søvind Marl Formation (Heilmann-Clausen *et al.* 1985). The Lillebælt Clay Formation holds a taxonomically diverse fauna with both epifaunal and infaunal benthos and nektonic organisms, but its shark components remain largely undescribed (Heilmann-Clausen 2012). The Lillebælt Clay Formation is composed of extremely fine-grained, smectite-rich clays informally named as 'plastic clay' and is known for forming large landslides along the coast. Its molluscan fauna indicates a water depth about 100–300 m (Schnetler & Heilmann-Clausen 2011), whereas a water depth of *c.* 500 m was assumed by Heilmann-Clausen (2012). The Lillebælt Clay Formation is subdivided into six formal beds named, in ascending order, L1 to L6 (Heilmann-Clausen *et al.* 1985). A dinoflagellate preparation (chc lab. no. 3164) was made of sideritic material associated with the fossil shark assemblage. The preparation yielded abundant, well-preserved dinoflagellate cysts. The assemblage is typical for the *Wetzeliella articulata-ovalis* Zone of Heilmann-Clausen (1988). The presence of *W. articulata* subspecies *brevicornuta* suggests that the shark-bearing horizon belongs to the lower to middle part of this zone. The zonal assignment indicates a possible provenance of the material from the upper part of Bed L4 to the lower part of Bed L6, but most likely not higher than the upper part of Bed L5. The site was visited by one of us (CHC) with Mogens Madsen in 2013. The site is located immediately south-west of a high cliff with Bed L4 referred to as the Vesterskov Section by Schnetler & Heilmann-Clausen (2011). South-west of the site occurs a high cliff with Quaternary sand and clay. Today, the layer in which the shark remains were found is covered by scree consisting of clay from Bed L5, which is seen in situ above the sliding masses. The conditions at the shark-bearing site in combination with the biostratigraphic data indicate that the shark material most likely originated from the lower Lutetian Bed L5.

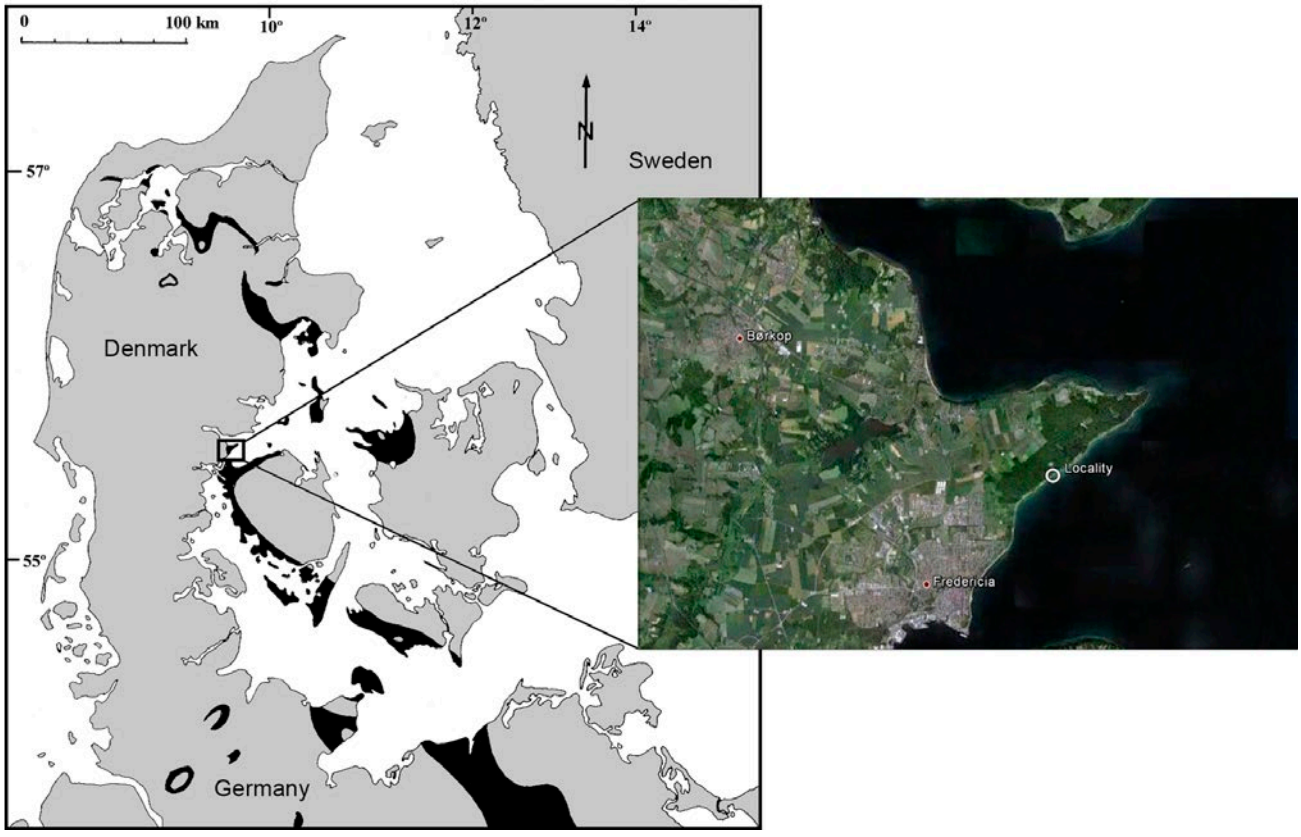

Fig. 1. Sub-Quaternary map showing, in black, the distribution of Eocene deposits in Denmark (modified from Schwarzhans 2007). The satellite image shows the excavation site at Vesterskov on Trelde Næs (modified from Google Earth (image © 2012 Aerodata International Surveys, © Google, © GeoBasis-DE/BKG, Image © 2012 GeoEye)).

Material and methods

The entire assemblage of fossil remains in DK541 comprises a total of eight teeth (five nearly complete teeth and three isolated tooth cusps) and 86 vertebrae, some of which are fragmentary (Fig. 2). Most of the vertebrae and teeth were mechanically prepared using sandblasting and scraping tools. A solution of 1 part thioglycolic acid to 19 parts water was used, as recommended by Howie (1974), to free one of the teeth (DK541d) that was embedded in a vertebra-bearing block of sideritic matrix. However, the enameloid of the tooth was severely damaged, likely due to the lack of any buffer added to the solution, and the tooth was subsequently prepared mechanically (Fig. 2B). It was therefore not attempted to free another tooth, DK541e, from its sideritic matrix (Fig. 2C).

One of the teeth in DK541, designated as DK541c, is embedded in the matrix of one of the vertebrae and exhibits only its labial side (Fig. 3). DK541c is darker in preserved colour, smaller in size, and more delicately built compared to all other teeth in DK541. Therefore, it is interpreted that DK541c does not belong to the same shark individual as represented by the rest of the specimen. For the purpose of this paper, unless otherwise explicitly indicated as DK541c, the description of DK541 and subsequent discussions specifically refer to the shark individual represented by the associated dental and skeletal remains excluding DK541c.

In order to extract additional morphological information from fragile vertebrae, computed tomography (CT) scanning was applied to eight vertebral centra using a Siemens MDCT scanner (four channels) at the Forensic Department of Rigshospitalet in Copenhagen, Denmark. The parameters for the scanning were 120 kV and 220 mA, and the algorithm Kernel 70 was used to emphasize the denser structure of the objects. The scanning was performed with a matrix of (X,Y) 0.5 mm × 0.5 mm and a reconstruction (Z) of 0.5 mm. Thus, the object is shown with isometric voxels, and proportions are kept as original. However, resolution of the scanner did not exceed 0.5 mm, and structures smaller than this size were not reconstructed. Digital cross-sections of vertebral centra were generated using

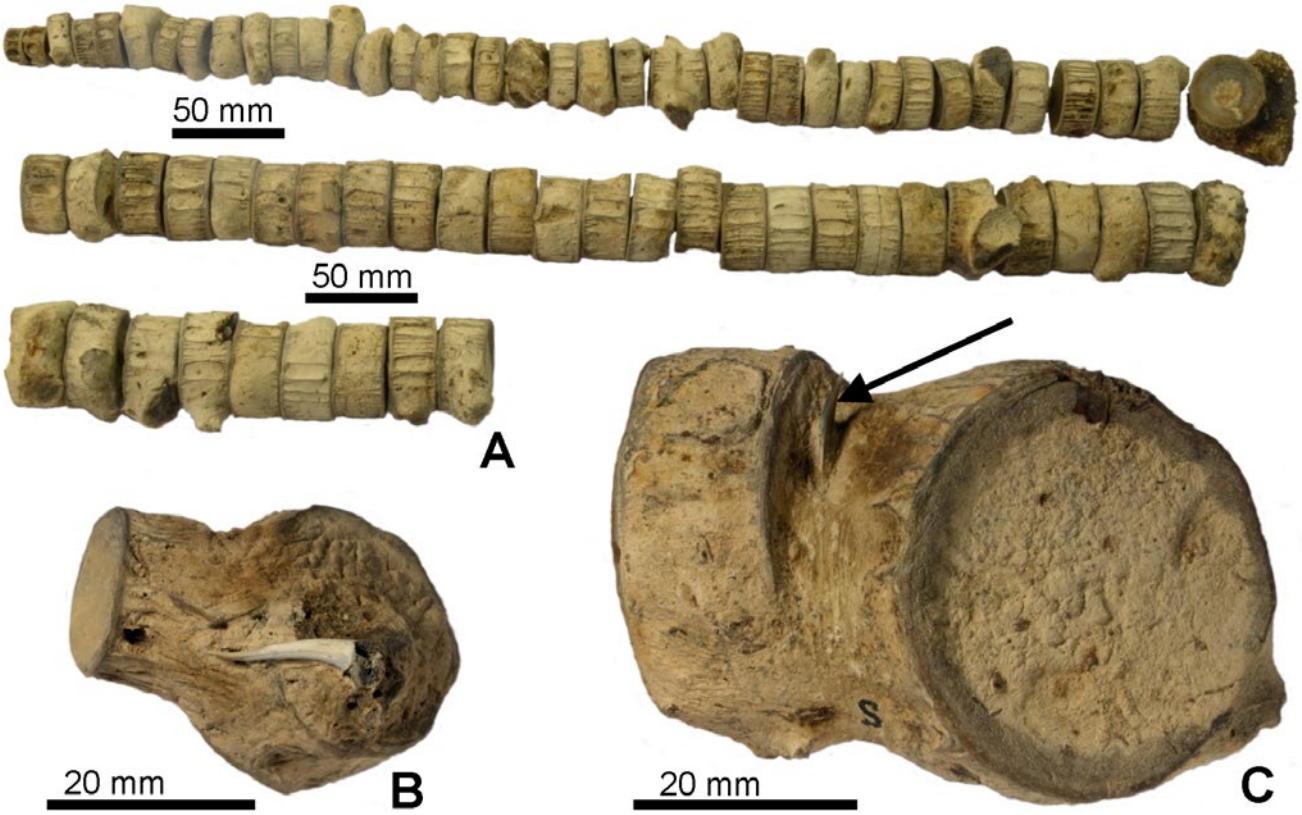

Fig. 2. Vertebral and dental remains of odontaspidid shark DK 541 from the middle Eocene Lillebælt Clay Formation of Denmark. **A**: General view of 73 vertebrae out of a total of 86. The sequence of vertebrae is artificially organized in this illustration. The rest of the vertebrae are either too fragmentary or not fully prepared (see B and C) to be included in this tentative reconstruction of the vertebral column of DK 541. **B**: Nodule DK541d containing two vertebral centra and a tooth. **C**: Nodule DK541e containing two vertebral centra and a tooth (at arrow) still embedded in the matrix between the two centra.

'AmbiVU 3D Workstation' (a free download program by AmbiVU) in which transverse sections were made through the centre of the double-cones. In addition, one of the scanned vertebrae was also cut in half in the same plane as the digital cross sections. We note that, because the teeth and the matrix have a similar density, the MDCT scanner did not allow recovery of images of the teeth still partly embedded in matrix.

Description

Vertebrae

The 86 vertebral centra are all disarticulated and are represented by various sizes (Fig. 2 and Fig. 4G–J). The largest centra measure 41 mm in lateral width, 36 mm in dorsoventral height, and 20 mm in anteroposterior thickness, whereas the smallest ones measure 18, 17, and 9 mm, respectively. The vertebrae collectively exhibit the following trend: the smaller the centrum, the more rounded it appears in anterior or posterior view. The largest ones are slightly compressed dorsoventrally, which is not the result of post-mortem compression through fossilization.

All vertebrae are amphicoelous, consisting of two evenly concave calcified cones. The rims of each centrum are relatively thick, and each concave articular face shows annuli. The two calcified cones are supported by radiating calcified lamellae that vary in number and size around the circumference of each centrum with a tendency to be arranged in pairs. In some centra, the lamellae bifurcate at their anterior and posterior extremities. On the dorsal and ventral faces, there is a pair of ovoid pits representing the basidorsal and basiventral insertion points for the neural and haemal arches, respectively. The anterior and posterior extremities of the paired pits reach to the inner surface of each vertebral cone. The dorsal pits are set closer to each other than the ventral pits.

One vertebra (DK541f) that was sectioned in a plane approximately halfway between the anterior and posterior ends reveals an asterospondylic condition (Fig. 5A). Four main uncalcified wedges are recognized, forming the basidorsal and basiventral cartilages. They radiate from the calcified primary double cone derived from the notochordal sheath. Inside the sheath, there is an uncalcified inner-zone cartilage. Between the four arch-bases, the intermedialia is invaded by calcified lamellae, which are often bifurcating towards the outside of the centrum, explaining their paired arrangement observed on the external surface. The bifurcations occur at various levels between the sheath cartilage and the external part of the centrum. This pattern is referred to as radial asterospondylic (see White 1937). All the vertebrae

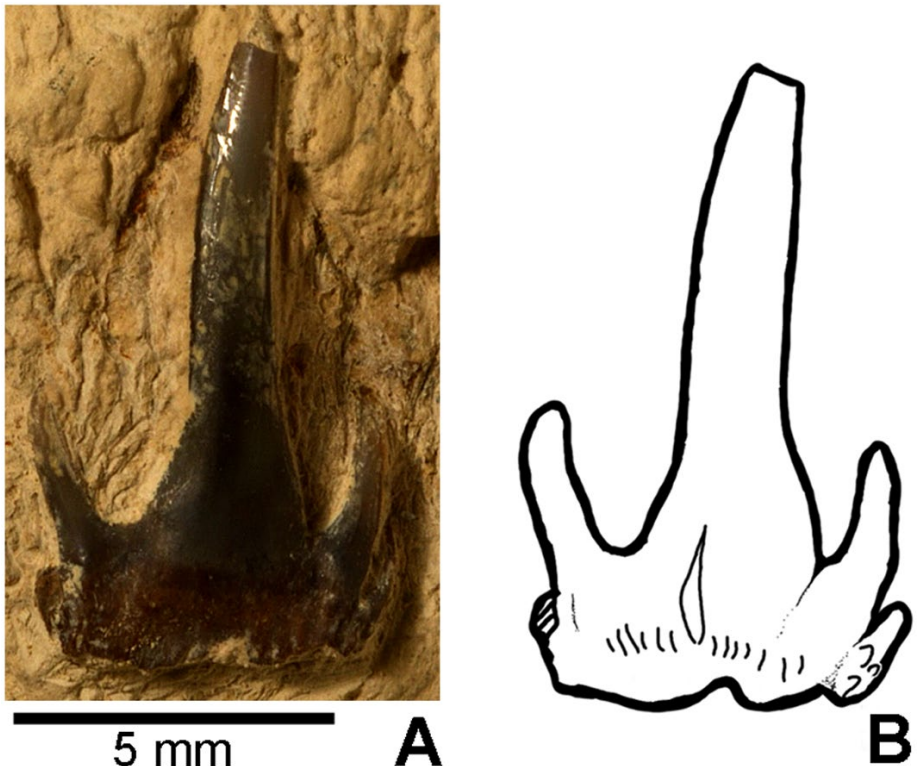

Fig. 3. Photograph (**A**) and interpretative sketch (**B**) of isolated odontaspidid tooth DK541c, labial view, that co-occurred with dental and vertebral remains of another odontaspidid individual DK541 (excluding DK541c); see Figs 2 and 4.

that were CT-scanned showed the same radial asterospondylic pattern (for rotating CT-reconstructions of DK541h, see also supplementary data files 1 and 2 on http://2dgf.dk/publikationer/bulletin/191bull61.html).

Teeth (excluding DK541c)

Each tooth, if complete, consists of a crown with a large main cusp and two pairs of lateral cusplets and a bilobed root. The crown heights of the four nearly complete teeth (DK541a,b,d,e; Fig. 4A–F) range from 10 to 24 mm, whereas the three isolated cusps have heights that range from 2.5 to 6 mm. The main cusp is tall and slender, flanked by up to two pairs of lateral cusplets. The main cusp is straight and narrow in labial view, slightly sigmoid in mesial or distal view, and slightly bulbous at its base in labial or lingual view. Both lingual and labial faces of the main cusp are convex, but the former is more convex than the latter. The mesial and distal cutting edges are sharp and reach to the crown base. The cutting edges are mostly smooth, but may bear weak serrations at the base of the main cusp. The first pair of lateral cusplets is well-developed, and they can reach up to one-third of the height of the main cusp. In contrast, the second pair is much smaller. One of the lateral cusplets in DK541a is pathologically curved lingually almost at right angle with its base (Fig. 4A–C; e.g., Becker *et al*. 2000; Balbino & Antunes 2007), and the same distinctive curvature is also seen in one of the isolated cusplets. In all teeth, the enameloid of the crown is smooth except for faint, short wrinkles or folds at the base of the labial face. At the base of the labial face of the main cusp sits a median, faint node. Each root, where preserved, shows broadly splayed lobes with narrow basal tip. The lobes are not very long and slightly curved labially. The surface texture of the root is porous except for a smooth dental band forming the tooth neck immediately below the crown on the lingual face. The lingual protuberance bears a shallow, but prominent nutritive groove with sharp edges.

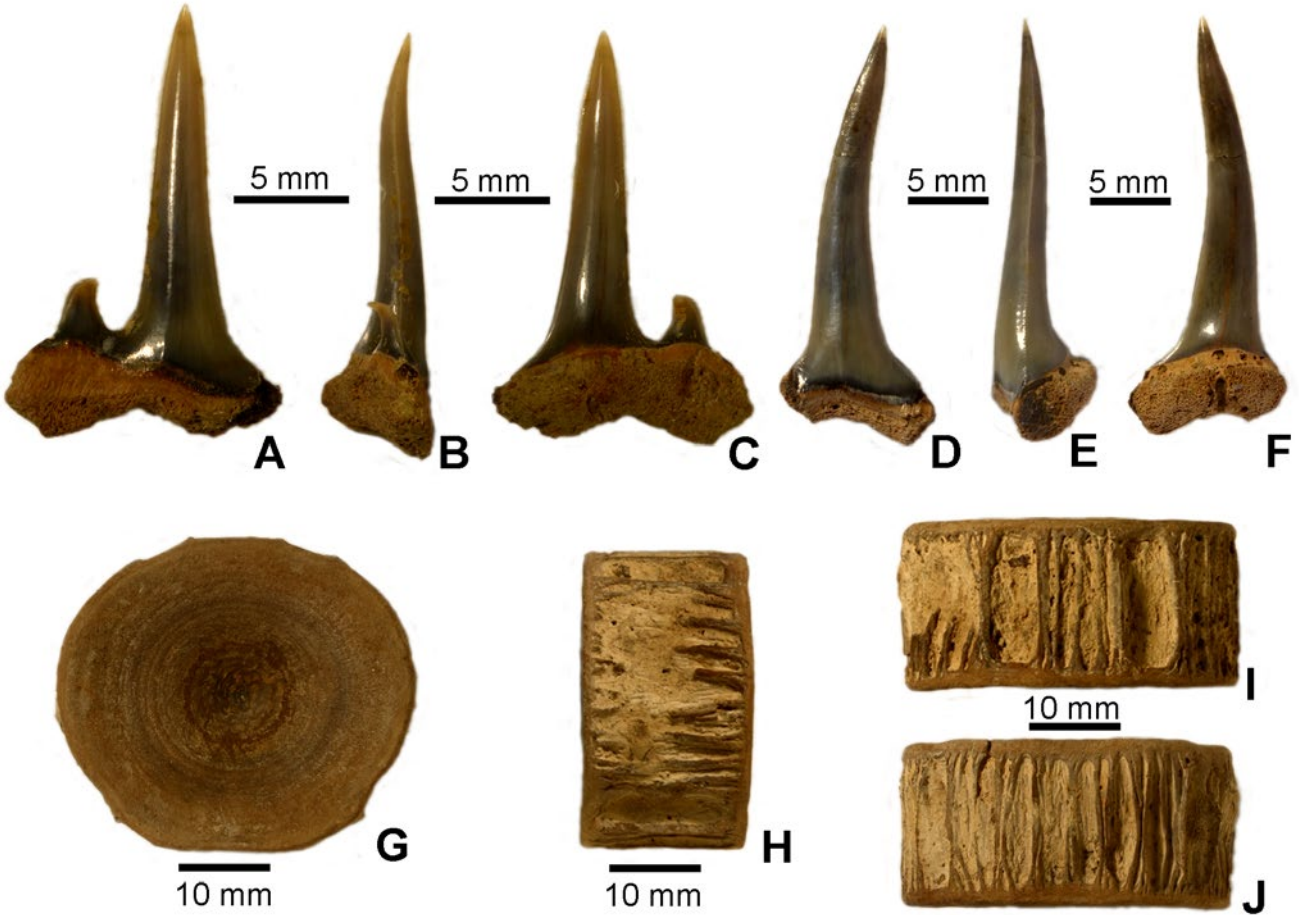

Fig. 4. Selected examples of associated dental and vertebral remains of odontaspidid shark DK541 (excluding DK541c). **A–C**: tooth DK541a in labial (**A**), distal (**B**), and lingual (**C**) views; **D–F**: tooth DK541b in labial (**D**), distal (**E**), and lingual (**F**) views; **G–J**: vertebral centrum DK541g in articular (**G**), lateral (**H**), dorsal (**I**), and ventral (**J**) views.

Discussion

Taxonomic remarks

All vertebrae in DK541 share the same external characteristics, and all the eight specimens that were CT-scanned show the same radial, asterospondylic structure. Asterospondylic vertebrae are restricted to the superorder Galeomorphi, and the radial asterospondylic pattern is found only in two orders, Orectolobiformes and Lamniformes (White 1937; Cappetta 1987). Orectolobiform centra depicted by Ridewood (1921) appear structurally simpler than those of Lamniformes; they have eight calcified lamellae (ten in *Stegostoma* and *Chiloscyllium*: White 1937) that are straight or branched only once or twice, and the lamellae are slightly thicker compared to those in lamniform centra. In external view, orectolobiform vertebrae show a more regular spacing of the calcified lamellae than in lamniform vertebrae (Kozuch & Fitzgerald 1989) as well as in DK541. Therefore, the vertebral morphology clearly indicates that DK541 belongs to a lamniform shark.

Based on published literature, the vertebrae of DK541 are quite similar to the vertebrae of extant *Carcharias taurus* by exhibiting a rather thick rim and ovoid ventral and dorsal pits, the extremities of which reach the rims (see Kozuch & Fitzgerald 1989; Purdy *et al.* 2001). However, we note that the centra of DK541 (Fig. 4G–J) also closely resemble those of extant *Odontaspis ferox* (Fig. 5C–F) not only externally, but also internally (Fig. 5A–B). Centra of other extant lamniform sharks, such as *Isurus*, possess very thin rims, and those of *Carcharodon* possess shorter ventral and dorsal pits, the extremities of which do not reach the rims (Kozuch& Fitzgerald 1989). This latter character seems, however, quite variable as the extremities of the dorsal and ventral pits do reach the rims in the vertebrae of *Carcharodon hubbelli* from the Pliocene of Peru (Ehret *et al.* 2009, 2012). The vertebrae of *Otodus obliquus* from the Eocene London Clay figured by Casier (1966) are twice the size of DK541, and the extremities of the dorsal and ventral pits do not reach the rims. It should also be noted that the vertebrae of DK541 do not belong to any of the Cretaceous lamniforms with known vertebral morphologies, such as Cretoxyrhinidae and Cardabiodontidae, because these taxa have more numerous lamellae in the lateral intermedialia, and the entire centra are anteroposteriorly compressed (e.g., Siverson 1999; Blanco-Piñón *et al.* 2005; Shimada *et al.* 2006).

DK541 is also interpreted to be a lamniform shark on the basis of its teeth with well-developed root lobes, tall slender main cusp, and sharp lateral cusplets.

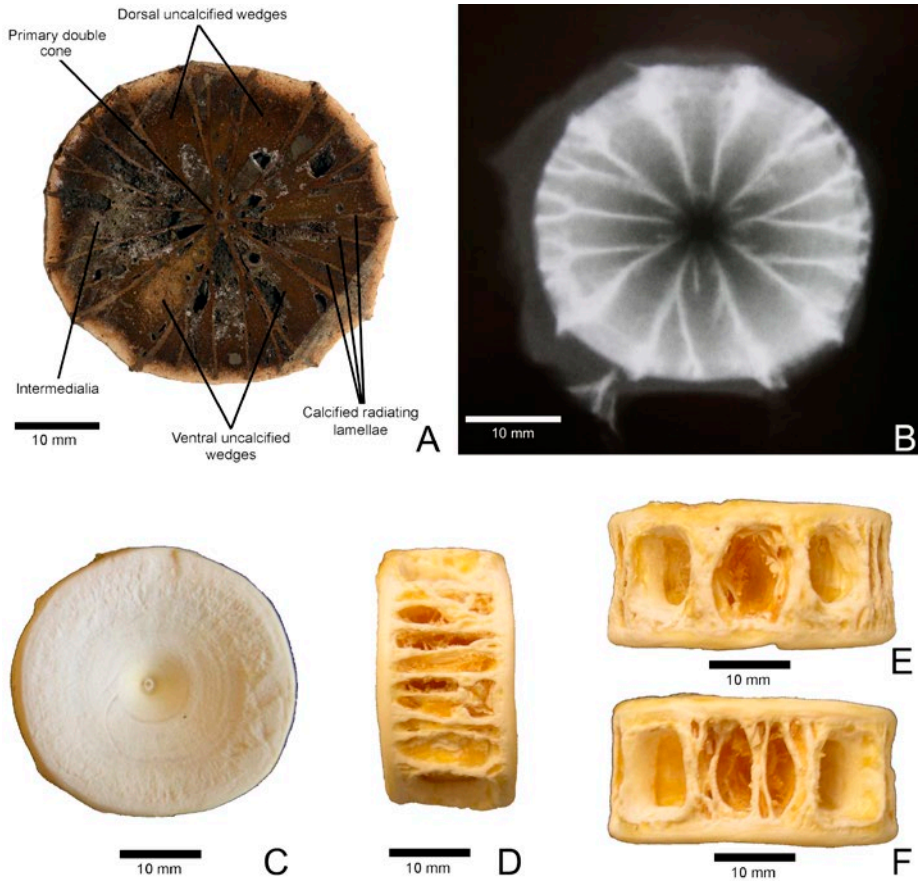

Fig. 5. **A**: Sectioned fossil vertebral centrum DK541f. **B-F**: internal and external morphology of the sixth vertebra removed from 297-cm-total length extant *Odontaspis ferox* (BPBM 9335); **B**: x-ray image; **C**: articular view; **D**: lateral view; **E**: dorsal view; **F**: ventral view.

The root lobes are well separated and the lingual protuberance bears a distinct nutritive groove. Such characteristics can be found in the teeth of the family Mitsukurinidae and Odontaspididae *sensu lato* (i.e., a paraphyletic assemblage including Odontaspididae and Carchariidae: Heinicke *et al*. 2009; Vélez-Zuazo & Agnarsson 2011). However, teeth of mitsukurinids tend to exhibit a more prominent lingual ornamentation and more reduced lateral cusplets than those of odontaspidids and DK541 (see Cappetta 2012). When compared to other Eocene odontaspidids, the teeth of DK541 can be distinguished easily from those of *Araloselachus, Borealotodus, Carcharias, Glueckmanotodus, Hypotodus, Jaekelotodus, Mennerotodus, Sylvestrilamia*, and *Turania*, in which the teeth do not possess lateral cusplets as tall as in DK541 (see Cappetta 2012). Well-developed lateral cusplets occur in *Brachycarcharias, Odontaspis, Orpodon*, and *Palaeohypotodus* (Cappetta 2012). Teeth of *Brachycarcharias*, however, possess a broader main cusp and cusplets than those of DK541, and the lingual face of their main cusp is ornamented (Cappetta & Nolf 2005). Teeth of *Orpodon* are much smaller (<12 mm in height) and possess broader lateral cusplets than those of DK541 (see Cappetta & Nolf 2005; Cappetta 2012).

DK541a and DK541b (Fig. 4A–F) possess cutting edges that reach the base of the main cusp that is quite compressed labiolingually, characteristics not consistent with *Odontaspis winkleri* and the genus *Odontaspis* in general (see Cappetta & Nolf 2005; Mannering & Hiller 2008; Cappetta 2012). The weak serrations at the base of their cutting edges are more reminiscent to those observed in *Palaeohypotodus* (Cappetta 2012), but this genus is unknown after the Ypresian (Ward & Wiest 1990; Cvancara & Hoganson 1993). Another odontaspidid species, *O. speyeri*, possesses vertical folds and tubercles at the labial crown base in juvenile specimens, possibly indicating its close phylogenetic affinity to *Paleohypotodus* (Siverson 1995). Teeth of *O. speyeri,* however, have relatively short lateral cusplets and less slender crowns compared to the teeth of DK541 (see Arambourg & Signeux 1952). Moreover, *O. speyeri* has only been found in early Paleocene deposits, whereas DK541 comes from the lower Lutetian (Arambourg & Signeux 1952).

In summary, although the resemblance between *Carcharias* vertebrae and the vertebrae of DK541 does exist, vertebrae of DK541 are also morphologically quite similar to those of *Odontaspis ferox*. The tooth morphology seen in DK541 suggests that the shark individual belongs to an odontaspidid close to *Odontaspis* or *Palaeohypotodus*. Because the tooth morphology observed in DK541 is quite unique, it may belong to an undescribed odontaspidid species. However, the tooth set in the specimen is small, making it difficult to adequately decipher the total morphological range of teeth. Therefore, we here conservatively identify DK541 as Odontaspididae indet. that was closely allied to *Odontaspis* or *Palaeohypotodus*.

Body size estimation

The biology of the fossil shark individual (DK541) is difficult to infer especially because of its tenuous taxonomic identity and incompleteness. However, we here estimate the total length (TL) of the fossil shark in life based on two extant odontaspidid (*Odontaspis ferox*) specimens, BPBM 9334 and 9335, housed in Bernice P. Bishop Museum, Honolulu, Hawaii, USA. BPBM 9335 preserves only the head region from a 297-cm-TL individual (sex unknown) in which its sixth vertebra has a diameter of 30 mm. On the other hand, BPBM 9334 is a complete 190-cm-TL female, and its skeleton imaged through computed tomography (CT) reveals that the thirty-third vertebra has the largest centrum and is 1.22 times larger than its sixth vertebra. Thus, the unpreserved thirty-third vertebra in BPBM 9335 likely had a diameter of 36.6 mm (note: exact vertebral measurements in BPBM 9334 cannot be taken from CT images and thus both specimens are needed for our calculation). The largest vertebra in DK 541 has a diameter of 41 mm, which is 1.12 times larger than the inferred diameter of the largest vertebra in BPBM 9335. If the preserved fossil vertebra is assumed to be the largest vertebra in the fossil individual, and if the body form as well as the relationship between the body form and vertebral properties in the fossil shark are assumed to have been the same as in the extant shark, the fossil individual possibly measured 333 cm TL.

The tallest tooth in BPBM 9335 is the second lower anterior tooth (sensu Shimada 2005), and its vertical crown height (CH) is 26 mm. The tallest preserved tooth in the fossil specimen is DK541b, which measures 24 mm CH. Its rather erect crown suggests that it likely represents one of the anterior teeth, but it was likely not the tallest anterior tooth in the dentition because of its sinuous crown. Its CH of 24 mm means that the tooth is 92% of the tallest tooth in BPBM 9335, and this percentage would yield an estimated TL of 274 cm for the fossil shark. This estimated TL is shorter than the TL estimated from the largest vertebra (see above), but this can be explained by the fact that DK541b may not have represented the largest tooth in the fossil individual. Therefore, whereas the tooth-based TL estimation would at least suggest that the fossil shark individual was no smaller than 274 cm TL, we consider the vertebra-based estimation (i.e., *c*. 333 cm TL) to be closer to the actual length of the fossil shark in this particular instance.

Taphonomic remarks

The shark individual represented by associated teeth and vertebrae (DK 541) was found with a tooth (DK541c; Fig. 3) presumably from another shark individual (see above). It is an incomplete tooth preserving only the crown with a main cusp and three cusplets in labial view. The tip of the main cusp is missing but the tooth has an estimated total apicobasal crown height of 10.5 mm with the following characteristics: cutting edges restricted to the narrow uppermost part of the main cusp that widens rapidly mesiodistally towards its base; labial surface flat; one medial pair of high, narrow, and diverging lateral cusplets flanking the main cusp, with height one-third of that of the main cusp and tips bent slightly towards the main cusp; a second (distal) pair of lateral cusplets (one side is missing) similar in shape to the medial pair but with height half of that of the medial pair. Well-developed ridges ornament the base of the labial face under the two mesial cusplets present and form minute tubercles, some of which are arranged on top of one another (the presence of this feature is uncertain on the distal side due to poor preservation). The crown surface is smooth except for a median, faint node at the base of the labial face of the main cusp. The well-developed labial ornamentation at the base of the crown in DK541c is similar to that in *Palaeohypotodus rutoti* (Leriche 1902; Gurr 1962; Cappetta 2012), but the narrow aspect of the main cusp and cusplets is found only in juvenile specimen of this species (Leriche 1951). Furthermore, the stratigraphic range of the genus does not extend over the Ypresian. We therefore leave this tooth in open nomenclature as a second Odontaspididae indet. To note, the estimated crown height of 10.5 mm is only about 40% of the crown height of the tallest tooth in BPBM 9445, giving an estimated TL of 120 cm; this is a distinct minimum value because the tooth likely did not represent the tallest tooth in the dentition.

The occurrence of a tooth from another shark individual with DK541 is taphonomically intriguing. The rock in which the fossil assemblage occurred is composed of fine-grained clays (see above), indicating deposition in a low-energy environment. Because the components of DK541 were all disarticulated and scattered across the sediment, it suggests that the shark carcass must have been lying on the sea floor for some time (e.g., see Schäfer 1972). Because DK541c is represented by a single tooth with no apparent association with other odontaspidid elements found together, it likely represents a shed tooth. The association of DK541c with the skeletal remain of DK541 may be coincidental, but it could be a result of feeding. However, extant odontaspidid sharks do not typically scavenge large animal carcasses (e.g., Compagno 2001) and DK541c seems too delicate to effectively tear off pieces of flesh of a large shark such as DK541. Therefore, if DK541c indeed represents a shed tooth, it could possibly be from feeding on smaller animals that were feeding on the shark carcass.

Conclusion

DK541 from the lower Lutetian part of the Lillebælt Clay Formation in Denmark is determined to be an odontaspidid lamniform shark based on vertebral and dental characteristics. Its tooth morphology suggests that the shark may belong to an undescribed odontaspidid taxon closely allied to *Odontaspis* or *Palaeohypotodus*, but we here conservatively refer to it as Odontaspididae indet. The fossil shark individual was likely no smaller than 274 cm total length based on the largest preserved tooth compared to teeth in extant *Odontaspis ferox*. However, comparison of vertebral sizes between the largest preserved vertebrae in DK541 and that in extant *O. ferox* suggests that the fossil individual possibly measured as much as 333 cm total length. The disarticulated nature of the skeletal and dental components of DK541 in a low-energy deposit suggests that the shark carcass must have stayed on the ocean floor for some time. The fossil individual represented by DK541 was found with a possible shed tooth of another odontaspidid (DK541c) that was likely a smaller individual than DK541.

Acknowledgments

This study represents the senior author's thesis project completed in 2011 as a partial fulfilment of the Bachelor program at the University of Copenhagen. We would like to thank Sten Lennart Jakobsen (conservator at the Geological Museum of Copenhagen), who sectioned the fossil vertebra illustrated in Figure 5A, helped prepare the specimen, and provided photographs of the fossil material. We also thank Arnold Y. Suzumoto (BPBM) for allowing us to study the extant *Odontaspis ferox* specimens, Kenneth Gray, James Hickey, Barbara Karl, Brian Reilly, and Cynthia K. Rigsby (Children's Memorial Hospital, Chicago, Illinois, U.S.A.) for providing us with the CT images of the extant *O. ferox* specimens, and Scott Gallatin and Ashley C. Swanski (Bremen Animal Hospital, Tinley Park, Illinois, U.S.A.) for making the X-ray image used in Figure 5B in this paper. We are thankful to Mogens Madsen for helpful discussion and for bringing some of us to visit the site. David Ward and Sylvain Adnet are thanked for their critical and constructive reviews.

References

Arambourg, C. & Signeux, J. 1952: Les vertébrés fossiles des gisements de phosphates (Maroc-Algérie-Tunisie). Notes et Mémoires du Service Géologique du Maroc 92, 1–372.

Balbino, A.C. & Antunes, M.T. 2007: Pathologic tooth deformities in fossil and modern sharks related to jaw injuries. Comptes Rendus Palevol 6, 197–209.

Becker, M.A., Chamberlain, J. A. & Stoffer, P. W. 2000: Pathologic tooth deformities in modern and fossil chondrichthians: a consequence of feeding-related injury. Lethaia 33, 103–118.

Blanco-Piñón, A., Shimada, K. & González-Barba, G. 2005: Lamnoid vertebrae from the Agua Nueva Formation (Upper Cretaceous: lower Turonian), northeastern Mexico. Revista Mexicana de ciencias geológicas 22, 19–23.

Cappetta, H. 1987: Handbook of paleoichthyology volume 3B, Chondrichthyes II, Mesozoic and Cenozoic Elasmobranchii, 193 pp. Stuttgart, New York: Gustav Fischer Verlag.

Cappetta, H. 2012: Handbook of paleoichthyology volume 3E, Chondrichthyes, Mesozoic and Cenozoic Elasmobranchii: Teeth, 512 pp. München: Verlag Dr. Friedrich Pfeil.

Cappetta, H. & Nolf, D. 2005: Révision de quelques Odontaspididae (Neoselachii: Lamniformes) du Paléocène et de l'Eocène du Bassin de la mer du Nord. Bulletin de l'Institut royal des Sciences naturelles de Belgique, Sciences de la Terre 75, 237–266.

Casier, E. 1966: Faune ichthyologique du London Clay, 496 pp. London: British Museum of Natural History.

Christensen, E.J. & Hald, N. 1991: Danekræ, et nyt begreb i dansk museumslovgivning. Arkæologiske Udgravninger i Danmark 1990, 7–16.

Compagno, L.J.V. 2001: Sharks of the world. An annotated and illustrated catalogue of shark species known to date. Volume 2. Bullhead, mackerel and carpet sharks (Heterodontiformes, Lamniformes and Orectolobiformes), 269 pp. Rome: Food and Agriculture Organization of the United Nations.

Cvancara, A.M. & Hoganson, J.W. 1993: Vertebrates of the Cannonball Formation (Paleocene) in North and South Dakota. Journal of Vertebrate Palaeontology 13, 1–23.

Ehret, D.J., Hubbell, G. & MacFadden, B.J. 2009: Exceptional preservation of the white shark Carcharodon (Lamniformes, Lamnidae) from the Early Pliocene of Peru. Journal of Vertebrate Paleontology 29, 1–13.

Ehret, D.J. Macfadden, B.J., Jones, D.S., Devries, T.J., Foster, D.A., & Salas-Gismondi, R. 2012: Origin of the white shark *Carcharodon* (Lamniformes: Lamnidae) based on recalibration of the Upper Neogene Pisco Formation of Peru. Palaeontology 55, 1139–1153.

Gurr, P.R. 1962: A new fish fauna from the Woolwich Bottom Bed (Sparnacian) of Herne Bay, Kent. Proceedings of the Geologists' Association 73, 419–447.

Heilmann-Clausen, C. 1988. The Danish Subbasin, Paleogene dinoflagellates. In: Vinken, R. (ed.): The Northwest European Tertiary Basin. Results of the International Geological Correlation Programme Project no 124. Geologisches Jahrbuch A 100, 339–343.

Heilmann-Clausen, C. 2012: Koralrev og lerhav. In: Sand-Jensen, K. & Larsen, G. (eds), Naturen i Danmark – Geologien, 2. udgave, 181–226. Copenhagen: Gyldendal.

Heilmann-Clausen, C., Nielsen, O.B. & Gersner, F. 1985: Lithostratigraphy and depositional environments in the Upper Paleocene and Eocene of Denmark. Bulletin of the Geological Society of Denmark 33, 287–323.

Heinicke, M.P., Naylor, G.J.P. & Hedges, S.B. 2009. Cartilaginous fishes (Chondrichthyes). In: Hedges, S.B. & Kumar, S. (eds), The timetree of life, 320–327. Oxford: Oxford University Press.

Howie, F.M.P. 1974: Introduction of thioglycollic acid in preparation of vertebrate fossils. Curator 17, 159–166.

Kozuch, L. & Fitzgerald, C. 1989: A guide to identifying shark centra from southeastern archaeological sites. Southeastern Archaeology 8, 146–157.

Leriche, M. 1902: Les poissons paléocènes de la Belgique. Mémoires du Musée royal d'Histoire naturelle de Belgique 2, 1–48.

Leriche, M. 1951 : Les poissons tertiaires de la Belgique (supplément). Mémoires de l'Institut royal des Sciences naturelles de Belgique 118, 476–600.

Mannering, A.A. & Hiller, N. 2008: An early Cenozoic neoselachian shark fauna from the southwest Pacific. Palaeontology 51, 1341–1365.

Purdy, R.W., Schneider, V.P., Applegate, S.P., McLellan, J.H., Meyer, R.L. & Slaughter, B.H. 2001: The Neogene sharks, Rays, and bony fishes from Lee Creek Mine, Aurora, North Carolina. Smithsonian Contributions to Paleobiology 90, 71–202.

Ridewood, W.G. 1921: On the Calcification of the Vertebral Centra in Sharks and Rays. Philosophical Transactions of the Royal Society of London 210, 311–407.

Schäfer, W. 1972: Ecology and Palaeoecology of Marine Environments, 568 pp. Chicago: University of Chicago Press.

Schnetler, K.I. & Heilmann-Clausen, C. 2011: The molluscan fauna of the Eocene Lillebælt Clay, Denmark. Cainozoic Research 8, 41–99.

Schwarzhans, W. 2007: Otoliths from casts from the Eocene Lillebælt Clay Formation of Trelde Næs near Fredericia (Denmark), with remarks on the diet of stomatopods. Neues Jahrbuch für Geologie und Paläontologie Abhandlungen 246, 69–81.

Shimada, K. 2005: Phylogeny of lamniform sharks (Chondrichthyes: Elasmobranchii) and the contribution of dental characters to lamniform systematics. Paleontological Research 9, 55–72.

Shimada, K., Cumbaa, S.L. & Van Rooyen, D. 2006: Caudal fin skeleton of the Late Cretaceous shark, *Cretoxyrhina mantelli* (Lamniformes: Cretoxyrhinidae) from the Niobrara Chalk of Kansas. Bulletin of the New Mexico Museum of Natural History and Science 35, 185–192.

Siverson, M. 1995: Revision of the Danian cow sharks, sand tiger sharks, and goblin sharks (Hexanchidae, Odontaspididae, and Mitsukurinidae) from southern Sweden. Journal of Vertebrate Paleontology 15, 1–12.

Siverson, M. 1999: A new large lamniform shark from the uppermost Gearle Siltstone (Cenomanian, Late Cretaceous) of Western Australia. Transactions of the Royal Society of Edinburgh: Earth Sciences 90, 49–65.

Vélez-Zuazo, X. & Agnarsson, I. 2011: Shark tales: A molecular species-level phylogeny of sharks (Selachimorpha, Chondrichthyes). Molecular phylogenetics and evolution 58, 207–217.

Ward, D.J. & Wiest, R.L.Jr. 1990: A checklist of Palaeocene and Eocene sharks and rays (Chondrichthyes) from the Pamunkey Group, Maryland and Virginia, USA. Tertiary Research 12(2), 81–88.

White, E.G. 1937: Interrelationships of the elasmobranchs with a key to the order Galea. Bulletin of the American Museum of Natural History 74, 25–138.

New data on eudialyte decomposition minerals from kakortokites and associated pegmatites of the Ilímaussaq complex, South Greenland*

SVEN KARUP-MØLLER & JOHN ROSE-HANSEN

Karup-Møller, S. & Rose-Hansen, J. 2013. New data on eudialyte decomposition minerals from kakortokites and associated pegmatites of the Ilímaussaq complex, South Greenland. ©2013 by Bulletin of the Geological Society of Denmark, Vol. 61, pp. 47–70. ISSN 2245-7070. (www.2dgf.dk/publikationer/bulletin).

A suite of samples with eudialyte and eudialyte decomposition minerals from the kakortokite and associated pegmatites of the Ilímaussaq complex in South Greenland has been investigated by electron microprobe analysis. Extensive decomposition of eudialyte has resulted in the formation of catapleiite as host for a number of rare and hitherto unknown REE minerals besides known minerals such as monazite and kainosite. Mineral A1 is present in very small amounts in nearly all eudialyte decomposition aggregates and comprises two varieties: Ca-rich A1 with composition $HCa_3REE_6(SiO_4)_6(F\square)$ and presumed apatite structure, and Ca-poor A1 with composition $(Fe,Mn,Ca)_{1.5}REE_6Si_6FO_{22}$ and unknown structure. Mineral A2 with composition $(Ca,Fe)_{1.2}REE_4Si_6O_{19-y}(OH)_{2y} \cdot nH_2O$ is indistinguishable from A1 in EMP-backscattered light and has only been found at a limited number of localities. Mineral A2 also occurs as a primary mineral at one locality. Additional rare and new REE-minerals are mineral A3 with composition $Na_{0.2}Ca_{0.6}Fe_{0.2}Mn_{0.5}Al_{0.5}REE_{2.8}Si_6F_{0.5}O)_{18-y}(OH)_{2y} \cdot nH_2O$; mineral Uk2 with composition $REE_{2.00}F_{1.50}O_{2.25-y}(OH)_{2y} \cdot nH_2O$; mineral Uk3 with composition $CaREE_4O_{7-y}OH)_{2y} \cdot nH_2O$; and mineral Y1 with composition $Na_2Ca_4Y_{2.7}REE_{1.3}F_{18}(OH)_4$. The Ce:(Y+La+Pr+Nd+Sm+Gd) molar ratio for A1, A2, A3, Uk2, Uk3 and monazite is close to 1:1. Characteristic for A1, A2 and monazite are substantial solid solutions between La and (Pr+Nd+Sm+Gd) with slowly increasing content of Ce as the content of La increases. A similar pattern does not exist for the REE in fresh eudialyte. Kainosite, identified in one decomposition aggregate, has not previously been found in the Ilímaussaq complex.

Keywords: Greenland, Ilímaussaq, kakortokite, pegmatite, eudialyte decomposition, unknown REE-mineral, monazite, kainosite, apatite group.

S.Karup-Møller [svka@byg.dtu.dk], Department of Civil Engineering, Technical University of Denmark, Brovej, Bygning 118, DK-2800 Lyngby, Denmark. J. Rose-Hansen [rose-hansen@dadlnet.dk], Department of Geoscience and Natural Resource Management, University of Copenhagen, Øster Voldgade 10, DK-1350 Copenhagen K, Denmark.

Received 13 February 2013
Accepted in revised form
22 November 2013
Published online
20 December 2013

*Contribution to the mineralogy of Ilímaussaq no. 143

Increasing demand for rare elements such as Zr, Nb, Ta and the rare earth elements (REE) for the manufacturing of a wide range of advanced materials has emphasized the need for new ore deposits with these elements. Until now these elements were mainly produced from carbonatitic rocks and as by-products from zircon and monazite in beach sands. One of the World's largest deposits of these elements is found in the peralkaline rocks of the Ilímaussaq complex in South Greenland. Estimated resources of some elements in Ilímaussaq are listed in Sørensen (1992).

Peralkaline nepheline syenites, termed "agpaitic" by Ussing (1912), were first described from the Ilímaussaq alkaline complex in South Greenland. Sørensen (1960) redefined agpaitic rocks as peralkaline rocks with chemically complex Zr-Ti silicate minerals such as eudialyte and rinkite instead of the chemically simpler zircon, titanite and ilmenite. Agpaitic rocks have high contents of Na-bearing minerals such as nepheline, arfvedsonite, aegirine, sodalite, eudialyte, steenstrupine and villiaumite (see Table 1 in Sørensen 1992). The most highly developed agpaitic rocks crystallized at very low temperatures. Eudialyte may be termed the type mineral of these rocks (Sørensen 1992).

Eudialyte is the main REE-bearing mineral in the

Ilímaussaq complex. Here the mineral contains 11–14 wt% ZrO_2, 1.7–8.7 wt% REE_2O_3 (Gerasimovsky 1969) and ~1 wt% Nb_2O_5. Eudialyte is a major mineral in the roof zone rocks where it occurs as an interstitial mineral (Bohse *et al*. 1974), and also in the lowest exposed zone of the complex, the kakortokites, where it is a liquidus cumulative mineral.

Extensive decomposition of eudialyte throughout the Ilímaussaq complex has taken place. The two major eudialyte alteration minerals are catapleiite and zircon, as originally described by Ussing (1898) and later summarized and confirmed by Sørensen (1962) and Karup-Møller *et al*. (2010). It is assumed that the formation of catapleiite was caused by residual interstitial liquids at a late magmatic stage whereas the formation of zircon was caused by liquids of external origin (Ussing 1898; Karup-Møller *et al*. 2010). The major eudialyte alteration mineral from the kakortokite area is catapleiite. Alteration of eudialyte in the marginal pegmatite of Ilímaussaq has, in addition to catapleiite and zircon, led to the formation of a number of rare, known and hitherto unknown, minerals present in very small amounts and with grain sizes generally less than 10 μm. These include fergusonite-(Ce), fergusonite-(Y), allanite, monazite, apatite, fersmite, nacareniobsite-(Ce), minerals A1, A2, Nb1, Nb2, Uk1 and Uk2 (Karup-Møller *et al*. 2010). Graser & Markl (2008) have in veins east of the Ilímaussaq complex found allanite as an alteration product after eudialyte.

This paper presents a study of altered eudialyte from eudialyte-rich layers in the kakortokite series and from hydrothermal mineral veins and pegmatites associated with the kakortokites. The study has yielded additional information on the alteration minerals A1, A2, Uk2, monazite, fergusonite-(Ce), fergusonite-(Y) and kainosite-(Y). Two new REE-minerals, A3

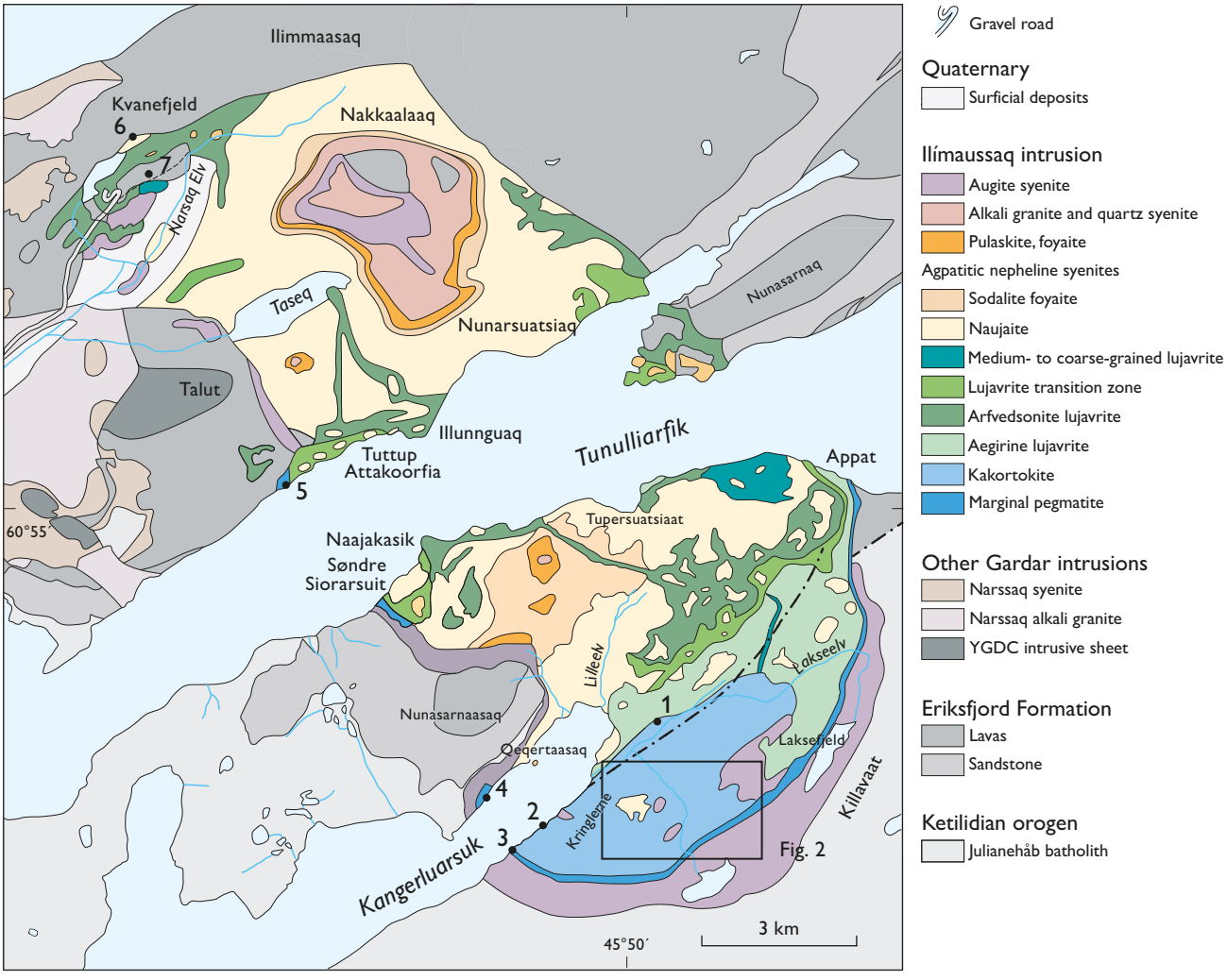

Fig. 1. Simplified geological map of the Ilímaussaq complex based on Ussing (1912), Ferguson (1964) and Andersen *et al*. (1988), redrawn by the Geological Survey of Denmark and Greenland (reproduced with permission). Numbers 1–7 are sample localities outside the area covered by Fig. 2.

and Uk3, and one new Y-rich REE-mineral, Y1, have been identified. The two fergusonite minerals will be treated elsewhere. Mineral A1 has been identified in nearly all eudialyte alteration aggregates from kakortokite, pegmatites and mineral veins, whereas the other alteration minerals occur only in a limited number of samples.

Geological setting of the kakortokite series and associated pegmatites and mineral veins

The Ilímaussaq alkaline complex (Fig. 1) is the type locality of agpaitic nepheline syenites (Ussing 1912). It consists of three main intrusive phases. Phase 1 is a partial rim of undersaturated augite syenite separating the complex from the country rocks. Phase 2 consists of alkali granite and quartz syenite present in the roof zone of the complex. Phase 3 is the main intrusive stage comprising a roof series (from the top and downwards pulaskite, foyaite, sodalite foyaite and naujaite), a floor series (the kakortokites) and in between a series of late lujavrites (e.g. Rose-Hansen & Sørensen 2002; Sørensen 2006; and Sørensen *et al.* 2006). A marginal pegmatite borders the kakortokites in southern Ilímaussaq and is also found at a few localities in the northern part of the complex.

The marginal pegmatite (Ussing 1912; Westergaard 1969; Bohse *at al.* 1971; Karup-Møller *et al.* 2010) consists of agpaitic nepheline syenite and short pegmatitic veins. Within the kakortokite area it has a thickness of about 50 m (Sørensen 1962; Bohse *et al.* 1971; Andersen *et al.* 1988; Karup-Møller *et al.* 2010).

The lower layered kakortokite series (Figs 1 and 2) forms the lowest exposed part of the Ilímaussaq complex (e.g. Ussing 1912; Ferguson 1964; Sørensen 2006; Pfaff *et al.* 2008). It is *c* 200 m thick and consists of a sequence of tri-partite layers each referred to as a unit, and which are repeated at least 28 times. From top to bottom each unit comprises a white layer rich in feldspar and nepheline, a red layer rich in eudialyte, and a black layer rich in arfvedsonite and aegirine. The layering is caused by variation in the modal amounts

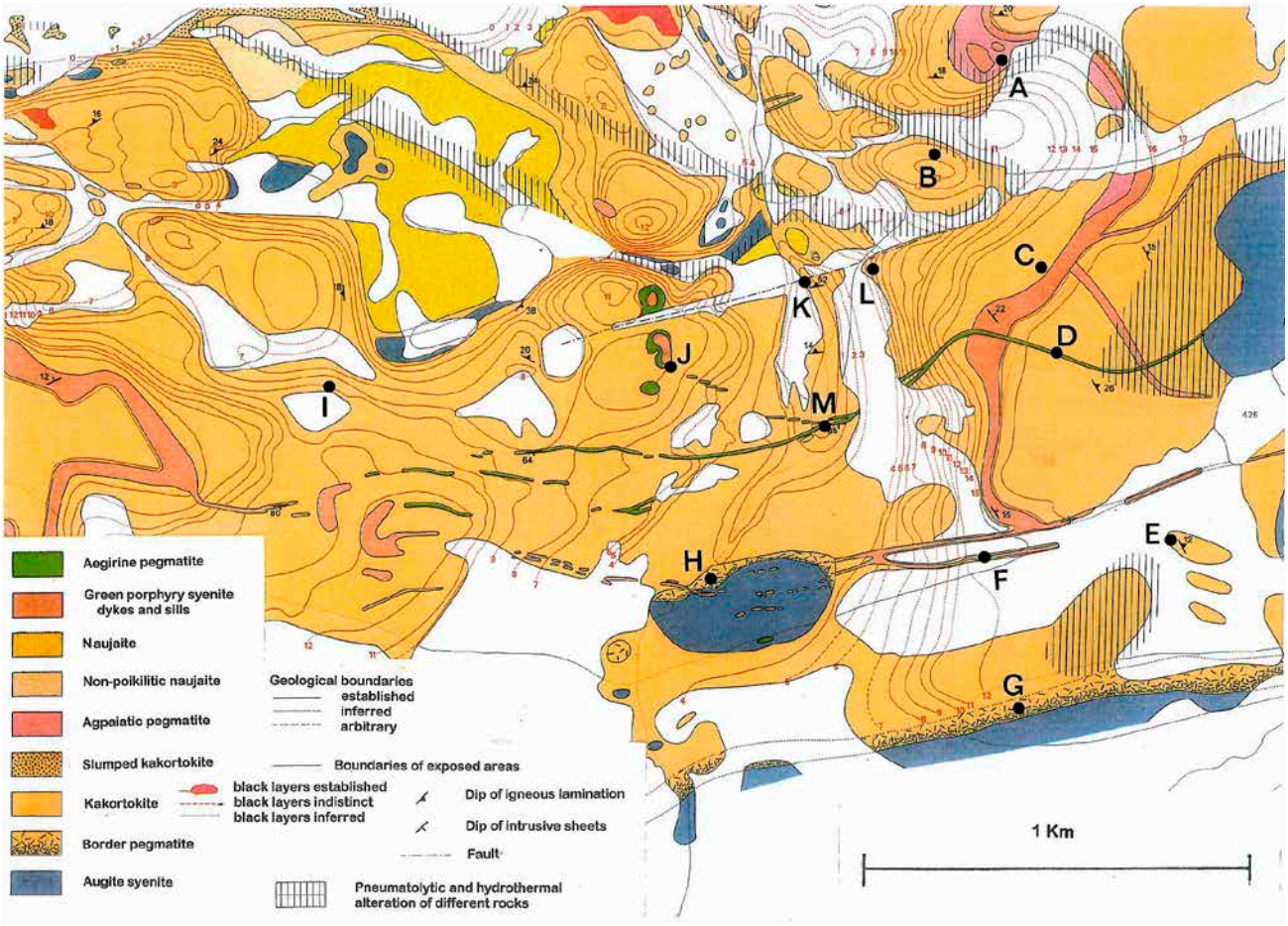

Fig. 2. Geological map of the central part of the kakortokite area, showing sample localities A–M. The map is from Bohse *et al.* (1971) and is reproduced with permission from the Geological Survey of Denmark and Greenland.

of the cumulus minerals. The red and black layers rarely exceed 1 m in thickness. The white layers may reach a thickness of at least 10 m. In the central part of the kakortokite series a distinct unit, named unit 0, has been identified and used as reference level during the mapping of the kakortokite series (Bohse *et al*. 1971). Above this unit, there are 16 units named +1 to +16 in ascending order, and below unit 0 there are 11 units named –1 to –11 in descending order. The lowermost part of the kakortokite is not exposed.

The layered kakortokite series is overlain by *c* 40 m of transitional layered kakortokites in which six eudialyte-rich horizons, named A–F, have been mapped by Bohse *et al*. (1971).

The lujavrites situated between the transitional layered kakortokites and the roof series have a thickness of up to 300 m (Rose-Hansen & Sørensen 2002). They comprise aegirine lujavrite I, aegirine lujavrite II, transitional lujavrite and arfvedsonite lujavrite (Andersen *et al*. 1981; Bohse & Andersen 1981). With decreasing grain size and increasing content of aegirine the transitional layered kakortokites grade into aegirine lujavrite I over a distance of a few metres (Bohse *et al*. 1971). In aegirine lujavrite I there are several eudialyte-rich layers (Henriksen 1993; Bailey 1995), two of which have here been named layer I and II. Layer I is located approximately 5 m from the contact between the transitional layered kakortokites and aegirine lujvrite I and may correspond to layer M1 in drill core 7 logged by Bailey (1995). Eudialyte-rich layer II is located approximately 20 m above layer I. The location is shown in Fig. 1 (loc. 1).

Fig. 3. Agpaitic pegmatite sill at locality A (Fig. 2). The upper 2.5–3.0 m of the sill is distinctly layered. A 10 cm thick grey fine-grained layer (a) in the upper part of the sill separates a more leucocratic lower part from an upper part richer in aegirine and arfvedsonite. Sample 230795 was collected from the grey layer in the pegmatite and samples 151463 and 230797 from the lower part of the pegmatite. Length of hammer handle 43 cm.

Pegmatites and mineral veins

In this work, pegmatites and hydrothermal mineral veins within the kakortokites have been subdivided into three types: agpaitic pegmatites, aegirine pegmatites and oval shaped pegmatites. In addition, there are albititic aplite veins and bodies. The agpaitic pegmatites and several of the largest aegirine pegmatites are shown on the geological map of Bohse *et al*. (1971). The oval-shaped pegmatites and most of the albititic aplites rarely exceed a few metres in size.

The *agpaitic pegmatites* comprise one large sill (Figs 3 and 4) and one vertical dyke. Both are shown on the geological map by Bohse *et al*. (1974). They are mainly

Fig. 4. The upper 1.5 m part of the agpaitic sill shown in Fig. 3, about 100 m east of the location shown in Fig. 3. Here again the grey fine-grained layer (a) separates the sill into a lower leucocratic part (b) and an upper mafic part (c) which is in contact with the overlying trachyte sill (d). A vague layering in the lower and upper parts of the sill is due to slight variations in the proportions of dark and light minerals and grain sizes. Note the two thin layers of coarse material in the fine-grained grey layer. This indicates that the layering of the pegmatite was presumably caused by physical/chemical variations during the crystallization of the sill and is not the result of multiple injections of liquid pegmatitic material.

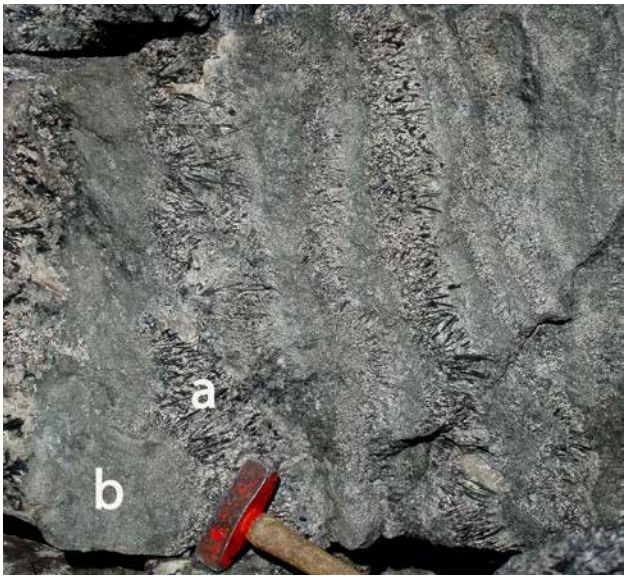

Fig. 5. Aegirine pegmatite in the gully of Laksetværelv (locality M, Fig. 2). Irregular layers of aegirine pegmatitic material (a) alternate with layers of fine-grained green aplitic material (b). The pegmatitic layers are dominated by up to 10 cm long aegirine crystals in poorly shaped rosettes which always grow in the same direction towards east (to the right), indicating that crystallization of the pegmatite took place from west to east.

Fig. 6. Aegirine pegmatite dyke 3 m thick, with marginal zones of very coarse microcline and less coarse central areas (locality B, Fig. 2). Length of hammer handle about 40 cm.

very coarse-grained and dominated by K-feldspar, nepheline and arfvedsonite/aegirine.

The *aegirine pegmatites* vary in thickness from a few centimetres to at least 15 m. They are generally characterized by alternating coarse- and fine-grained, dark green layers which have sharp or gradual contacts against each other (Figs 5 and 6, respectively). The major minerals are feldspar and aegirine.

The *oval-shaped pegmatites* (Figs. 7–9) always occur with sharp contacts against the kakortokite host. Several of these are present at locality I on Fig. 2. The major minerals are K-feldspar, aegirine/arfvedsonite, nepheline and sodalite. Nepheline and sodalite are often partly replaced by analcime.

In addition to the major minerals the pegmatites contain eudialyte (often completely decomposed to secondary minerals) and very small amounts of exotic minerals such as tundrite-(Ce) (Karup-Møller 1982), rinkite, helvite (Johnsen & Bohse 1981), astrophyllite and niobophyllite (Macdonald *et al*. 2007), pectolite, sphalerite, galena, fluorite, native lead and associated secondary litharge and platnerite (Karup-Møller 1975).

Irregularly shaped small *albititic aplites* have either sharp or gradual contacts against the host kakortokite (e.g. at loc. L, Fig. 2). Rarely, albititic aplitic material forms areas within aegirine pegmatites (Fig. 10; loc. J, Fig. 2) and oval-shaped pegmatites (loc. E, F and I, Fig. 2). Albititic aplites also occur as conformable layers in the kakortokite, e.g. at loc. K on Fig. 2. At this locality the aplite layer is about 15 cm thick and can be followed over a distance of about 20 m before disappearing under talus.

Eudialyte and/or eudialyte decomposition products in all pegmatite varieties and in albititic aplites have been included in the present study.

Analytical methods

Electron microprobe analyses were carried out at the Department of Geosciences and Natural Resource Management, University of Copenhagen, using a JEOL 733 superprobe in wavelength dispersive mode with an on-line correction program supplied by JEOL. The accelerating voltage was 15 kV, beam current 15 nA and beam diameter 3 μm. Counting times were 30 seconds on peak positions and 15 seconds on background positions. Wavelengths and standards used were Na *K*α ($NaAlSi_3O_8$), K *K*α ($KAlSi_3O_8$), Ca *K*α and Si *K*α ($CaSiO_3$), Mn *K*α ($MnTiO_3$), Fe *K*α (Fe_2O_3), Al *K*α (Al_2O_3), Ce *L*α (CeO_2), La *L*α (18 wt% La_2O_3 in synthetic glass), Nd *L*α ($Nd_3Ga_5O_{12}$), Pr *L*α ($Pr_3Ga_5O_{12}$), Sm *L*α ($SmFeO_3$), Y *L*α ($Y_3Al_5O_{12}$), Gd *L*α ($GdFeO_3$), Dy, Yb and Er *L*α (all three elements in synthetic silica glass standards), P *L*α and F *K*α (apatite-Wilberforce), Nb *L*α (columbite), Th *M*α (ThO_2), U *M*α (UO_2), and Cl *K*α (sodalite). The estimated detection limit is 0.02 wt% for all elements.

Up to 10 analyses were completed on each phase in a given eudialyte alteration aggregate. All microphotos are back-scattered electron (BSE) images. The analyses of alteration minerals are available in a supplementary data file at the web site http://2dgf.dk/publikationer/bulletin/191bull61.html.

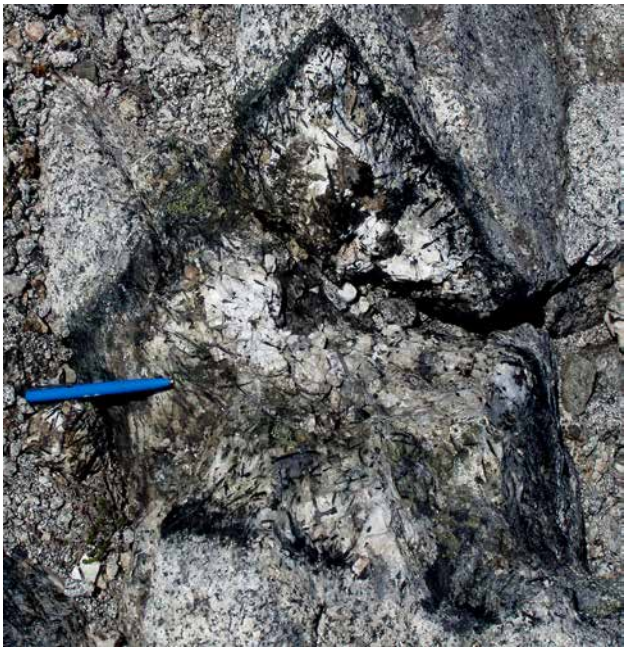

Fig. 7. Small pegmatite geode with high concentrations of aegirine in the border zone against the host kakortokite. The central area is dominated by microcline with minor aegirine and totally decomposed eudialyte (locality I on Fig. 2). About 14 cm ball point pencil for scale.

Fig. 8. Circular pegmatite (a) at locality F with sharp contact against kakortokite (b). The pegmatite is composed of fine-grained aegirine in dense aggregates (1), nepheline (2), microcline (3), eudialyte (4) and arfvedsonite or aegirine (5). Width of photo *c* 60 cm.

Samples studied

Samples with fresh eudialyte and/or totally decomposed eudialyte were taken from the eudialyte-rich red layers in kakortokite units –11, –9, –5, 0, +7, +9, +16, from the eudialyte-rich layers B and D in the transitional layered kakortokite above layer +16, and from the two eudialyte-rich layers I and II in the aegirine lujavrite I. The sample from unit –11 was taken in the white feldspar- and nepheline-rich layer because the red kakortokite layer of this unit was not exposed. Numerous specimens were collected from all three pegmatite types and from albititic aplites. In addition,

Fig. 9. Extremely microcline-rich oval-shaped pegmatite in the kakortokite layer +9 at locality I (Fig. 2). The microcline crystal at the hammer head is more than 30 cm long.

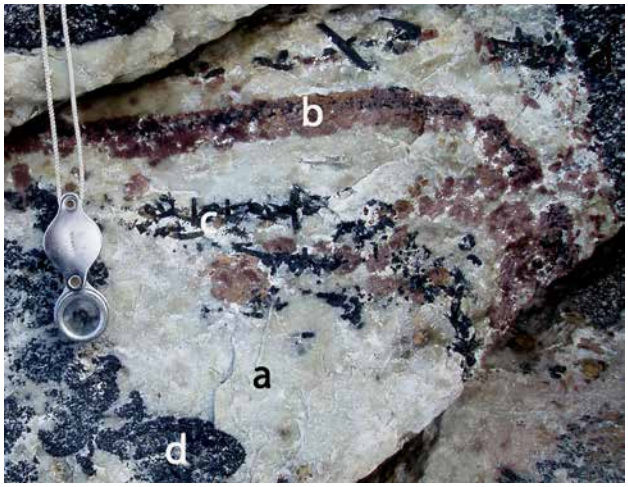

Fig. 10. Fine-grained albititic aplite (a) in the aegirine pegmatite at locality J (Fig. 2), enclosing layered and randomly distributed eudialyte (b) and aegirine (c). Intensely corroded kakortokite remnants (d) are seen in the bottom left part of the photograph. Hand lens 8 cm long.

Table 1. List of investigated layers and samples

Sample	Description	Locality
Layers I, II	Eudialyte-rich layers in green lujavrite	1
Layers A, B, D	Eudialyte-rich layers in transitional kakortokites	1
Layers –11, –9, –5	Eudialyte-rich layers in lower layered kakortokite series	2
Gr2	Marginal pegmatite	3
104361	Marginal pegmatite	4
109302, 109303, 109304	Marginal pegmatite	5
104380	Marginal pegmatite	6
Bore holes 44-22.9 and 48-42.5	Mineralized lujavrites	7
151463; 230790, -91, -95, -96, -97	Agpaitic pegmatite	A
Layer +16	Eudialyte-rich layer in lower layered kakortokite series	A
151460, 230790	Aegirine pegmatite	B
151467	Aegirine pegmatite	C
231301, 231302	Aegirine pegmatite	D
151426, 151428	Circular pegmatite	E
151432	Aplitic phase in circular pegmatite	E
23-1, 23-2, 23-3	Circular pegmatite	F
188188	Marginal pegmatite	G
199195	Marginal pegmatite	H
199199, 199200	Circular pegmatite	I
Layers +7, +9	Eudialyte-rich layer in lower layered kakortokite series	I
151564	Aegirine pegmatite sill	J
Layer 0	Eudialyte-rich layer in lower layered kakortokite series	K
151437	Conformable albititic aplite	K
199176, 199177, 199178	Albititic aplite in kakortokite layer +5	L

Localities 1–7 are shown in Fig. 1 and localities A–L are shown in Fig. 2. The detailed positions of marginal pegmatite and bore holes on Kvanefjeld (Locs 6 and 7) are shown on the geological map of the Kvanefjeld area in Sørensen *et al*. (1974).
All six-digit sample numbers are GGU numbers.

data recorded on mineral A1 from the marginal pegmatite (loc. A–D in Fig. 1 of Karup-Møller *et al*. 2010) have been included in the present study. Monazite from a relatively large number of localities within the kakortokite area (samples 23-2, 23-3, 151428, 199199, layers –9 and –11), the marginal pegmatite (samples 104361, 104380, 199159, 199188) and in drill cores 44-22.9 m and 48-42.5 m from Kvanefjeld, has also been analyzed. All sample localities are shown on Figs 1 and 2 and listed in Table 1.

Mineral descriptions and results

Eudialyte

Analyses of fresh eudialyte were obtained for selected samples from the lujavrite-kakortokite profile, from pegmatitic material at localities E and F, and from albititic aplite at localities E and I (Fig. 2). Small systematic changes in the composition of the mineral were recorded and will be described elsewhere. The average composition of eudialyte in selected samples from the lower layered kakortokite series (units –11, –9, –5, 0, +7, +9, +16) and the transitional layered kakortokites (layers B and D) is listed in Table 3 (no. 1). Following Johnsen & Grice (1999) the analysis has been recalculated on the basis of 29 (Si+Al+Zr+Ti+Nb).

Correlation coefficients for REE in eudialyte are shown in Table 2. All values between 0.1 and –0.1 are considered to be of no significance. Only a weak correlation exists between the elements. Ce is negatively correlated with all the other REE except La. Y is positively correlated with La and Nd but negatively correlated with Pr, Sm and Gd. The weak positive correlation between La and Nd is in sharp contrast to the strong to very strong negative correlation between these two elements in the secondary minerals. The eudialyte analyses are indicated as encircled fields in Fig. 11.

Eudialyte decomposition minerals

Decomposition of eudialyte in the kakortokite series and associated pegmatites and mineral veins has re-

sulted in the formation of catapleiite hosting a number of rare minerals similar to those found in decomposed eudialyte from the marginal pegmatite (Karup-Møller *et al*. 2010). During decomposition, most of the REE in the original eudialyte became concentrated in Ca-rich mineral Al, Ca-poor mineral A1, and some in mineral A2, fergusonite and monazite. Of interest for the study of the minerals A1 and A2 is the distribution of REE in these. Correlation coefficients for REE in A1, A2 and monazite have been calculated.

Table 2. Correlation matrix for REE in eudialyte

	Y	La	Ce	Pr	Nd	Sm	Gd
Y	1.00						
La	0.15	1.00					
Ce	–0.31	0.04	1.00				
Pr	–0.36	–0.30	–0.30	1.00			
Nd	0.44	0.22	–0.18	–0.38	1.00		
Sm	–0.16	–0.22	–0.28	–0.04	–0.10	1.00	
Gd	–0.26	–0.40	–0.29	–0.04	–0.26	–0.09	1.00

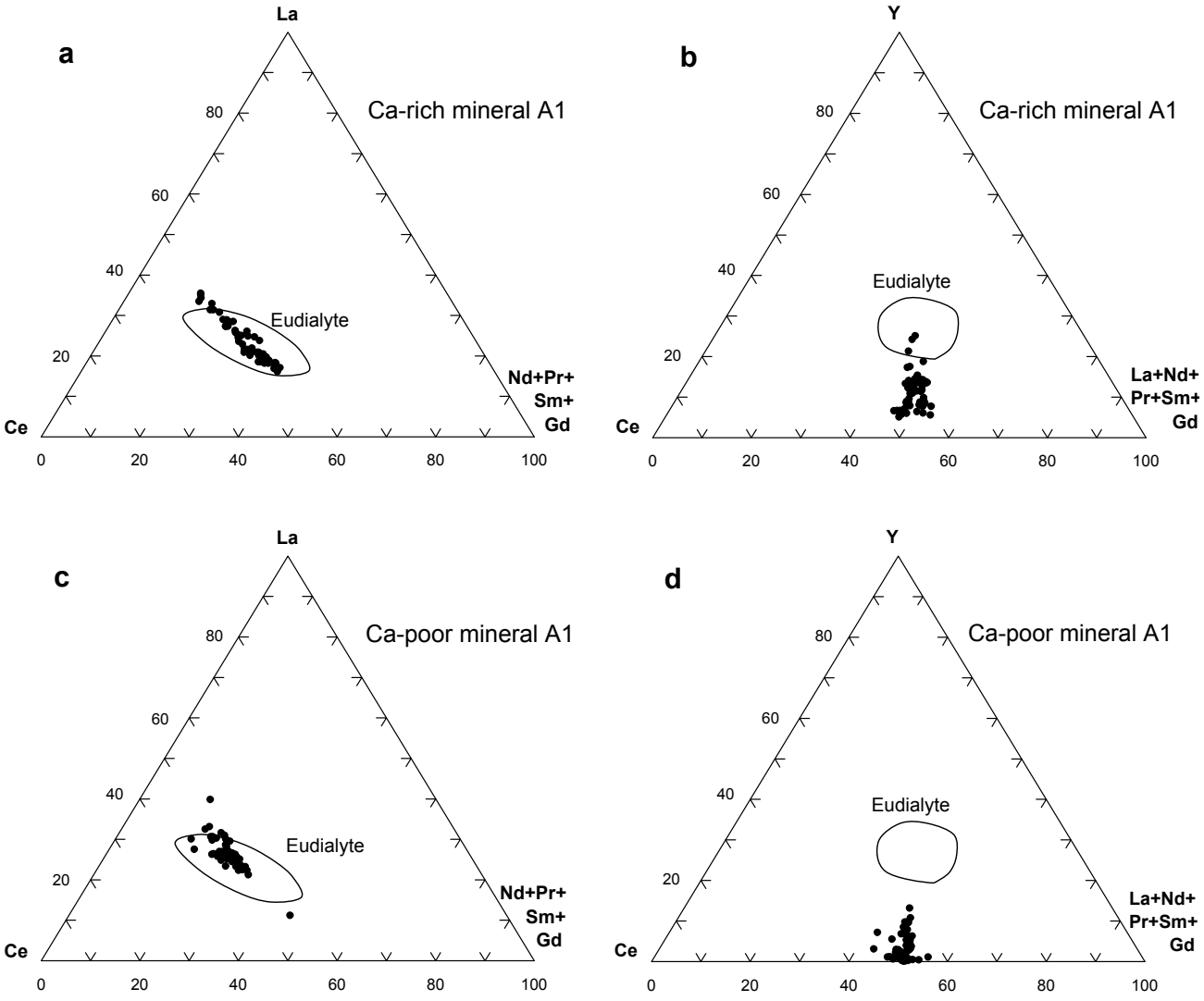

Fig. 11. Molar plots of REE in mineral A1. Analyses of unaltered eudialyte plot within the encircled areas.

Table 3. Microprobe analyses of mineral A1

	1	2	3	4	5	6	7
Mineral	Eudialyte	Ca-rich A1	Ca-poor A1	Ca-poor A1	Altered A1	Altered A1	Ca-poor A1
	Average*	Average	Average	Fig. 16 (c)	Fig. 16 (d)	Fig. 16 (e)	Fig. 17 (c)
No. of analyses	243	106	270	3	3	3	5
SiO_2	49.51 (.36)	22.64 (.57)	23.58 (.59)	19.12 (.07)	21.53 (.50)	18.69 (.67)	20.55 (.52)
TiO_2	0.10 (.01)	-**	-	0.35 (.03)	0.38 (.13)	0.98 (.06)	0.63 (.08)
ZrO_2	11.71 (.15)	0.19 (.48)	0.22 (.29)	-	0.02 (.02)	0.04 (.04)	0.07 (.05)
ThO_2	-	0.11 (.09)	0.22 (.28)	0.20 (.14)	4.99 (.98)	8.23 (.70)	5.83 (.87)
P_2O_5	-	0.81 (.45)	0.44 (.01)	6.00 (.64)	1.28 (.16)	0.81 (.17)	1.18 (.15)
Al_2O_3	0.25 (.02)	-	0.18 (.18)	0.08 (.03)	0.35 (.01)	1.77 (.04)	0.78 (.07)
Nb_2O_5	0.76 (.13)	-	-	0.27 (.12)	1.30 (.59)	6.61 (.66)	3.95 (.60)
Y_2O_3	0.46 (.05)	4.02 (2.00)	1.18 (1.26)	0.36 (.06)	0.70 (.26)	3.04 (.19)	2.38 (.33)
La_2O_3	0.48 (.03)	12.81 (3.34)	16.67 (2.67)	19.63 (.69)	11.87 (.76)	11.07 (.60)	13.41 (1.05)
Ce_2O_3	0.97 (.07)	26.78 (2.30)	31.66 (2.10)	32.33	29.82 (.42)	25.33 (.74)	27.67 (.65)
Pr_2O_3	0.13 (.02)	2.54 (.43)	2.71 (.43)	2.46 (.30)	2.49 (.27)	1.88 (.34)	2.39 (.35)
Nd_2O_3	0.39 (.04)	11.64 (2.43)	10.99 (1.99)	9.69 (.49)	11.66 (.85)	7.66 (.56)	8.96 (.52)
Sm_2O_3	0.11 (.02)	2.75 (1.00)	1.98 (.68)	1.56 (.36)	1.99 (.35)	1.36 (.27)	1.61 (.23)
Gd_2O_3	0.10 (.04)	1.86 (.80)	0.89 (.59)	0.27 (.07)	0.64 (.16)	0.90 (.12)	0.87 (.26)
FeO	6.10 (.27)	0.13 (.31)	2.01 (.69)	1.19 (.04)	1.25 (.19)	0.96 (.12)	1.22 (.07)
MnO	0.68 (.05)	0.00	0.45 (.49)	1.35 (.08)	1.15 (.05)	2.71 (.23)	1.22 (.29)
CaO	9.89 (.58)	11.07 (.69)	2.90 (.90)	0.78 (.12)	1.97 (.21)	1.61 (.10)	1.94 (.06)
K_2O	0.28 (.06)	-	-	-	0.04 (.01)	0.04 (.04)	0.05 (.01)
Na_2O	14.53 (.54)	0.00	0.26 (.37)	2.63 (.26)	0.32 (.03)	0.04 (.04)	0.28 (.06)
F	0.05 (.02)	1.34 (.15)	1.01 (.26)	1.08 (.04)	1.18 (.06)	0.86 (.07)	1.16 (.07)
Cl	1.40 (.14)	-	-	-	-	-	-
F,Cl–O corr.	–0.34	–0.56	–0.43	–0.45	–0.50	–0.36	–0.49
Total	97.56	98.13	96.92	98.90	94.43	94.23	95.66
Atoms based on Si+Zr+P = 6.00**							
Si	25.68	5.80	5.89	4.74	5.71	5.78	5.80
Ti	0.03	-	-	0.06	0.08	0.23	0.13
Zr	2.96	0.02	0.04	-	-	0.01	0.01
Th	-	0.01	0.01	0.01	0.30	0.58	0.38
P	-	0.18	0.07	1.26	0.29	0.21	0.19
Al	0.15	-	0.05	0.02	0.11	0.65	0.39
Nb	0.18	-	-	0.03	0.16	0.93	0.51
Y	0.13	0.55	0.16	0.05	0.10	0.50	0.36
La	0.09	1.21	1.54	1.80	1.16	1.27	1.40
Ce	0.18	2.52	2.90	2.94	2.90	2.87	2.87
Pr	0.03	0.24	0.25	0.22	0.24	0.21	0.25
Nd	0.07	1.07	0.98	0.86	1.11	0.85	0.91
Sm	0.01	0.24	0.17	0.13	0.18	0.15	0.16
Gd	0.01	0.15	0.07	0.02	0.06	0.09	0.08
ΣREE	0.53	5.98	6.07	6.02	5.75	5.94	6.03
Fe	2.66	0.03	0.42	0.25	0.28	0.25	0.29
Mn	0.30	-	0.09	0.28	0.26	0.71	0.29
Ca	5.50	3.04	0.78	0.21	0.56	0.53	0.59
K	0.18	-	-	-	0.01	0.01	0.02
Na	14.62	-	0.13	1.27	0.16	0.03	0.15
F	0.09	1.08	0.80	0.85	0.99	0.84	1.03
Cl	1.23						

* - = below detection limit Numbers in parentheses are 1σ

** The eudialyte recalculation is based on 29 (Si+Ti+Zr+Al+Nb)

1: Average of eudialyte from the kakortokite series. 2: Average of all Ca-rich mineral A1 analyses. 3: Average of all Ca-poor mineral A1 analyses. 4–7: Analyses of fresh and altered Ca-poor mineral A1 in sample 23-2 (circular pegmatite).

Mineral A1

Mineral A1 appears occasionally as individual lath-shaped crystals in random distribution throughout eudialyte alteration aggregates, but it is mostly found in clusters of crystals (Figs 12 and 13).

Karup-Møller *et al*. (2010, their Table 2) found the average composition of A1 in eudialyte decomposition aggregates from the marginal pegmatite to be $(Na,Ca,Fe,Mn)_2Ce_3REE_3Si_6FO_{22.5}$. However, additional microprobe analyses on this mineral in altered eudialyte from the kakortokite area have proved the existence of two varieties, a Ca–rich A1 and a Ca-poor A1. Continuous solid solution between these two varieties does not appear to exist. In Fig. 14 both phases show sharp contacts to each other, confirming this conclusion. They have therefore been treated separately.

The major chemical difference between Ca-rich and Ca-poor mineral A1, apart from their Ca contents, is the presence of small contents of Fe, Mn and Na in Ca-poor A1. Mn and Na have not been detected in Ca-rich A1 and the average content of Fe in this mineral is less than 0.1 wt%. The proportions between the REE in the two A1 varieties are rather similar (Table 3). The most noteworthy difference is the higher contents of Ce and La and the lower contents of Y in Ca-poor A1 compared to Ca-rich A1.

A pronounced variation in the content of individual REE, in particular La and Nd, exists for both mineral varieties from grain to grain in individual decomposition aggregates. In order to determine the substitutional relationships between the elements, correlation matrices (Tables 4 and 5) and triangular plots for certain elements and element combinations (Fig. 11) were completed on all A1 analyses, leading to the average values in Table 3 (nos 2–3). The results of the substitutional relationships are reported below.

Ca-rich mineral A1

The average composition of a total of 106 individual analyses of Ca-rich A1 is listed in Table 3 (no. 2). Characteristic for all analyses is a molar ratio of Si (+Zr+P) to REE close to 1:1. Only limited analyses for the HREE Dy, Yb and Er were completed on Ca-rich A1 in sample 230795 (see the supplementary data file).

From the correlation matrix in Table 4 it is seen that Ca is negatively correlated with Ce, Y and La but positively correlated with Nd, Pr, Sm and Gd. Cerium is also negatively correlated with these four elements and Y, but positively correlated with La. There is a strong positive correlation internally between Nd, Pr, Sm and Gd. These relationships can to some extent also be read from Fig. 11a. Here a linear relationship shows that a decreasing content of Pr+Nd+Sm+Gd is accompanied by an increasing content of La and

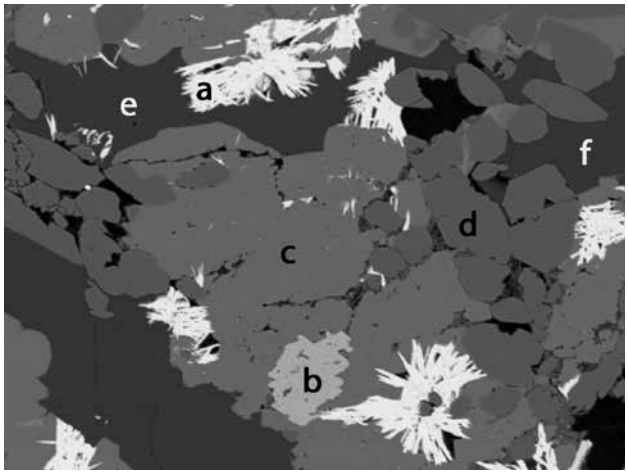

Fig. 12. Eudialyte decomposition aggregate composed of Ca-poor mineral A1 (a), zircon (b), catapleiite (c), aegirine (d), possibly analcime (e), and K-feldspar (f). Sample 231301. Width of image 0.26 mm.

Fig. 13. Cluster of lath-shaped mineral A1 crystals isolated in K-feldspar. Kakortokite layer 0. Width of image 0.07 mm.

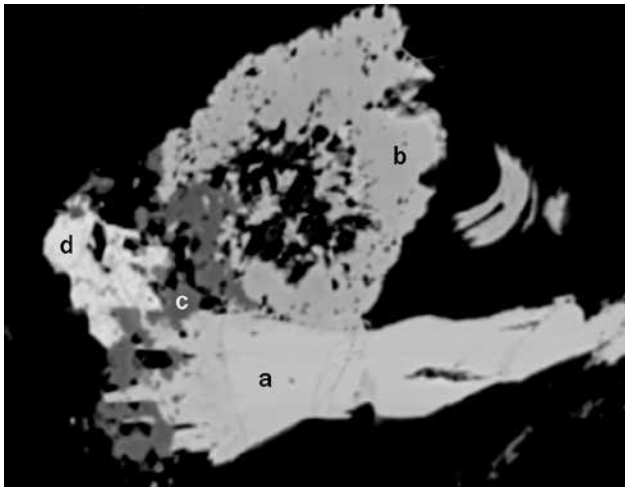

Fig. 14. Aggregate composed of Ca-poor A1 (a), Ca-rich A1 (b), an unidentified Nb-mineral (c) and fergusonite (d). Sample 151437, albititic aplite. Width of image 0.06 mm.

Table 4. Correlation matrix for elements in Ca-rich mineral A1

	Ca	Y	La	Ce	Pr	Nd	Sm	Gd
Ca	1.00							
Y	–0.11	1.00						
La	–0.47	–0.18	1.00					
Ce	–0.53	–0.61	0.75	1.00				
Pr	0.04	–0.27	–0.47	–0.14	1.00			
Nd	0.22	–0.28	–0.83	–0.33	0.66	1.00		
Sm	0.36	–0.14	–0.87	–0.53	0.56	0.91	1.00	
Gd	0.53	0.10	–0.84	–0.76	0.40	0.68	0.78	1.00

a moderate increase in the content of Ce. Finally Y displays a weak negative correlation with La, Pr, Nd and Sm, but a very weak positive correlation with Gd. The small plot area in Fig. 11b confirms these poorly defined relationships. Calcium follows Pr, Nd, Sm and Gd but has not been included in the plot.

Ca-poor mineral A1

The average composition of 270 analyses of Ca-poor A1 is listed in Table 3 (no. 3). As for the Ca-rich A1, the molar ratio of Si (+Zr+P) to REE is close to 1:1. The correlation matrix for Ca-poor A1 (Table 5) is, with a few exceptions, similar to that for Ca-rich A1. It is seen that Fe is positively correlated with Ca. A major difference between the two matrices is the positive correlation between Ca and Pr, Nd, Sm and Gd in Ca-rich A1 and the negative correlation between these elements in Ca-poor A1. In Fig. 11c the analyses cluster in a slightly oval-shaped area in rather sharp contrast to the linear relationships recorded for Ca-rich A1 (compare Fig. 11a with 11c). The plots in Figs 11b and 11d are similar; the only difference is higher contents of Y in Ca-rich A1 than in Ca-poor A1.

Nb-bearing Ca-poor mineral A1

Ca-poor A1 with small amounts of Nb and Th was found in sample 23-3 from the small and poorly exposed pegmatite at locality F in Fig. 2. It occurs within cavities in aegirine after an unknown mineral, probably villiaumite (NaF), and the following minerals were formed: catapleiite, Ca-poor A1, monazite, an unidentified Nb-mineral, thorite, and poorly defined Mn-hydroxides or carbonates.

Catapleiite is the dominant mineral in the aggregate shown in Fig. 15. The mineral occurs as thin laths forming a pseudohexagonal open intergrowth. Cavities are partly filled with the unidentified Nb-mineral. Enclosed between the catapleiite laths there are a few relatively large and almost completely decomposed Ca-poor A1 crystals. The most centrally placed of these is shown in Fig. 16 where the different REE-minerals can be distinguished. The precipitation of the Nb-mineral in cavities between catapleiite crystals is accompanied by its crystallization along fractures. Presumably at the same time almost complete replacement of the original A1 (Table 3 no. 4) took place. Two stages in this replacement process can be recognized in Fig. 16. In the lower left part of the picture the two A1-like replacement phases (d and e) can be recognized. Analyses of these two phases are listed in Table 3, nos 5 and 6. As a result of this replacement process, Na was almost completely removed from the primary A1 and the content of P was strongly reduced. The content of Nb, Th and Al was increased from close to nil in A1 to substantial amounts in the phase at point e in Fig. 16. The total content of REE was not signifi-

Table 5. Correlation matrix for elements in Ca-poor mineral A1

	Ca	Fe	Y	La	Ce	Pr	Nd	Sm	Gd
Ca	1.00								
Fe	0.15	1.00							
Y	0.36	0.15	1.00						
La	–0.18	–0.14	–0.58	1.00					
Ce	–0.66	–0.31	–0.80	0.57	1.00				
Pr	–0.41	–0.13	–0.24	0.36	0.42	1.00			
Nd	–0.33	–0.06	–0.08	–0.67	–0.10	0.66	1.00		
Sm	–0.06	0.01	–0.43	0.31	–0.73	0.71	0.34	1.00	
Gd	0.10	–0.25	–0.30	0.11	–0.38	–0.38	0.15	0.56	1.00

cantly changed as a result of this alteration process, but the REE distribution changed. A decrease in the element oxide sum from 99.35 wt% in the primary A1 to 94.59 wt% in the most replaced variety (Table 3 no. 6) suggests that hydration (or carbonatization) accompanied the replacement process.

Figure 17 shows crystals of catapleiite that have grown from the walls of an empty space. A group of Nb-bearing A1 lamellae (composition in Table 3 no. 7) occurs in the bottom right part of the picture. The mineralization was terminated by the precipitation of a thin crust of the Nb-mineral upon the catapleiite crystals, sometimes filling cavities between these as seen in Figs 15 and 16. The composition of the Nb-bearing A1 lamellae resembles the composition of the Nb-bearing last phase in the replacement process after

Fig. 15. Cavity in aegirine (a) filled with lamellar catapleiite (b) which encloses strongly altered Ca-poor A1 crystals (c). Cavities between the catapleiite crystals (d) are partly filled with an unidentified Nb-bearing mineral (e). It is not possible to distinguish between A1 and the Nb-mineral in the picture. Therefore the lower central part of the area, covering most of the A1 crystals, is shown at a lower electron flux in Fig. 16. Sample 23-2, circular pegmatite. Width of image 0.46 mm.

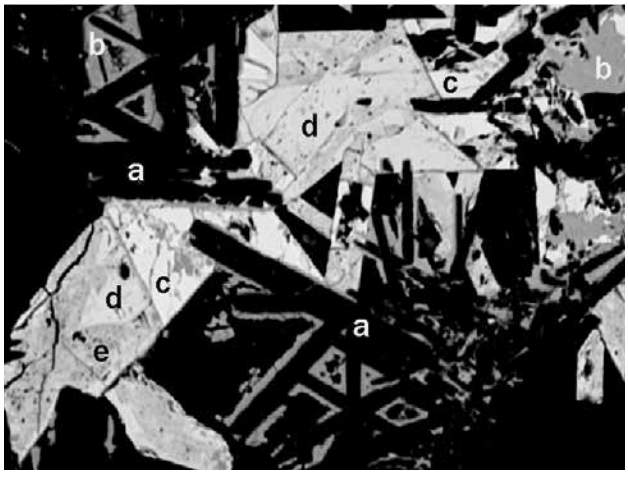

Fig. 16. The lower central area in Fig. 15 recorded at low electron flux which has resulted in easy distinction between the various phases present. Catapleiite (a) is encrusted by a thin layer of an unidentified Nb-mineral (b); sometimes cavities are completely filled with this mineral. The majority of early precipitated A1 (c) has been altered. Two stages (d) and (e) in this alteration process can be recognized. Width of image 0.21 mm.

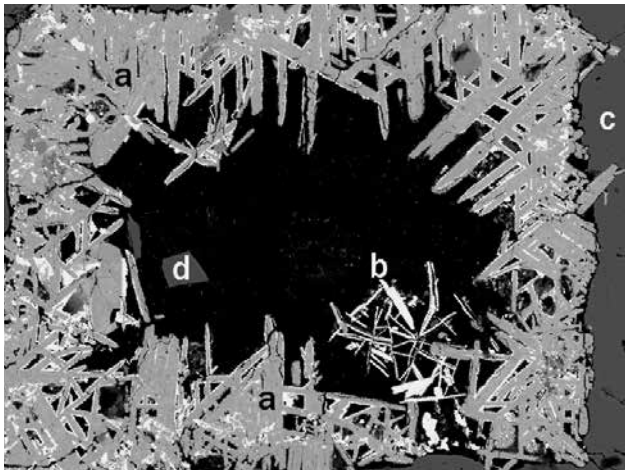

Fig. 17. Cavity in aegirine close to the cavity shown in Figs 15 and 16, partly filled with catapleiite crystals (a), Ca-poor A1 (b) and an unidentified Nb-mineral encrusting catapleiite crystals and partly filling cavities between these (c). The central black area with a crystal of aegirine (d) is epoxy-filled empty space. Sample 23-2, circular pegmatite. Width of image 0.70 mm.

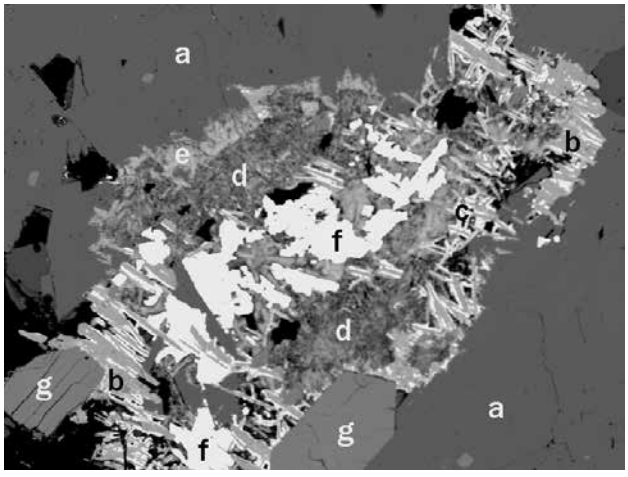

Fig. 18. Cavity in K-feldspar (a) filled with catapleiite (b) encrusted by an unidentified Nb-mineral (c, grey-white), and two Mn-hydroxides and/or carbonates (d, e) enclosing an aggregate (f) of monazite and thorite indistinguishable from each other on the figure. Aegirine crystals (g) are also present. Sample 23-2, circular pegmatite. Width of image 1.64 mm.

mineral A1 in Fig. 16. A similar replacement process may also have taken place here (Fig. 17) but cannot be recognized due to the small size of the lamellae.

In another mineral aggregate in the same sample (Fig. 18), we have identified a heterogeneous mixture of catapleiite, the unidentified Nb-mineral, two Mn-hydroxides or carbonates, monazite and thorite.

Mineral A2

In contrast to mineral A1, mineral A2 was only found at a limited number of pegmatite localities within the kakortokite area. Like A1, it occurs as a secondary mineral in eudialyte decomposition aggregates. In backscattered images in the microprobe it is not possible to distinguish between the two minerals. Mineral A2 was originally found in sample 104361 from the marginal pegmatite (Loc. 4, Fig. 1) (Karup-Møller *et al*. 2010). In one sample mineral A2 was also found as a primary mineral (Fig. 19). In another sample a phase close in composition to A2 was identified (Fig. 20). The compositions of all the phases mentioned are listed in Table 6.

Mineral A2 has a molar ratio of Si:REE close to 3:2. It has no detectable contents of Zr, Ti, Th, Al, P or F. A2 is relatively rich in Y and to some extent also Gd compared to A1. This would imply that the mineral also contains relatively high amounts of HREE, but as seen from Table 6 this is not the case. The low element oxide sum obtained therefore cannot be explained by missing HREE but indicates that A2 is a hydrous or carbonate-bearing mineral . The analyses of A2 in the eudialyte decomposition aggregates show that there is a large difference in composition from grain to grain within the same sample (and often also from grain to grain within individual decomposition aggregates). In order to illustrate the substitutional relationships between the elements in A2, correlation coefficients and element plots similar to those carried out for mineral A1 are presented.

From the correlation matrix in Table 7 it is seen that both Ca and Fe are positively correlated with La and negatively correlated with the other REE. Thus grains relatively rich in La contain relatively more Fe and Ca than those poorer in La. There is no correlation between Y and Ca and only a weak positive correlation between Y and Fe. Furthermore, La is positively correlated with Ce and negatively correlated with Pr, Nd, Sm and Gd. This is also evident from the triangular Ce-La-(Pr+Nd+Sm+Gd) plot in Fig. 21a. Table 7 shows that Y is negatively correlated with the other REE. This is also seen from the plot Ce-Y-(La+Pr+Nd+Sm+Gd) in Fig. 21b. Here the A2 plot covers a rather broad range and overall increasing contents of Y are accompanied by decreasing contents of all other REE.

The original formula for A2 from the marginal pegmatite (Karup-Møller *et al*. 2010) was proposed as $REE_3Si_4O_{12.5-y}(OH)_{2y} \cdot nH_2O$, ignoring the small amounts of Fe and Ca recorded. On the basis of the average A2 analyses in Table 6 no. 1, the following simplified empirical formula for A2 is here proposed: $(Ca,Fe)_{1.2}REE_4Si_6O_{19.2-y}(OH)_{2y} \cdot nH_2O$.

In sample 231301, mineral A2 was found as a primary mineral enclosed in a fine-grained homogeneous intergrowth of aegirine and analcime. The sample represents the fine-grained albite phase of the large aegirine pegmatite at locality D, Fig. 2. Here the A2 grains are relatively large (Fig. 19) and all delicately zoned. The lightest zones have a composition close to that of A2 in the eudialyte decomposition aggregates (Table 6 no. 2). The darkest zones have a high content

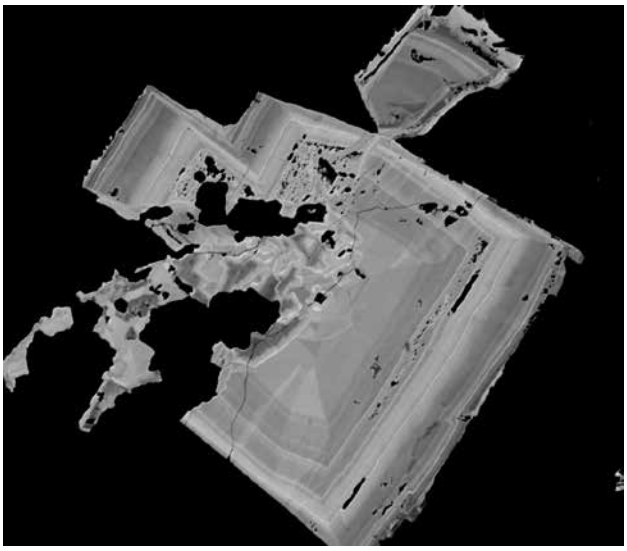

Fig. 19. Primary mineral A2 grain showing zoning. Sample 231301, aegirine pegmatite. Width of image 0.21 mm.

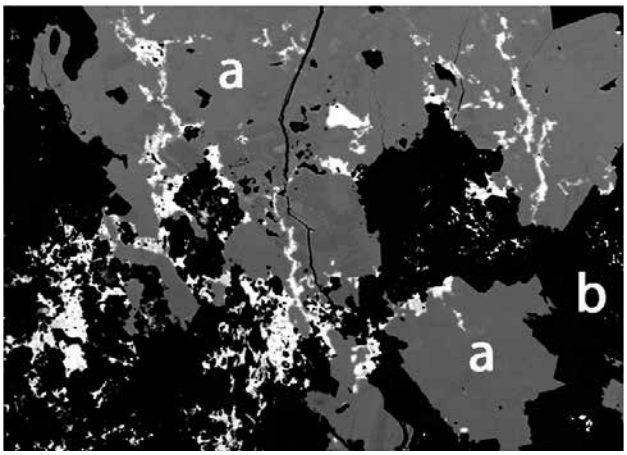

Fig. 20. Irregular veinlets and patches of mineral A2-like phase (white) in zircon (a) and K-feldspar (b) in a eudialyte decomposition aggregate. Sample 151460, aegirine pegmatite. Width of image 0.29 mm.

of Y and correspondingly lower content of the other REE, particularly Ce and Nd (Table 6 no. 3). A gradual change in composition of the mineral from light to dark zones is assumed to exist. The compositional range of mineral A2 is thus defined by, at the one end, the darkest zones in the A2 grains in sample 231301 with maximum content of Y and corresponding low contents of the other REE, and, at the other end, by A2 grains in eudialyte decomposition aggregates with minimum content of Y and correspondingly high contents of the other REE.

A mineral close in composition to A2 was found in sample 151460. The mineral occurs as irregularly shaped veinlets grading into clusters of disseminated grains in zircon and K-feldspar (Fig. 20). The proportions between the individual REE in A2 and in this mineral variety are strikingly different (Table 6 no. 4) but the Si:REE ratio of 6:4.47 is close to that of ideal A2.

Table 6. Microprobe analyses of mineral A2

	1	2	3	4	5
	Av. secondary	Primary, light	Primary, dark	Secondary	Secondary
No of analyses	82	2	3	9	7
SiO_2	27.38 (1.17)	29.92 (.26)	30.23 (.21)	27.60 (.55)	26.90 (.24)
Y_2O_3	7.31 (3.73)	2.74 (.09)	19.51 (.43)	2.12 (.60)	2.44 (.73)
La_2O_3	5.72 (1.78)	5.35 (.11)	2.63 (.02)	13.29 (2.18)	1.91 (.32)
Ce_2O_3	17.73 (2.81)	18.29 (.27)	8.23 (.37)	27.04 (.74)	16.41 (1.38)
Pr_2O_3	2.16 (.64)	2.55 (.34)	1.37 (.26)	2.27 (.40)	3.20 (.43)
Nd_2O_3	11.19 (2.58)	14.86 (.09)	6.32 (.13)	8.65 (1.00)	19.30 (.92)
Sm_2O_3	3.16 (1.08)	3.62 (.30)	1.70 (.18)	1.39 (.45)	6.36 (.41)
Gd_2O_3	2.40 (1.34)	3.65 (.52)	3.11 (.13)	0.75 (.31)	4.38 (.55)
Dy_2O_3	n.a.**	0.88 (.01)	2.81 (.56)	n.a.	n.a.
Er_2O_3	n.a.	-*	0.64 (.12)	n.a.	n.a.
Yb_2O_3	n.a.	-	0.61 (.28)	n.a.	n.a.
FeO	2.22 (1.33)	3.80 (.08)	3.69 (.13)	0.69 (.35)	-
CaO	3.39 (1.58)	4.22 (.01)	5.81 (.17)	2.82 (.29)	1.21 (1.3)
Na_2O	-	0.53 (.01)	-	-	-
F	-	-	-	-	0.22 (.15)
F–O corr.	-	-	-	-	–0.09
Total	82.66	90.41	86.66	86.62	82.24
Atoms based on Si = 6.00					
Si	6.00	6.00	6.00	6.00	6.00
Y	0.85	0.29	2.06	0.25	0.29
La	0.46	0.40	0.19	1.07	0.16
Ce	1.42	1.34	0.60	2.16	1.34
Pr	0.17	0.19	0.10	0.18	0.26
Nd	0.88	1.07	0.45	0.67	1.55
Sm	0.24	0.25	0.12	0.10	0.50
Gd	0.17	0.24	0.20	0.05	0.32
Dy		0.04	0.18		
Er		-	0.04		
Yb		-	0.04		
∑REE	4.19	3.82	3.98	4.48	4.42
Fe	0.41	0.43	0.61	0.12	-
Ca	0.80	0.61	1.23	0.66	0.29
Na	-	0.21	-	-	-
F	-	-	-	-	0.29

* - = below detection limit ** n.a. = not analysed Numbers in parentheses are 1σ

1: Average of mineral A2 grains in eudialyte decomposition aggregates. 2 and 3: zones in primary A2 grain in sample 230301 (Fig. 19) from aegirine pegmatite. 4: Phase resembling A2 in sample 151460 (Fig. 20) from aegirine pegmatite. 5: mineral A2 in decomposed eudialyte in sample 104361 from the marginal pegmatite.

Table 7 Correlation matrix for elements in mineral A2

	Ca	Fe	Y	La	Ce	Pr	Nd	Sm	Gd
Ca	1.00								
Fe	0.73	1.00							
Y	–0.05	0.21	1.00						
La	0.24	0.29	–0.51	1.00					
Ce	–0.40	–0.54	–0.82	–0.51	1.00				
Pr	–0.59	–0.58	–0.42	–0.06	0.56	1.00			
Nd	–0.81	–0.85	–0.37	–0.30	0.59	0.69	1.00		
Sm	–0.78	–0.87	–0.17	–0.48	–0.40	0.58	0.92	1.00	
Gd	–0.63	–0.82	–0.13	–0.48	–0.28	0.46	0.75	0.81	1.00

Mineral A2 in sample 104361, from the marginal pegmatite, has a Si:REE ratio of 6:4.42 (Table 6 no. 5) which is similar to that of A2 from the kakortokites. The proportions between the REE in A2 from the two areas are also comparable.

Monazite

Monazite occurs in decomposed eudialyte as isolated apparently primary grains in silicate minerals and as a decomposition mineral after an unknown mineral. The average chemical composition of the mineral, excluding analyses from samples 23-2 and 199195, is listed in Table 8 no. 1 and results in the formula: $(Ce_{0.48}La_{0.30}Pr_{0.04}Nd_{0.12}Sm_{0.01}Ca_{0.01})_{\Sigma 0.96}(P_{0.97}Si_{0.03})_{\Sigma 1.00}F_{0.03}O_{3.90}$. From the correlation coefficients for monazite (Table 9), it is seen that Ce is negatively correlated with La and Y and positively correlated with Nd, Pr and Sm. La is negatively correlated with Nd, Pr, Sm and Gd. This is also seen from the Ce-La-(Pr+Nd+Sm+Gd) plot in Fig. 22, which displays the same general trend as that recorded for both Ca-rich and Ca-poor A1.

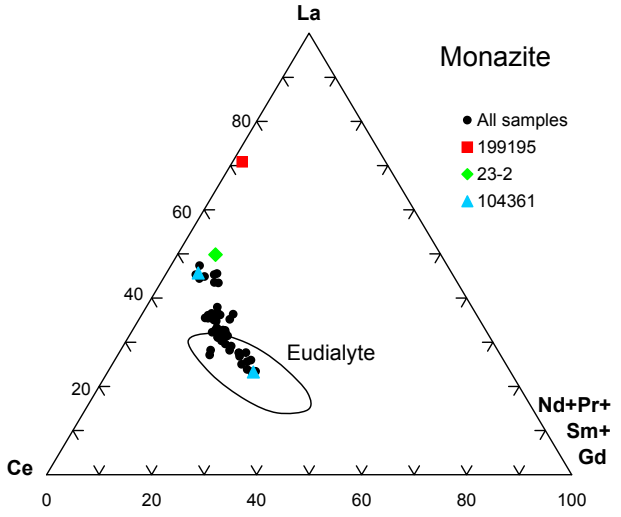

Fig. 22. Molar plot of REE in monazite. "All samples" exclude the two samples 199195 and 23-2 plotted separately. The two analyses from 104361 plotted separately are the extremes given in Table 8. Analyses of unaltered eudialyte plot within the encircled area. See text for discussion.

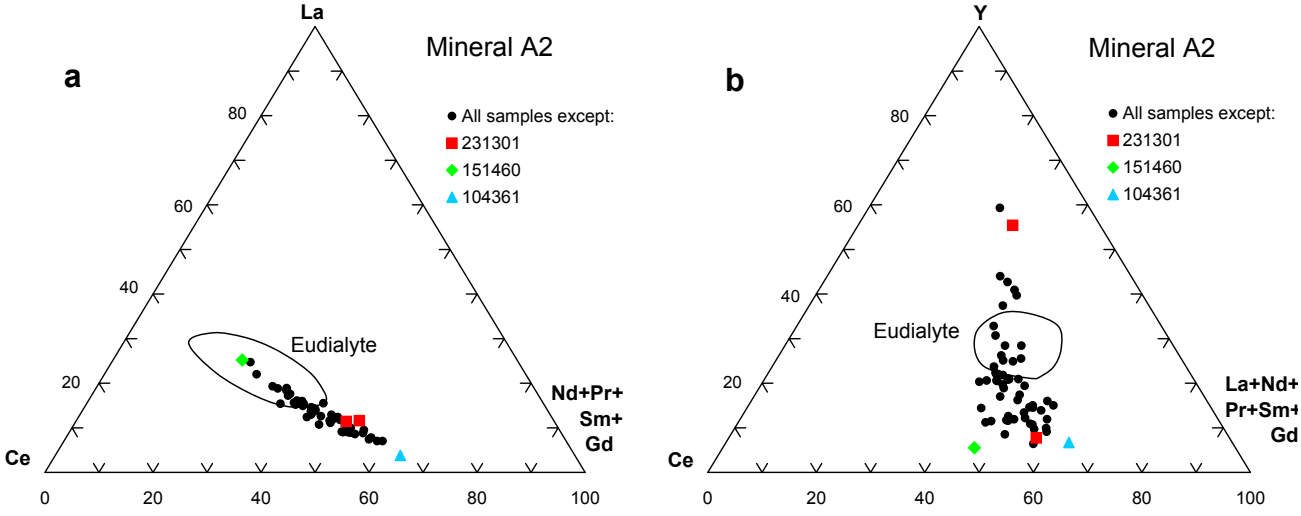

Fig. 21. Molar plots of REE in mineral A2. Analyses of unaltered eudialyte plot within the encircled areas. See text for discussion.

Table 8. Microprobe analyses of monazite

	1	2	3	4	5
Sample no.	All analyses*	104361 lightest	104361 darkest	23-2	199195
No. of analyses	134	3	3	13	4
SiO_2	0.84 (.84)	0.67 (.02)	0.08 (.03)	0.29 (.25)	0.44 (.41)
TiO_2	0.02 (.03)	-	-	0.03 (.03)	-
ZrO_2	0.09 (.18)	0.05 (.04)	-	0.04 (.05)	-
ThO_2	0.38 (.53)	0.48 (.05)	-	0.22 (.20)	0.43 (.42)
UO_2	0.02 (.01)	n.a.**	n.a.	0.02 (.01)	0.06 (.07)
P_2O_5	30.86 (1.20)	31.53 (.26)	31.88 (.63)	31.75 (.69)	31.44 (.96)
Al_2O_3	0.03 (.07)	-	-	0.02 (.02)	-
Nb_2O_3	0.03 (.03)	-	-	0.04 (.08)	-
Y_2O_3	0.04 (.05)	0.06 (.05)	-	0.05 (.06)	0.04 (.04)
La_2O_3	21.95 (3.90)	16.04 (.23)	32.28 (1.07)	35.59 (3.25)	49.43 (1.56)
Ce_2O_3	35.09 (1.56)	34.01 (.26)	34.36 (.64)	30.88 (1.89)	19.19 (.90)
Pr_2O_3	2.62 (.58)	3.33 (.25)	1.30 (.15)	1.35 (.34)	0.44 (.16)
Nd_2O_3	8.80 (2.59)	13.59 (.41)	2.65 (.25)	3.74 (1.16)	0.73 (.10)
Sm_2O_3	0.89 (.53)	2.02 (.14)	0.39 (.13)	0.17 (.20)	-
Gd_2O_3	0.20 (.23)	0.87 (.29)	0.05 (.09)	0.07 (.06)	0.14 (.17)
FeO	0.02 (.02)	-	-	-	0.05 (.06)
MnO	0.02 (.03)	-	-	-	0.05 (.07)
CaO	0.17 (.28)	0.04 (.01)	0.02 (.02)	0.03 (.02)	0.03 (.03)
K_2O	0.02 (.03)	-	-	-	0.04 (.04)
Na_2O	0.02 (.06)	-	-	-	-
F	0.22 (.26)	0.05 (.02)	0.04 (.03)	0.37 (.23)	0.42 (.17)
F–O corr.	–0.09	–0.02	–0.02	–0.16	–0.18
Total	102.24	102.72	103.03	104.50	102.75
Atoms based on P+Si = 10.00					
Si	0.31	0.24	0.03	0.11	0.16
Ti	-	-	-	-	-
Zr	0.02	0.02	-	-	-
Th	0.03	-	-	0.02	0.04
U	-	-	-	-	-
P	9.69	9.76	9.97	9.89	9.84
Al	0.01	-	-	-	-
Nb	-	-	-	-	-
Y	-	0.01	-	0.01	-
La	3.00	2.16	4.40	4.83	6.79
Ce	4.76	4.55	4.65	4.16	2.60
Pr	0.35	0.44	0.18	0.18	0.06
Nd	1.16	1.78	0.35	0.49	0.10
Sm	0.11	0.26	0.05	0.02	-
Gd	0.02	0.11	-	-	0.02
∑REE	9.40	9.31	9.63	9.69	9.57
Fe	-	-	-	-	0.01
Mn	-	-	-	-	0.01
Ca	0.07	0.01	-	0.01	0.01
K	0.02	-	-	-	0.02
Na	0.02	-	-	-	-
F	0.27	0.06	0.05	0.43	0.48

* except analyses from samples 23-2 and 199195

Numbers in parentheses are 1σ

** n.a. = not analysed

Table 9. Correlation matrix for REE in monazite

	Y	La	Ce	Pr	Nd	Sm	Gd
Y	1.00						
La	–0.02	1.00					
Ce	–0.18	–0.71	1.00				
Pr	–0.01	–0.82	0.57	1.00			
Nd	0.10	–0.89	0.50	0.82	1.00		
Sm	0.23	–0.60	0.23	0.44	0.69	1.00	
Gd	0.02	–0.29	–0.03	0.25	0.37	0.38	1.00

Monazite in sample 104361 from the marginal pegmatite was described in Karup-Møller *et al.* (2010), appearing as a patchy aggregate of crystals isolated in silicate minerals. Analyses of the lightest and darkest areas (Table 8 nos 2 and 3) of this aggregate gave the compositions (a): $(Ce_{0.46}La_{0.22}Pr_{0.04}Nd_{0.18}Sm_{0.03}Cd_{0.01})_{\sum 0.93}(P_{0.98}Si_{0.02})_{\sum 1.00}F_{0.01}O_{3.88}$ and (b): $(Ce_{0.47}La_{0.44}Pr_{0.02}Nd_{0.04}Sm_{0.01})_{\sum 0.98}P_{1.00}F_{0.01}O_{3.97}$ respectively. In Fig. 22, these compositions lie at the ends of the elongated monazite compositional range.

Monazite in sample 23-2 (circular pegmatite) and 199195 (marginal pegmatite) (Table 8 nos 4 and 5) have higher contents of La and correspondingly lower contents of Ce (Fig. 22). Monazite in sample 199195 represents the La-richest mineral recorded by us. It has the composition $(Ce_{0.26}La_{0.68}Pr_{0.01}Nd_{0.01})_{\sum 0.96}(P_{0.98}Si_{0.02})_{\sum 1.00}F_{0.05}O_{3.90}$.

Mineral A3 and associated minerals Uk2 and Uk3

Decomposition of the marginal area of a relatively large eudialyte crystal in sample 151428 has resulted in the formation of catapleiite as host for monazite and two previously undescribed minerals, A3 and Uk3. Two aggregates of A3 are present; one of these is shown in Fig. 23. The average chemical composition of 13 microprobe analyses of both aggregates is listed in Table 10 no. 1. A3 also occurs intergrown with Uk3 forming the aggregate shown in Fig. 24. The compositions of the two phases in this aggregate are listed in Table 10 nos 2 and 4.

In the analyses in Table 10 nos 1 and 2 the molar proportions for A3 are based on Si (+Ti) = 6.00. The average Si:REE is 6:2.78, i.e. close to 2:1, and quite different from that of A1 (1:1) and A2 (3:2). The oxide total is close to 80 wt%. A3 (like A2) is thus an OH/H_2O mineral with only small contents of F (A2 has no F). The following simplified formula for A3 is suggested: $Na_{0.2}Ca_{0.6}Mn_{0.5}Fe_{0.2}Al_{0.5}REE_{2.8}Si_{6.0}F_{0.5}O_{18-y}(OH)_{2y} \cdot nH_2O$.

The simplified formula for Uk3 is $CaCe_2(La,Pr,Nd,Sm,Gd)_2F_{0.2}O_{7-y}(OH)_{2y} \cdot nH_2O$. A phase with a similar composition has been identified in sample Gr2. Close to the decomposed eudialyte material in sample 151428, mineral Uk2 occurs as fracture fillings in fresh eudialyte (Fig. 25, Table 10 no. 3). It has a chemical composition $REE_{2.00}F_{1.50}O_{2.25-y}(OH)_{2y} \cdot nH_2O$, with Ce:(La+Pr+Nd+Sm+Gd)=1:1. It is almost identical with mineral Uk2 described by Karup-Møller *et al.* (2010). A phase with a similar composition has also

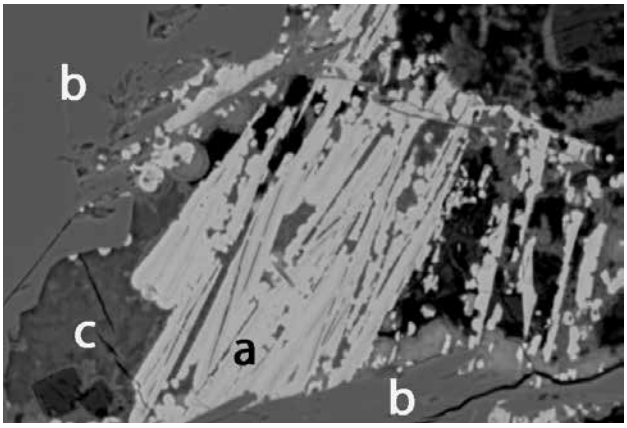

Fig. 23. Slightly radiating aggregate of mineral A3 crystals (a) in a matrix presumably of analcime (c) enclosed in catapleiite (b). Note the colloform texture of both analcime and A3 at upper left in the image. Sample 151428, circular pegmatite. Width of image 0.12 mm.

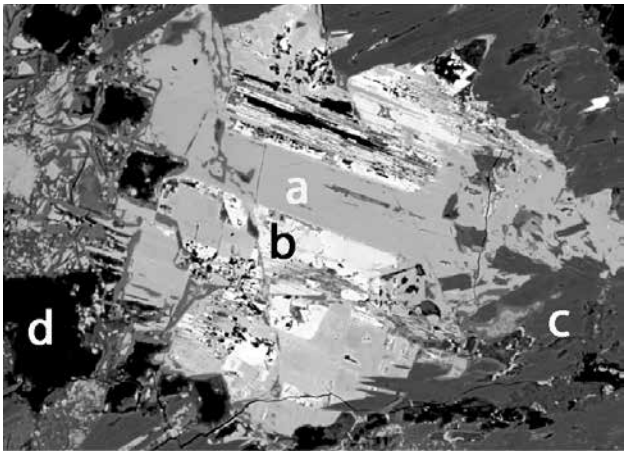

Fig. 24. Aggregate of mineral A3 (a) intergrown with mineral Uk3 (b) enclosed in catapleiite (c). Epoxy filled cavity at d. Sample 151428, circular pegmatite. Width of image 0.24 mm.

Table 10. Microprobe analyses of unidentified phases in sample 151428 (circular pegmatite)

	1	2	3	4
Mineral	A3	A3	Uk2	Uk3
No. of analyses	13	5	6	7
SiO_2	30.85 (1.43)	30.00 (.61)	-	0.20 (.06)
TiO_2	0.10 (.07)	0.11 (.03)	-	-
ZrO_2	- *	-	-	-
ThO_2	-	-	-	-
UO_2	-	-	-	-
P_2O_5	0.02 (.01)	0.02 (.01)	0.04 (.02)	0.03 (.03)
Al_2O_3	2.04 (.27)	2.14 (.14)	-	0.12 (.09)
Nb_2O_3	1.60 (.56)	1.62 (.09)	-	-
Y_2O_3	0.24 (.14)	0.42 (.20)	0.13 (.05)	0.06 (.05)
La_2O_3	10.08 (.70)	10.52 (.43)	21.57 (3.23)	17.78 (1.09)
Ce_2O_3	19.91 (.86)	17.93 (.38)	35.24 (1.13)	34.14 (1.35)
Pr_2O_3	1.90 (.22)	1.49 (.12)	2.94 (.26)	3.18 (.20)
Nd_2O_3	7.56 (.73)	5.90 (.40)	12.89 (1.83)	13.71 (.89)
Sm_2O_3	0.57 (.13)	0.51 (.09)	0.98 (.15)	1.32 (.24)
Gd_2O_3	0.12 (.14)	0.05 (.08)	0.40 (.20)	0.38 (.18)
Dy_2O_3	0.03 (.04)	0.12 (.14)	-	0.04 (.04)
Er_2O_3	-	-	0.10 (.10)	-
Yb_2O_3	0.04 (.06)	0.07 (.08)	0.14 (.15)	0.05 (.05)
FeO	1.17 (.26)	0.74 (.05)	-	-
MnO	2.61 (.65)	3.18 (.50)	-	-
CaO	3.00 (.26)	2.78 (.32)	0.45 (.08)	5.86 (.038)
K_2O	0.02 (.02)	0.02 (.01)	-	-
Na_2O	0.49 (.15)	0.49 (.02)	-	-
F	0.61 (.14)	0.79 (.06)	6.66 (.39)	0.45 (.14)
F–O corr.	–0.26	–0.33	–2.80	–0.19
Total	82.70	78.57	78.71	77.13
Atoms to	Si+Ti = 6.00	Si+Ti = 6.00	∑REE = 2.00	∑REE = 4.00
Si	5.98	5.98		0.04
Ti	0.02	0.02		
Al	0.47	0.51		0.02
Nb	0.14	0.15		
Y	0.02	0.05	0.01	0.01
La	0.73	0.77	0.59	1.02
Ce	1.42	1.31	0.95	1.94
Pr	0.13	0.11	0.08	0.18
Nd	0.52	0.42	0.34	0.76
Sm	0.04	0.04	0.02	0.07
Gd	0.01		0.01	0.02
∑REE	2.87	2.70	2.00	4.00
Fe	0.19	0.12		
Mn	0.43	0.53		
Ca	0.62	0.59	0.04	0.98
K				
Na	0.18	0.19		
F	0.38	0.50	1.54	0.22

* - = below detection limit Numbers in parentheses are 1σ

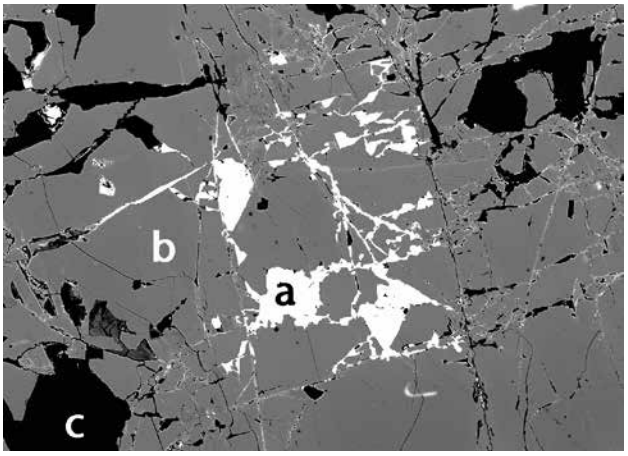

Fig. 25. Fractures in fresh eudialyte (b) filled with mineral Uk2 (a). Black areas (c) are either a silicate mineral (K-feldspar or analcime) or epoxy-filled cavities. Sample 151428, circular pegmatite. Width of image 0.61 mm.

been identified in samples from kakortokite layer –11 (Table 11 no. 5), 109304 and 230790.

Kainosite-(Y) and unknown Y-rich mineral Y1

In decomposed eudialyte in sample 151564 and kakortokite layer –11 we have identified two Y-rich minerals. One of these is assumed to be kainosite-(Y), while the other is assumed to be a new mineral species which has been termed Y1.

In Fig. 26 kainosite-(Y) is intergrown with catapleiite, and both minerals enclose Ca-poor A1 crystals. In addition aegirine and patches of K-feldspar are present. In other aggregates kainosite-(Y) (Table 11 no. 1) occurs intergrown with A1 and an unidentified Nb mineral (Karup-Møller & Rose-Hansen, unpublished data). The element oxide total recorded for kainosite-(Y) is close to 90 wt%. Assuming that the mineral is kainosite-(Y), i.e. a carbonate, then on the basis of the analysis in Table 11 no. 1 the following formula has been calculated: $(Ca,Fe,Na)_{1.99}(Y_{1.45}REE_{0.53})(SiO_3)_4CO_3{\cdot}H_2O$, or simplified $Ca_2Y_{1.5}REE_{0.5}(SiO_3)_4CO_3{\cdot}H_2O$.

Ca-poor A1 (Table 11 no. 2) often encrusts a phase which appears dark grey to nearly black in the microprobe images (Figs 27, 28). Microprobe analysis of this phase (Table 11 no. 3) yielded compositions close to that of the A1 host. The textural relations suggest that, as A1 crystallized, it enclosed material which subsequently crystallized as a distinct phase with a composition close to the host but enriched in Nb and Th. This phase presumably also contains OH/H_2O because the wt% oxide sum is slightly lower than that of the host.

Mineral Y1 was found in decomposed eudialyte in the sample from kakortokite layer –11. It forms a small aggregate enclosed in catapleiite. In the same catapleiite matrix we also found an aggregate of monazite (Fig. 29). The microprobe analysis of Y1 in this aggregate (Table 11 no. 4) is reported in wt% element values because it is not an oxide phase. Assuming that the missing anions are OH^- groups, then, on the basis of the analysis in Table 11 no. 4, the following simplified formula for Y1 is proposed: $Na_2Ca_4Y_{2.7}REE_{1.3}F_{18}(OH)_4$.

Discussion

Ca-rich and Ca-poor mineral A1

The two mineral A1-varieties have compositions resembling those of britholite: $(REE,Ca)_{10}(SiO_4,PO_4)_6(OH,F)_2$, britholite-(Ce): $Ca_4Ce_6(SiO_4)_6(OH)_2$ (Oberti *et al*. 2001) and lessingite-(Ce): $Ca_4REE_6(SiO_4)_6(OH,F)_2$. An unnamed mineral with the composition $NaCa_{1.5}REE_7(Si,P)_6O_{24}OH \cdot nH_2O$ described by Kalsbeek *et al*. (1990) is also regarded as a P_2O_5-poor member of the britholite group of minerals by these authors.

Britholite was originally found in South Greenland (Winther 1899). Since then, britholite has been found in several alkaline intrusions throughout the world. The mineral generally forms as a result of hydrothermal alteration (Arden & Halden 1999), although at the type locality it occurs as primary crystals in a nepheline syenite pegmatite at Naujakasik (Bøggild 1933). Britholite-(Ce) forms a solid solution series with apatite by the substitution of REE and Si for P and Ca (Khudolozhkin *et al*. 1973). Fully substituted britholite should then have the ideal composition $Ca_4REE_6(SiO_4)_6(F,OH)_2$, which actually is the composition of the now discarded lessingite-(Ce) (Burke 2006). Lessingite-(Ce) from the type locality at Kyshtym in Russia was described by Zilbermintz (1929) and restudied by Kalsbeek *et al*. (1990) who concluded that britholite-(Ce), lessingite-(Ce) and their unnamed mineral have the same crystal structure.

Britholite and related minerals belong to the apatite group with the general formula $M_{10}(ZO_4)_6X_2$ (M = Ca, Zr, Pb, Na…., Z = P, As, Si, V, REE…, and X = F, OH, Cl…). These minerals are tolerant to structural distortion and chemical substitution and are therefore extremely diverse in composition (e.g. Kreidler & Hummel 1970; McConnell 1973; Roy *et al*.1978; Elliott 1994). An extensive list of apatite group minerals and synthetic compounds with apatite structure is given by Pan & Fleet (2002). The X anions in the c-axis channels of natural apatites are dominated by F^-, OH^- and Cl^-. Additional substitutions in the c-axis anion channels include other monovalent anions (e.g. Br^-, I^-, O_2^-, O_3^-, BO_2^-, NCO^-, NO_3^- and NO_2^-) and divalent anions

Table 11. Microprobe analyses of kainosite and associated minerals

	1	2	3	4	5
Sample	151564	151564	151564	Layer–11	Layer–11
Mineral	Kainosite-(Y)	A1 (Ca-poor)	Phase enclosed in A1	Y1***	Uk2
No. of analyses	6	2	2	5	5
SiO_2	35.49 (.56)	23.97 (.13)	22.44 (.61)	-	0.03 (.02)
TiO_2	-*	0.17 (.03)	0.22 (.05)	-	-
ZrO_2	-	-	0.34 (.01)	-	-
ThO_2	0.14 (.09)	0.12 (.05)	2.66 (.01)	-	-
UO_2	0.05 (.03)	-	n.a.	-	0.03 (.02)
P_2O_5	-	0.14 (.06)	0.38 (.09)	-	0.02 (.02)
Al_2O3	-	0.58 (.15)	1.44 (.07)	-	-
Nb_2O_3	0.06 (.04)	0.07 (.03)	2.43 (.12)	0.04	-
Y_2O_3	24.22 (.81)	2.65 (.29)	3.09 (.01)	24.53	0.07 (.04)
La_2O_3	0.04 (.04)	17.97 (.05)	9.07 (.34)	0.50	17.69 (.38)
Ce_2O_3	0.15 (.14)	29.06 (.27)	24.10 (.32)	1.95	35.26 (.17)
Pr_2O_3	0.04 (.04)	2.30 (.15)	2.60 (.06)	0.63	3.15 (.21)
Nd_2O_3	0.34 (.19)	8.62 (.11)	12.06 (.05)	4.60	12.71 (.17)
Sm_2O_3	0.18 (.12)	2.12 (.02)	4.03 (.13)	1.80	1.62 (.28)
Gd_2O_3	2.18 (.23)	2.01 (.21)	3.13 (.39)	4.82	0.20 (.06)
Dy_2O_3	4.23 (.52)	n.a.**	n.a.	3.26	n.a.
Er_2O_3	4.35 (.28)	n.a.	n.a.	1.29	n.a.
Yb_2O_3	3.02 (.44)	n.a.	n.a.	0.32	n.a.
FeO	0.02 (.02)	1.22 (.04)	1.00 (.06)	-	-
MnO	-	0.23 (.06)	0.52 (.24)	-	-
CaO	14.84 (.28)	3.92 (.10)	3.29 (.13)	16.25	-
K_2O	-	-	-	-	-
Na_2O	0.40 (.14)	-	-	4.55	-
F	-	1.20 (.16)	1.20 (.16)	33.84	6.82 (.37)
F–O corr.	-	–0.51	–0.51	-	–2.87
Total	89.75	95.84	93.49	98.38	74.73
Atoms to	Si = 4.00	Si+Ti = 6.0	Si+Ti+Zr = 6.0	Ca = 4.00	∑REE =2.00
Si	4.00	5.97	5.91		
Ti		0.03	0.04		
Zr			0.04		
Th			0.16		
U					
P		0.03	0.09		
Al		0.17	0.45		
Nb		0.01	0.29		
Y	1.45	0.35	0.43	2.72	
La		1.68	0.88	0.04	0.51
Ce	0.01	2.65	2.33	0.14	1.00
Pr		0.21	0.25	0.04	0.09
Nd	0.02	0.77	1.14	0.31	0.35
Sm	0.01	0.18	0.37	0.12	0.04
Gd	0.08	0.17	0.27	0.30	0.01
Dy	0.15			0.20	
Er	0.15			0.08	
Yb	0.11			0.02	
∑REE	1.98	6.01	5.67	3.97	2.00
Fe		0.25	0.22		
Mn		0.05	0.10		
Ca	1.79	1.05	0.93	4.00	
K					
Na	0.09			1.95	
F	-	0.78	1.01	17.56	1.67

* - = below detection limit ** n.a. = not analysed ***element values, not oxides

Numbers in parentheses are 1σ

(O^{2-}, CO_3^{2-}, O_2^{2-}, S^{2-}, HCN^{2-} and NO_2^{2-}), vacancy (□), and neutral and organic molecules (McConnel 1973; Trompe & Montel 1978; Elliott 1994). A large number of divalent, trivalent, tetravalent and hexavalent cations may substitute for Ca^{2+}. Ca-deficiency has been reported to occur in both natural and synthetic apatites. Assuming that Ca-rich A1 with 25 mol % Ca less than in ideal britholite has the apatite structure, the following substitution may have taken place: $Ca^{2+}+F^{-} = H^{+}+$ □ and the formula would then be: $HCa_3REE_6(SiO_4)_6(F□)$, with Si:REE = 1:1.

The Ca-poor A1 has a significantly lower Si:REE ratio than Ca-rich A1. It is not possible to demonstrate substitutional relationships involving anion vacancies and still maintain the apatite structural scheme for this mineral. We therefore conclude that Ca-poor A1 does not have the apatite structure. At present the following simplified empirical formula for the mineral is proposed: $(Fe,Mn,Ca)_{1.5}REE_6Si_6FO_{22}$ until the mineral is found with a sufficiently large crystal size to allow its structure to be determined.

It is evident from Fig. 11 that Ce remains almost independent of the substitutional relationships between the other REE, in particular La and Nd, in the crystal structure of both A1 varieties and to some extent also in monazite (Fig. 22). Furthermore Ce, in contrast to the other REE, may occur with both valences +3 and +4. Alteration of eudialyte may have taken place under

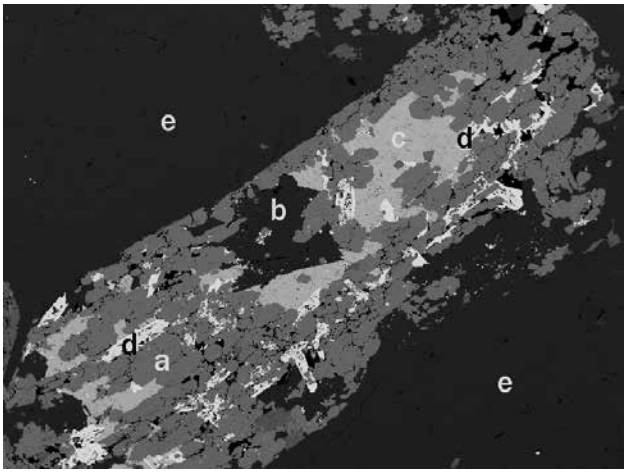

Fig. 26. Eudialyte decomposition aggregate composed of catapleiite (a), kainosite-(Y) (c), Ca-poor A1 (d) and K-feldspar and analcime (b) isolated in a fine-grained albite matrix (e). Note that aegirine is absent from the decomposition aggregate. Sample 151564, aegirine pegmatite sill. Width of image 1.47 mm.

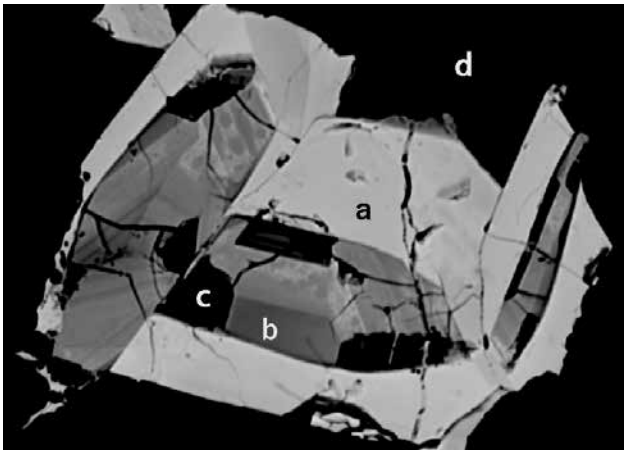

Fig. 27. Aggregate of Ca-poor A1 crystals (a) enclosing a phase with composition near A1 (b). The black areas (c) are either a silicate mineral (analcime or K-feldspar) or epoxy-filled cavities. The host (d) is catapleiite. Sample 151564, aegirine pegmatite sill. Width of image 0.13 mm.

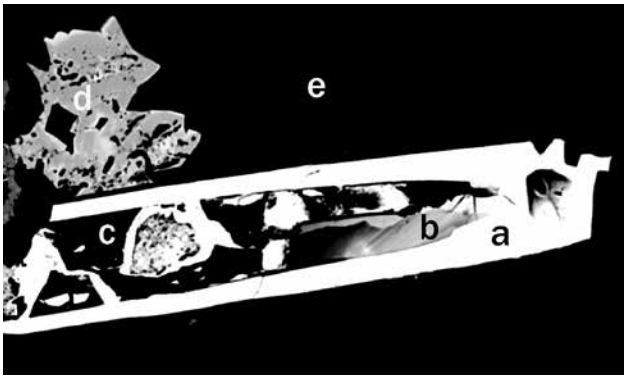

Fig. 28. Ca-poor A1 crystal (a) enclosing an A1-like phase (b) and epoxy-filled cavities or an unidentified silicate mineral (c) in contact with an unidentified REE-mineral (d), all enclosed in catapleiite (e). Similar A1 crystals are enclosed in the eudialyte decomposition aggregate shown in Fig. 26. Sample 151564, aegirine pegmatite sill. Width of image 0.25 mm.

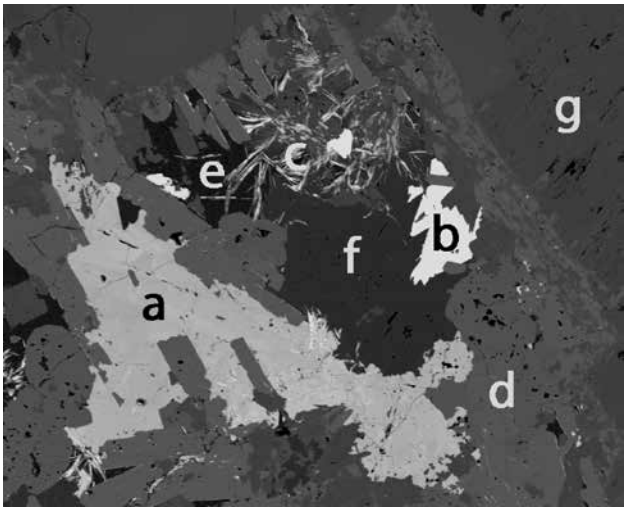

Fig. 29. Eudialyte decomposition aggregate composed of an aggregate of mineral Y1 crystals (a), an aggregate of monazite crystals (b), thin A1-crystals (c), catapleiite (d), K-feldspar (f) and analcime (e), enclosed in aegirine (g). Kakortokite layer –11. Width of image 0.90 mm.

oxygen fugacities sufficiently high to allow for the formation of Ce^{4+}. However it is not very likely that the Ce^{4+} ion, because of its small ionic radius (0.97 Å for Ce^{4+} versus 1.14 for Ce^{3+}, Shannon 1976), may exist in the apatite structure type although it is common in zircon (Thomas *et al*. 2003). The ionic radius of Zr^{4+} is 0.87 Å. However, assuming that one Ce atom per formula unit of Ca-rich A1 has a valence of +4, then this would require one empty cation position and one empty anion position per formula unit. With two Ce^{4+} cations per formula unit, one empty cation position is still required but no empty anion positions.

Assuming that Ca-poor A1 also has apatite structure, then 2.5 Me^{2+} per formula unit are 'missing'. However, there are only about 3 Ce atoms per formula unit. Assuming that all three Ce atoms have a valence of +4, then one Me^{2+} would still be missing. This could be resolved by having one half empty position plus two 'empty' Me^{2+} occupied by H^+, and fully occupied anion positions per formula unit. Under these assumptions the following two formulae for Ca-rich A1 and one for Ca-poor A1 can be proposed:

Ca-rich A1: $\square Ca_3Ce^{4+}REE_5(SiO_4)_6(F\square)$

Ca-rich A1: $\square Ca_3Ce_2^{4+}REE_4(SiO_4)_6(F,OH)_2$

Ca-poor A1: $\square_{0.5}H_2(Fe,Mn,Ca)_{1.5}Ce_3^{4+}REE_3(SiO_4)_6(F,OH)_2$

Ca-poor A1 enriched in Nb, Th, Ti and Al

All mineral A1 studied, except for in sample 23-2, are formed from the decomposition of eudialyte. Eudialyte has no detectable amounts of P, and this may explain why mineral A1 contains very little of this element, although monazite is an accessory mineral in some aggregates. However, in sample 23-2 Ca-poor A1 in association with catapleiite and an unidentified Nb-mineral was precipitated in cavities after an unknown mineral, presumably the water-soluble mineral villiaumite (NaF). Early precipitated mineral A1 contains considerable amounts of P and Na but only small amounts of Ca, Nb and Th and almost no aluminium. As the precipitation of minerals continued, late solutions may have reacted with early precipitated mineral A1 in these cavities resulting in the formation of hydrated mineral A1 varieties with up to 8.23 wt% ThO_2, 6.61 wt% Nb_2O_5, 1.77 w.% Al_2O_3, 1.61 wt% CaO and 0.98 wt% TiO_2. At the same time the contents of P and Na were strongly reduced. However, in all phases the Si+P to REE molar ratio remained virtually unchanged, close to 1:1. This suggests that the Ca-poor A1 structure type allows substantial substitutions as is the case for the apatite structure type.

Distribution of REE

During decomposition the majority of REE in the original eudialyte were concentrated mainly in mineral A1 and to some extent also in mineral A2. The other unidentified REE minerals play a subordinate role in this respect as they are present in insignificant amounts. Yttrium, however, plays a major role in the formation of the secondary minerals where Y is mainly concentrated in fergusonite-(Y), mineral A2, kainosite-(Y) and mineral Y1. Relatively little Y is present in mineral A1 compared to the amount contained in the original eudialyte (Fig. 11b, d).

Eudialyte contains practically no P; nevertheless in some decomposition aggregates both monazite and apatite have been identified. P must therefore have been introduced during the decomposition process from an external source.

A characteristic feature of nearly all the secondary minerals (except for kainosite-(Y) and mineral Y1) is that Ce constitutes nearly half the amount of REE present. This is also valid for the original eudialyte. For mineral A1, most of the analyzed monazite grains, and to some extent mineral A2, extensive exchange can take place between La on one hand and Pr, Nd, Sm and Gd on the other (Figs 11, 21, 22). In mineral A1 and some monazite grains, increasing content of La is accompanied by a slight increase in the content of Ce. In mineral A2 there is a more pronounced increase in the content of Ce with increasing content of La and decreasing contents of the other REE. A similar element relationship is only vaguely seen in the original eudialyte. Here increasing content of La is accompanied by increasing content of Nd and decreasing amounts of Pr, Sm and Gd. At the same time increasing contents of La and Nd are accompanied by a significantly stronger increase in the content of Ce compared to mineral A1. This is also indicated by the shape of the eudialyte compositional field in Fig. 11a.

Conclusions

The major alteration mineral of eudialyte from the kakortokite part of the Ilímaussaq complex is catapleiite. Generally the shapes of the original eudialyte crystals are perfectly preserved (e.g. the eudialyte pseudomorph in Fig. 26). It appears that the original element content in the eudialyte is preserved within the eudialyte pseudomorphs. Zirconium is contained in catapleiite. The major part of the REE are concentrated in mineral A1, locally also in fergusonite-(Ce), fergusonite-(Y), monazite, and minerals A2, A3, Uk2 and Uk3. Detailed analyses of mineral A1, originally described by Karup-Møller *et al*. (2010), have proved

the existence of two varieties: Ca-rich and Ca-poor A1. The Ca-rich variety, close in composition to 'lessingite' but with pronounced cation deficiency, has the ideal formula $HCa_3REE_6(SiO_4)_6(F\square)$ and may possess apatite structure; hence it may be a member of the britholite group. The chemically related Ca-poor A1 variety appears not to be a member of the same group. Mineral Uk2, originally described by Karup-Møller *et al*. (2010) and found only in one sample (locality C, Fig. 1) has been found during the present investigation at three additional localities.

The proportion between Ce and the other REE is close to 1:1 both in the original eudialyte and in the secondary minerals. Characteristic for all secondary minerals is a significant substitutional relationship between La on one hand and Nd, Pr, Sm, Gd (and presumably also the minor amounts of HREE) on the other. For mineral A1 (both varieties, but in particular for Ca-rich A1), there is a slight increase in the content of Ce with increasing content of La and decreasing content of Nd, Pr, Sm and Gd. This is substantial for mineral A2. For monazite the Ce content remains constant. A similar well-defined relationship for the REE in eudialyte cannot be recognized. Here the substitutional relationships between these elements are much less pronounced and they also show different trends (Fig. 11a).

Chlorine in the secondary minerals is below the detection limit, and this element must have been removed during the decomposition of eudialyte. In contrast, P which is absent in eudialyte must have been added to those decomposition aggregates which contain monazite and apatite.

The proportion between Y and the other REE is significantly higher in eudialyte than in mineral A1 (Fig.11b). This may explain the formation of fergusonite-(Y), mineral A2 and locally the two Y minerals kainosite-(Y) and Y1. Kainosite constitutes a significant proportion of the decomposition aggregate shown in Fig. 26. The original eudialyte in this sample may therefore have had an Y content above the average for this mineral.

Acknowledgements

We are grateful for the technical assistance of A. Berger, M.K. Sørensen and H. Diaz. E. Makovicky, J.C. Bailey, T. Balic-Zunic and H. Friis read the manuscript and made valuable comments on its contents. The English was checked by J.C. Bailey. Collaboration with H. Bohse in the field is greatly appreciated. The Danish Natural Science Research Council provided the microprobe facilities.

References

Andersen, S., Bailey, J.C. & Bohse, H. 1981: Zr-Y-U stratigraphy of the kakortokite-lujavrite-sequence, southern Ilímaussaq intrusion. Rapport Grønlands Geologiske Undersøgelse 103, 69–76.

Andersen, S., Bohse, H. & Steenfelt, A. 1988: The southern part of the Ilímaussaq complex, South Greenland, 1:20.000 geological map. Copenhagen: Geological Survey of Greenland.

Arden, K.M. & Halden, N.M. 1999: Crystallization and alteration history of britholite in rare-earth-element-enriched pegmatitic segregations associated with the Eden Lake Complex, Manitoba, Canada. Canadian Mineralogist 37, 1239–1253.

Bailey, J.C. 1995: Cryptorhytmic and macrorhytmic layering in aegirine lujavrite, Ilímaussaq alkaline intrusion, South Greenland. Bulletin of the Geological Society of Denmark 42, 1–16.

Bøggild, O.B. 1933: Igalikite and naujakasite, two new minerals from South Greenland. Meddelelser om Grønland 92(9), 12 pp.

Bohse, H. & Andersen, S. 1981: Review of the stratigraphic divisions of the kakortokite and lujavrite in southern Ilímaussaq. Rapport Grønlands Geologiske Undersøgelse 103, 53–61.

Bohse, H., Brooks, C.K. & Kunzendorf, H. 1971: Field observations on the kakortokites of the Ilímaussaq intrusion, South Greenland, including mapping and analyses by portable X-ray fluorescence equipment for zirconium and niobium. Rapport Grønlands Geologiske Undersøgelse 38, 43 pp.

Bohse, H., Rose-Hansen J., Sørensen, H., Steenfelt, A., Løvborg, L. & Kunzendorf, H. 1974: On the behavior of uranium during crystallization of magma – with special emphasis on alkaline magmas. In: Formation of Uranium Ore Deposits, 49–60.Vienna: International Atomic Energy Agency.

Burke, E.A.J. 2006: A mass discreditation of GQN minerals. Canadian Mineralogist 44, 1557–1560.

Elliott, J.C. 1994: Structure and chemistry of the apatites and other calcium orthophosphates, 387 pp. Amsterdam: Elsevier.

Ferguson, J. 1964: Geology of the Ilímaussaq alkaline intrusion, South Greenland. Description of map and structure. Bulletin Grønlands Geologiske Undersøgelse 39, 82 pp.

Gerasimovsky, V.I. 1969: Geochemistry of the Ilímaussaq alkaline massif (South-west Greenland). (Geochimija Ilimmassakskogo stselotsnogo massiva (Jugo-sapadnaja-Greenlandija), 174 pp. Moscow: Nauka. (in Russian).

Graser, G. & Markl, G. 2008: Ca-rich ilvaite-epidote-hydrogarnet endoskarns: a record of late-magmatic fluid influx in the persodic Ilímaussaq complex, South Greenland. Journal of Petrology 49, 239–265.

Henriksen, J.H.H. 1993: Geochemical trends through part of the upper transitional kakortokites and aegirine lujavrite I, Ilímaussaq intrusion, South Greenland. Unpublished M.Sc. thesis, University of Copenhagen, 185 pp.

Johnsen, O. & Bohse, H. 1981: Helvine from the Ilímaussaq intrusion. In: Bailey, J.C., Larsen, L.M. & Sørensen, H. (eds): The

Ilímaussaq intrusion, South Greenland. A progress report on geology, mineralogy, geochemistry and economic geology. Rapport Grønlands Geologiske Undersøgelse 103, 25–29.

Johnsen, O. & Grice, J.D. 1999: The crystal chemistry of the eudialyte group. Canadian Mineralogist 37, 865–891.

Kalsbeek, N., Larsen, S. & Rønsbo, J.G. 1990: Crystal structures of rare earth elements rich apatite analogues. Zeitschrift für Kristallographie 191, 249–263.

Karup-Møller, S. 1975: On the occurrence of the native lead, litharge, hydrocerussite and plattnerite from the Ilímaussaq alkaline intrusion in South Greenland. Neues Jahrbuch für Mineralogie, Monatshefte 5, 229–241.

Karup-Møller, S. 1982: Tundrite from the Ilímaussaq alkaline intrusion, South Greenland. Neues Jahrbuch für Mineralogie, Monatshefte 481–494.

Karup-Møller, S., Rose-Hansen, J. & Sørensen, H. 2010: Eudialyte decomposition minerals with hitherto undescribed phases from the Ilímaussaq complex, South Greenland. Bulletin of the Geological Society of Denmark 58, 75–88.

Khudolozhkin, O., Urusov, V.S. & Tobelko, K.I. 1973: Dependence of structural ordering of rare earth atoms in the isomorphous series apatite-britholite (abukumalite) on composition and temperature. Geochemistry International 10, 1171–1177.

Kreidler, E.R. & Hummel, F.A. 1970: The crystal chemistry of apatite: structure fields of fluor- and chlorapatite. American Mineralogist 55, 170–184.

Macdonald, R., Karup-Møller, S. & Rose-Hansen, J. 2007: Astrophyllite-group minerals from the Ilímaussaq complex, South Greenland. Mineralogical Magazine 71, 1–16.

McConnel, D. 1973: Apatite, its crystal chemistry, mineralogy, utilization, and geologic and biologic occurrences, 111pp. New York: Springer.

Oberti, R., Ottolini, L., Della Ventura, G. & Pardon, G.C. 2001: On the symmetry and crystal chemistry of britholite. New structural and microanalytical data. American Mineralogist 86, 1066–1075.

Pan, Y. & Fleet, M.E. 2002: Compositions of the apatite-group minerals: substitution mechanisms and controlling factors. Reviews in Mineralogy and Geochemistry 48, 13–49.

Pfaff, K., Krumrei, T.H. Marks, M., Wenzel, T.R. & Markl, G. 2008: Chemical and physical evolution of the "lower layered sequence" from the nepheline syenitic Ilímaussaq intrusion, South Greenland: Implications for the origin of magmatic layering in peralkaline felsic liquids. Lithos 106, 280–296.

Rose-Hansen, J. & Sørensen, H. 2002: Geology of the lujavrites from the Ilímaussaq alkaline complex, South Greenland, with information from seven bore holes. Meddelelser om Grønland, Geoscience 40, 58 pp.

Roy, D.M., Drafall, L.E. & Roy, R. 1978: Crystal chemistry, crystal growth, and phase equilibria of apatites. In: Alper, A.M. (ed.), Phase Diagrams, Material Sciences and Technology 6-V, 186–239. New York: Academic Press.

Shannon, R.D. 1976: Revised effective ionic radii and systematic studies of interatomic distances in halides and chalcogenides. Acta Crystallographica A 32, 751–767.

Sørensen, H. 1960: On the agpaitic rocks. Report 21st International Geological Congress Norden 1960 vol. 13, 319–327.

Sørensen, H. 1962: On the occurrence of steenstrupine in the Ilímaussaq massif, Southwest Greenland. Meddelelser om Grønland 167(1), 251 pp.

Sørensen, H. 1992: Agpaitic nepheline syenites: a potential source of rare elements. Applied Geochemistry 7, 417–427.

Sørensen, H. 2006: The Ilímaussaq alkaline complex, South Greenland. An overview of 200 years of research and an outlook. Meddelelser om Grønland, Geoscience 45, 1–70.

Sørensen, H., Rose-Hansen, J., Nielsen, B.L., Løvborg, L., Sørensen, E. & Lundgaard, T. 1974: The uranium deposit at Kvanefjeld, the Ilímaussaq intrusion, South Greenland. Geology, reserves and beneficiation. Rapport Grønlands Geologiske Undersøgelse 60, 54 pp.

Sørensen, H., Bohse, H. & Bailey, J.C. 2006: The origin and mode of emplacement of lujavrites in the Ilímaussaq alkaline complex, South Greenland. Lithos 91, 286–300.

Thomas, J.B., Bodnar, R.J., Shimizu, N. & Chesner, C.A. 2003: Melt inclusions in zircon. Reviews in Mineralogy and Geochemistry 53, 63–87.

Trompe J.C. & Montel, G. 1978: Some features in the incorporation of oxygen in different oxidation stages in the apatite lattice–II. On the synthesis and properties of calcium and strontium peroxiapatites. Journal of Inorganic Nuclear Chemistry 40, 23–26.

Ussing, N.V. 1898: Mineralogisk-petrografiske undersøgelser af grønlandske Nefelinsyenitter og beslægtede Bjergarter. Meddelelser om Grønland 14, 1–220.

Ussing, N.V. 1912: Geology of the country around Julianehaab, Greenland. Meddelelser om Grønland 38, 376 pp.

Westergaard, A.S. 1969: The border pegmatites of the Ilímaussaq intrusion. Rapport Grønlands Geologiske Undersøgelse 19, 39–40.

Winther, C. 1899: In: Bøggild, O.B. & Winther, C.: On some minerals from the nephelite-syenite at Julianehaab, Greenland (epistolite, britholite, schizolite and steenstrupine), collected by G. Flink. Meddelelser om Grønland 24, 181–213.

Zilbermintz, V.A. 1929: Sur le gisement de cérite, de bastnesite et d'un minéral nouveau la lessingite, dans le district Minier, Kychtym (Ural). Doklady Akademii. Nauk SSSR A3, 55–60.

Instructions to authors

The Bulletin publishes articles normally not exceeding 30 printed pages, notes not longer than 4 pages, and short contributions of maximum 1 printed page. Longer articles and monographs may be published at the discretion of the editors, but it is advisable to consult the chief editor before submitting long manuscripts. Short contributions may be comments on previously published articles, presentation of current scientific activities, short scientific notes, or book reviews.

Manuscripts with complete sets of illustrations, tables, captions, etc., should be submitted electronically to the chief editor (lml@geus.dk). The **main text** with references and figure captions should be either in Word or pdf format, **figures** should be in either pdf, jpeg, or tiff format, and **tables** should be in Word text format, i.e. written in lines with tab spacing between table columns. "Word tables" are discouraged because they are not re-formatted easily. Consult the editor before submitting other formats.

Manuscripts will be reviewed by two referees; suggestions of referees are welcome. The final decision on whether or not a manuscript will be accepted for publication rests with the chief editor, acting on the advice of the scientific editors. Articles will be published in the order in which they are accepted and produced for publication.

Manuscript

Language – Manuscripts should be in English. Authors who are not proficient in English should ask an English-speaking colleague for assistance before submission of the manuscript.

Title – Titles should be short and concise, with emphasis on words useful for indexing and information retrieval. An abbreviated title to be used as running head must also be submitted.

Abstract – An abstract in English must accompany all papers. It should be short (no longer than 250 words), factual, and stress new information and conclusions rather than describing the contents of the manuscript. Conclude the abstract with a list of key words.

Main text – Use 1.5 or double spacing throughout, and leave wide margins. Italics should be used only in generic and species names and in some Latin abbreviations (e.g. *c, et al., ibid., op. cit*).

Spelling – Geological units named after localities in Greenland, formal lithostratigraphical units and intrusions named after localities in Greenland remain unchanged even if the eponymous locality names have since been changed in accordance with modern Greenlandic orthography.

References to figures, tables and papers – References to figures and tables in the text should have the form: Fig. 1, Figs 1–3, Table 3 or as (Smith 1969, fig. 3) when the reference is to a figure in a cited paper.

References to papers are given in the form Smith (1969) or (Smith 1969). Combined citations by different authors are separated by a semicolon; two or more papers by same author(s) are separated by commas. Citations are mentioned chronologically and then alphabetically. Use 'et al.' for three or more authors, e.g. Smith et al. (1985).

Reference list

Use the following style:

Smith, A.A. 1989: Geology of the Bulbjerg Formation. Bulletin of the Geological Society of Denmark 38, 119–144. [Note that name of journal is given in full].

Smith, A.A., Jensen, B.B. & MacStuff, C.C. 1987: Sandstones of Denmark, 2nd edition, 533 pp. New York: Springer Verlag. [For more than 10 authors, use first author followed by *et al.*].

Smith, A.A., Jensen, B.B. & MacStuff, C.C. 1992: Characterization of Archean volcanic rocks. In: Hansen, D.D. *et al.* (eds): Geology of Greenland. Geological Survey of Denmark and Greenland Bulletin 40, 1397–1438. [More than three editors – therefore *et al.* form is used].

Sorting – Danish letters æ, ø and å (aa) are treated as ae, o and a (aa), respectively.

References are sorted by:

1: Alphabetically by the first author's surname
2: Papers by one author: two or more papers are arranged chronologically
3: Papers by two authors: alphabetically after second author's name. Two or more papers by the same two authors: chronologically.
4: Papers by three or more authors: chronologically. Papers from the same year are arranged alphabetically after second, third, etc.author's name.

Authors themselves are responsible for the accuracy and completeness of their references. If incorrect references are found, the manuscript will be returned to the author for complete rechecking. The reference list must include all, and only, the references cited in the paper (including figures, tables etc).

Illustrations

May be prepared in either black and white or colour. There is no colour charge. Horizontal illustrations are much to be preferred. Size of smallest letters in illustrations should not be less than 5.5 pt. Remember scale.

All figures (including photographs) should be submitted in electronic form ready for direct reproduction, i.e. having the dimensions of the final figure with a standard resolution of 300 dpi for photographs. Preferred formats are pdf, tiff and jpg.

Size – The width of figures must be 82 mm, 125 mm or 171 mm. Maximum height is 223 mm.

Captions – Captions to figures, tables and plates must be delivered on separate pages.

Supplementary data files

Supplementary files are accepted. Such files may provide e.g. analytical data tables, detailed data documentation, illustrations with special effects, or videos.

Proofs

Proofs – Authors receive page proofs of the article after technical set-up. The cost of any alterations against the final manuscript will be charged to the author.

Content, vol. 61

ISSN 1350-0150